Annual Report 2002

AG Magnetismus
Universität Kaiserslautern

Address: Prof. Dr. Burkard Hillebrands
Fachbereich Physik
Universität Kaiserslautern
Erwin-Schrödinger-Straße 56
67663 Kaiserslautern, Germany
Tel.: +49-(0)631-205-4228
Fax.:+49-(0)631-205-4095

Postal address: Postfach 3049
67653 Kaiserslautern, Germany

Internet: http://www.physik.uni-kl.de/hillebrands/
E-Mail: hilleb@physik.uni-kl.de

Our Group

From left to right:

Dr. Vladislav Demidov, Markus Weber, Andreas Beck, Dimitry Kholin, Christian Bayer, Dr. Mireia Blanco-Mantecón, Dr. Sergej Demokritov, Hans Nembach, Dr. Kurt Jung, Tim Mewes, Stefan Poppe, Bernd Pfaff, Heike Schuster, Dr. Jürgen Fassbender, Sybille Müller, Prof. Dr. Burkard Hillebrands, Dr. Marc Rickart

Contents

Chapter 1: Introduction

Dear colleagues and friends,

again we report on our research in the last 12 months, the period of November 2001 to October 2002.

Our key field is magnetization dynamics, and this field received a large boost in the last year. We investigated the eigenmode spectrum in inhomogeneously magnetized magnetic stripes and found several localized quantized modes near the edges of the stripes. A description of these modes in terms of spin waves in a potential well helped us to understand deeper the nature of these exciting new phenomena. Also new results were obtained in the field of nonlinear spin wave propagation: We demonstrated the formation of envelope solitons from parametrically amplified and from conjugated spin wave pulses and showed, that using phase control the non-adiabatic parametric amplification of spin wave packets can be reliably manipulated.

This work is paralleled by two important strategic developments. In Germany a new priority program ("Schwerpunktprogramm") entitled "Ultrafast magnetization processes" and funded by the Deutsche Forschungsgemeinschaft started operation in July, coordinated by Günter Reiss from Bielefeld and myself. Here 17 groups from all over Germany collaborate to achieve a basic understanding of the temporal evolution of fast magnetization processes in magnetically ordered films, multilayers and microstructured systems. A general aim is to understand the fundamental mechanisms needed for applications in ultrafast magneto-electronic devices. For more information see our web side at http://www.spindynamik.de. Second, within the European Community a Research Training Network on "Ultrafast Magnetization Processes in Advanced Devices" started operation in September, coordinated by the University of Kaiserslautern (see: http://www.ultraswitch.de). Seven universities and research laboratories and 3 industrial partners jointly address the field of ultrafast magnetization phenomena with large emphasis on the training of young researchers in this field.

Our other research activities were rather successful as well. In the field of exchange bias we showed that in the epitaxial system FeNi/FeMn an intervening Cu spacer layer generates oscillations of the exchange bias field as a function of its thickness. In a joint cooperation with the group of Jacques Ferré at the Université Paris Sud we were able to demonstrate, that the exchange bias field scales with the total magnetic moment at the ferromagnet-antiferromagnet interface, using magnetic second harmonic generation. We also found a new strategy to investigate the wide parameter space for remagntization processes in exchange bias systems spanned by the various anisotropy contributions. The understanding of interface anisotropies was advanced by realizing, that on periodically stepped Fe films on vicinal Au substrates the angular anisotropy in the height-height correlation function scales surprisingly well with the induced magnetic surface anisotropy.

The fields of elastic properties of films as well as of applications of hard coating materials to medical applications had also several highlights. We investigated the elastic properties of nanoporous low-dielectric-constant films by Brillouin light scattering and we improved the sputtering process for achieving dense carbon films deposited at room temperature for bio- and medical applications. Starting from the requirement for many biocompatible thin films to be either hydrophilic or hydrophobic we developed a variety of coatings with large variations in their surface potential. Beyond the biomedical applications these surfaces are also suitable to solve many adhesion related problems in other fields (eg. the extrusion of polymers).

Jürgen Fassbender successfully completed his habilitation, and he is now on the market for a professor position. Three members of our group received their Ph.D.: Radek Lopusnik, who then has started a post-doctoral stay in the group of Tom Silva at NIST, Boulder, Marc Rickart, who is now starting a post-doc position in the group of Paulo Freitas at INESC in Lisboa, and Thomas Wittkowski.

A particular pleasure was having Prof. J. Darrell Comins, University of the Witwatersrand, South Africa, with us. He spent his sabbatical in our group joining our activities on elastic properties of films, especially at high temperatures.

I myself enjoyed very much a sabbatical stay at the Université Paris Sud from October 2001 to February 2002, hosted by Jacques Ferré at the Laboratoire de Physique des Solides. The work with him and his group, as well as with Claude Chappert and his group at the Institut d'Électronique Fondamentale was very rewarding, and I would like to thank both very much for the hospitality and the good work.

Our work would not have been possible without valuable collaborations with people all over the world. They are too many to list them here all. In particular we would like to thank, in alphabetical order, Dima Berkow, Harry Bernas, Klaus Bewilogua, John Chapman, Claude Chappert, Darrell Comins, Hajo Elmers, Claude Fermon, Jacques Ferré, Colm Flannery, Loris Giovannini, Xin Jiang, Boris Kalinikos, Mikhail Kostylev, Natatia Kreines, Wolfram Maaß, Roland Mattheis, Alexandra Mougin, Fabrizio Nizzoli, Carl Patton, Günter Reiss, Frank Richter, John R. Sandercock, Gerd Schönhense, Andrei Slavin, Bob Stamps, Stefan Visnovsky and Manfred Weiler for their interactions with us and their strong input on our work. Collaborations within the Fachbereich Physik at the University of Kaiserslautern (Martin Aeschlimann, Hans Schmoranzer, Herbert Urbassek, Richard Wallenstein and Christiane Ziegler and their groups) and the Institut für Oberflächen- und Schichtanalytik have been very stimulating. I am especially grateful to Heinz Busch and Udo Grabowy and their start up company NTTF GmbH for the close contact after they left our institute and their participation in all biomedical projects. I am much obliged to Stefan Sattel and his team from the TZO GmbH for providing convenient general conditions for our work in Rheinbreitbach.

I would also like to thank all our sponsors, which are the Deutsche Forschungsgemeinschaft, the Bundesministerium für Bildung, Wissenschaft, Forschung und Technologie, the Humboldt Foundation, the Deutscher Akademischer Austauschdienst, the European Community, the European Science Foundation, INTAS, the State of Rheinland-Pfalz and the University of Kaiserslautern. My special thanks go to Andreas Beck, Tim Mewes, Sibylle Müller and Thomas Wittkowski for their help in preparing this report.

It is my special pleasure to greet all former group members. May this report help to stay in touch with each other.

If you are interested in our work I would be happy to hear from you. If you have any questions, comments, suggestions, or any kind of criticism, please contact us.

With all my best wishes for Christmas, and a Happy New Year,

Burkard Hillebrands

Kaiserslautern, November 2002

Chapter 2: Personnel

2.1 Members of the Group

Group leader:

Prof. Dr. Burkard Hillebrands

Senior scientists:

Dr. habil. Sergej Demokritov, Hochschuldozent
Dr. habil. Jürgen Fassbender, Privatdozent
Dr. Kurt Jung, Akad. Direktor

Postdocs:

Dr. Mireia Blanco-Mantecón	since 03/02
Dr. Vladislav Demidov	since 09/02
Dr. Marc Rickart	since 08/02
Dr. Alexander Serga	since 08/01
Dr. Thomas Wittkowski	since 08/02

PhD students:

Dipl.-Phys. Andreas Beck	since 09/01
Dipl.-Phys. Lisa Kleinen (Rheinbreitbach)	since 10/00
Dipl.-Phys. Radek Lopusnik	until 11/01
Dipl.-Phys. Tim Mewes	since 05/99
Dipl.-Phys. Astrid Müller	until 10/02
Dipl.-Phys. Hans Nembach	since 05/00
Dipl.-Phys. Stefan Poppe	since 03/99
Dipl.-Phys. Marc Rickart	until 07/02
Dipl.-Phys. Thomas Wittkowski	until 07/02

Diploma Students:

Christian Bayer	since 10/01
Gerd Distler	until 07/02
Martin Lesmeister	until 04/02
Markus Weber	until 10/02

Engineers and Technicians

Dipl.-Ing. (FH) Mathias Mautner	until 12/01
Günther Moog (Rheinbreitbach)	since 02/02
Bernd Pfaff	
Dipl.-Ing. (FH) Dieter Weller	since 04/02

Secretary:

Sibylle Müller
Heike Schuster (Schwerpunkt Materialwissenschaften)

2.2 Visiting Scientists, Postdoctoral Fellows and Exchange Students

Dr. Alexander Serga, Radiophysical Faculty, Taras Shevchenk
Kiev University, Kiev, Ukraine — since 08/01

Alexander is working on the problem of nonlinear spin waves financed by a DFG project. In particular he works on time resolved Brillouin light scattering and experiments for parametric pumping of wave packets.

Dr. Loris Giovannini, Istituto Nazionale per la Fisica della Materia (INFM)
and Dipartimento di Fisica, Universita di Ferrara, Ferrara, Italy — 22.11.01 - 30.11.01

Loris is working on the simulation of Brillouin spectra from phonon and spin-wave excitations in layered and structured materials. The main focus of his engagement was the analysis of phonon Brillouin spectra in nanoporous transparent single layer films including surface and bulk excitations and the surface phonon spectra of transparent boron nitride bilayer films.

Miguel Angel Niño, Ph.D Student, Department of Physics of Condensed
Matter, Universidad Autonoma de Madrid — 15.01.02 - 05.02.02

Miguel has been working in our lab and participating in our research of molecular beam epitaxy of thin magnetic films. During this time he has learned the technology of thin film growth on Cu(001) buffers prepared on MgO substrates.

Seong-Gi Min, student, Department of Physics, Chungbuk Nat,
Chungbuk, South Korea — 01.03.02 - 17.08.02

Seong-Gi spent six months in Kaiserslautern investigating non-linear and parametrical interactions of spin waves with a microwave electromagnetic field. The main scientific results of his work are connected with the realization and study of phase control of non-adiabatic parametric amplification of propagating spin wave packets in ferrite films. He was supported through the Seoul University Foundation.

Dr. Mireia Blanco-Mantecón, Magnetic Materials Research Group,
University of Wales, Bangor, United Kingdom — since 03/02

Mireia is working in the field of magnetization dynamics. She is especially involved in setting up a time-resolved photoemission electron microscope.

Prof. Robert L. Stamps, Department of Physics,
University of Western Australia, Perth, Australia — 06.05.02 - 10.05.02

Bob spent a short research stay in Kaiserslautern. He helped a lot in understanding ion irradiation induced modifications of the exchange bias effect. He was also involved in the interpretation of magnetization dynamics results.

Prof. J. Darrel Comins, Department of Physics,
University of the Witwatersrand, Johannesburg, South Africa 06.05.02 - 17.08.02

Darrell spent one half of his sabbatical with us in Kaiserslautern, supported by the DAAD. He was involved in Brillouin light scattering from surface phonons in hard coatings. An intense exchange of experience in this field led to the very successful completion of measurements on stepped tungsten carbide films. Experiments to investigate the temperature dependence of thin film elastic behavior and to monitor phase transitions were brought on their way.

Prof. Andrei Slavin, University of Rochester, Michigan, U.S.A. 01.06.02 - 22.06.02

Andrei spent a short research stay in our lab. He was heavily involved in the modelling of localized modes of spin wave wells created in confined magnetic objects.

Dimitry Kholin, Ph.D. student, Institute for Physical Problems,
Moscow, Russia 20.06.02 - 31.10.02

Dimitry is working on the fundamental properties of biquadratic and non-collinear coupling in layered magnetic systems. He investigates the interplay between the type of the coupling and the morphology of interfaces.

Dr. Vladislav Demidov, St. Petersburg, Russia since 09/02

Vladislav has just started his work in our lab. His research is devoted to dynamics of current induced magnetic switching.

Dr. Mikhail Kostylev, Electronics Faculty,
St. Petersburg Electrotechnical University St.Petersburg, Russia 19.09.2002 - 31.10.02

Mikhail is working on the problem of nonlinear spin waves financed by a DFG project. In particular he works on theory of spin-wave waveform parametric amplification and generation in magnetic films and magnetic-film-based active resonators by using pulsed microwave parallel magnetic pumping.

2.3 Guest Seminars

Dr. L. Giovannini 22.11.01	Istituto Nazionale per la Fisica della Materia (INFM) and Dipartimento di Fisica, Universita di Ferrara, Ferrara, Italy *Brillouin cross section from spin waves: Calculation for magnetic films and multilayers* Sonderseminar Schwerpunkt Materialwissenschaften
Prof. Dr. R.L. Stamps 06.05.02	University of Western Australia, Australia *Stability of domains and pinning near the ferromagnet/anti-ferromagnet interface* Sonderseminar
Dr. S. Kaka 10.05.02	NIST, Boulder, Colorado, USA *Switching dynamics in sub-micrometer spin-valves* Sonderseminar
Prof. J.D. Comins 27.05.02	Department of Physics, University of Witwatersrand, Johannesburg, South Africa *BLS studies on the elasticity of opaque materials* Sonderseminar
Dr. Yves Roussigné 17.06.02	LPMTM, Institut Galilée, Université Paris *Spin wave profiles, eigen frequencies and Brillouin intensities in nanostructures* Sonderseminar
Dr. Mark Stiles 28.06.02	NIST, Gaithersburg, Maryland, USA *Transport of spin in magnetic multilayers* Sonderseminar Schwerpunkt Materialwissenschaften
Prof. Paul Crowell 22.07.02	University of Minnesota, USA *Real-time spin dynamics in patterned films* Sonderseminar
Dr. C.M. Flannery 04.10.02	Materials reliability division at NIST, Boulder, Colorado, USA *Surface acoustic waves for materials characterisation* Sonderseminar Schwerpunkt Materialwissenschaften
T. Hempel 22.08.02	Universität Bielefeld, Germany *GMR – Theorie und Experiment* Sonderseminar
Dr. M. Kostylev 21.10.02	St. Petersburg Electrotechnical University, Russia *Spin wave spectrum and spin wave excitation on thin metallic-film structures* Sonderseminar

2.4 Visits of Group Members at other Laboratories

M. Weber	LPS, Université Paris-Sud 22.-30.11.01 Host: Dr. J. Ferré
T. Mewes	University of Western Australia 12.11.01-22.12.01 Host: Prof. R.L. Stamps
M. Blanco-Mantecón	CEA Saclay, France 21.04.-08.05.02 Host: Dr. C. Fermon
S.O. Demokritov	University of Hamburg, Germany 26.05.-29.05.02 Host: Prof. R. Wiesendanger
S.O. Demokritov	ETH, Zürich, Switzerland 07.07.-09.07.02 Host: Prof. D. Pescia

2.5 Group Member Photo Gallery

Christian Bayer
Diploma student

Andreas Beck
Ph.D. student

Dr. Mireia Blanco-Mantecón
Guest scientist

Dr. Vladislav Demidov
Guest scientist

Dr. habil. Sergej Demokritov
Senior scientist and lecturer

Gerd Distler
Diploma student

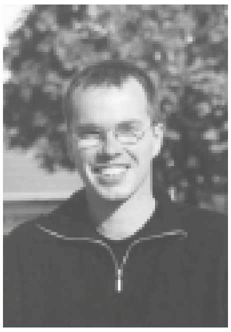

Dr. habil. Jürgen Fassbender
Senior scientist and lecturer

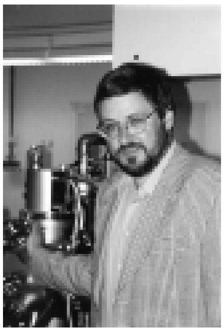

Prof. Dr. Burkard Hillebrands
Group leader

Dr. Kurt Jung
Senior scientist

Lisa Kleinen
Ph.D. student

Martin Lesmeister
Diploma student

Radek Lopusnik
Ph.D. student

Mathias Mautner
Mechanical engineer

Tim Mewes
Ph.D. student

Günther Moog
Technician

Astrid Müller
Ph.D. student

Sibylle Müller
Secretary

Hans Nembach
Ph.D. student

Bernd Pfaff
Technician

Stefan Poppe
Ph.D. student

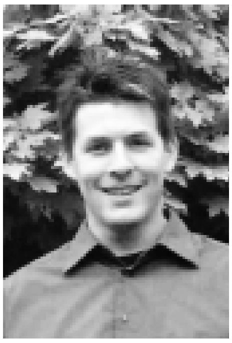

Marc Rickart
Postdoc

Heike Schuster
Secretary

Dr. Alexander Serga
Guest scientist

Markus Weber
Diploma student

Dieter Weller
Mechanical engineer

Thomas Wittkowski
Postdoc

Chapter 3: Research Topics

The field of magnetism in films and multilayers is currently one of the strongest developing areas in modern solid state physics. This is caused both by the challenging developments in the discovery and understanding of the basic physical phenomena, and by the strong impact into industrial applications in the areas of sensors and information storage technology. New mechanisms like interlayer exchange coupling, the giant magnetoresistance effect, the room-temperature tunneling magnetoresistance effect, and, since very recently, spin current phenomena were discovered all within the last one and a half decade. Applications based on these effects were developed, like the magnetic read head based on the giant magnetoresistance effect found in nearly every hard disk drive sold nowadays. The combination with microelectronics, the so-called field of magnetoelectronics is strongly expanding and bridging the gap between conventional magnetism and semiconductor physics in view of potential applications in sensor devices and magnetic random access memories.

Most of our research projects are in this field. We fabricate epitaxial layers and multilayers and study their structural, magnetic and magneto-transport properties.

A main focus is in the field of spin dynamics. We study the eigen-frequency spectrum of excitations of the magnetization on the frequency scale using the Brillouin light scattering technique, and the temporal evolution by time resolved magneto-optic methods. We investigate high frequency properties like linear and nonlinear spin waves including parametric processes, time dependent magnetization effects, and fast magnetic switching.

A key issue is the fabrication of high-quality epitaxial film and multilayer systems and devices using molecular beam epitaxy as prototype systems to study fundamental problems.

In the field of applications we address problems of fast magnetic switching, the exchange bias effect and tunneling magnetoresistance. We transfer our results into actual devices by working closely together with industrial partners.

As a second working area we develop and investigate carbon films for medical applications in the framework of the Institute for Thin Film Technology in Rheinbreitbach. A special focus is on the determination of elastic properties of hard coating materials.

Overview on projects

1) **Epitaxial magnetic films and multilayers: growth, structure and magnetic properties**

   The preparation of samples with highest possible structural quality and characterization is very important to be able to study magnetic phenomena with the necessary precision. We achieve this by using molecular beam epitaxy employing the standard *in-situ* methods for chemical and structural analysis. They comprise Auger spectroscopy for chemical analysis, low and high energy electron diffraction, and *in-situ* scanning tunneling and atomic force microscopy. To characterize the magnetic properties we perform *in-situ* Brillouin light scattering spectroscopy and magneto-optic Kerr effect magnetometry. *Ex-situ*, the samples are investigated using Brillouin light scattering, vector Kerr magnetometry, vibrating sample magnetometry, and more. Scientific subjects are magnetic anisotropies induced at interfaces and by controlled defects, and interlayer coupling effects between magnetic films in multilayers. Special attention is paid to the interplay between the morphology at the interfaces (atomic defects, steps, roughness and interdiffusion) and the magnetic properties. For example, magnetic films grown on vicinal substrates representing templates with arrays of ordered atomic steps are a prototype system for a direct investigation of such interplays.

2) Exchange bias systems

The investigation of exchange bias systems is of fundamental as well as technological importance. The effect is a shift of the hysteresis loop along the field axis, and it appears in multilayers of coupled ferromagnetic and antiferromagnetic films. We study in particular structurally well characterized epitaxial bilayers. The role of defects and interfacial mixing is investigated using ion irradiation in order to artificially create disorder. Ion irradiation techniques are also applied to modify the magnitude and direction of the exchange bias field. This is of high technological interest, especially for magnetic sensor applications.

3) Tunneling magnetoresistance

A magnetoresistive tunnel device is basically a three-layer sandwich system consisting of two ferromagnetic electrodes separated by a very thin ($\approx 1\,\text{nm}$ thick) insulating barrier. The structure changes its electrical resistance (up to 50 % at room temperature) according to the relative orientation of the magnetizations of the two electrodes with respect to each other. Its properties depend dramatically on the homogeneity and quality of the barrier layer. We investigate transport phenomena based on the magnetic tunneling effect with the aim to develop a new generation of magnetic sensors and nonvolatile memories. In a dedicated project we put special emphasis on the development of new methods for the preparation of the barriers and for the investigation of their crystallographic and chemical structures. We have introduced and developed a technology for preparation of thin oxide and nitride layers as tunnel barriers using low energy beams of ionized atomic oxygen/nitrogen. Monoenergetic, low-energy atomic oxygen ions are embedded into an Al film and allow for a very homogeneous formation of the tunnel barrier. Of particular interest are, e.g., the chemical and physical processes taking place during the preparation of the barriers.

4) Magnetic nanopatterning

Light ion irradiation is an excellent tool to locally modify magnetic properties on the submicrometer scale, without affecting the surface topography. This effect is used to magnetically pattern ultrathin films and multilayers using resist masks patterned by electron beam lithography. The major difference between this technique and conventional lithographic techniques is that the environment of the nanostructures can also be magnetic (paramagnetic, antiferromagnetic).

5) Dynamic magnetic properties of laterally patterned nanostructures

We investigate the basic magnetic properties of systems patterned on the micrometer to nanometer scale. In particular we focus on the domain structure and the change in the spin wave mode spectrum due to lateral confinement effects. We have developed a Brillouin light scattering setup, operating in a Fourier microscope like mode, to obtain sub-micrometer scale spatial information about the distribution of dynamic excitations in small magnetic objects. Using this method we have observed lateral quantization of spin waves in magnetic stripes and rectangular elements. Main results are the observation of quantized modes and of edge modes existing in areas with a large internal field gradient, and static and dynamic coupling effects between magnetic objects.

6) Nonlinear properties of microwave excited spin waves

Spin waves with high precession angles, which can be excited using microwave stripe lines, are an interesting object for the investigation of general effects of nonlinear wave propagation in dipersive, anisotropic, and dissipative media. Contrary to nonlinear optical pulses the spectrum of spin waves can be easily manipulated, by, e.g., changing the orientation and the value of the applied magnetic field. In addition spin waves are much slower than light pulses making their observation easier.

Using the time resolved Brillouin light scattering technique developed in our lab, we measure the intensity distribution of spin waves propagating in a magnetic film with spatial and temporal resolution. Central problems are: the propagation of spin waves in the linear and nonlinear intensity regimes, the formation of instabilities (e.g. self-focusing), the propagation of nonlinear excitations (solitons, magnetic “bullets”) and collision experiments of these excitations. An important development of these studies is the investigation of self-generation of solitons and bullets in loops with a feedback and the development of a spin wave soliton “laser”.

7) Fast magnetic switching

For memory devices it is of special importance how fast and secure magnetic domains can be written or the magnetization of a single magnetic object can be reversed. The corresponding time scale is in the picosecond to nanosecond regime. In order to investigate these phenomena a time-resolved scanning magneto-optic Kerr microscope has been constructed. The time evolution of the magnetization is sensed stroboscopically. The magnetization dynamics and in particular the switching behavior of thin magnetic films and nanostructures is investigated.

8) Numerical simulations

Numerical simulations are used for several aspects. i) The evolution of the magnetization upon pulse field application is calculated and compared to the results of time-resolved magneto-optic Kerr effect experiments. ii) Quasi static switching properties like the modification of the well known Stoner astroid by additional anisotropy or coupling contributions are studied. iii) The magnetization reversal behavior of epitaxial exchange bias layers is investigated with respect to different anisotropy contributions.

9) Elastic properties of hard, super-hard and inhomogeneous films and multilayers

We prepare hard and super-hard films and investigate their elastic properties using Brillouin light scattering. Research subjects are amorphous carbon (a-C:H and ta-C:H) and boron nitride films, which are prepared using unbalanced magnetron sputtering. The elastic constants are determined from the dispersion curves of surface and film phonons (Rayleigh and Sezawa modes). One of our aims is to prepare hard and super-hard films with minimized internal stresses.

10) Biofunctionalized surfaces for medical applications

Amorphous thin carbon films are known to be very biocompatible, and they can be prepared by various deposition techniques to qualify for miscellaneous applications in the biological and medical field. At the Institute for Thin Film Technology we develop in close collaboration with our spin off company NTTF GmbH biocompatible and biofunctionalized surfaces for medical implants and surgical instruments. Currently we are working on carbon coatings for intraocular lenses, cardiovascular stents and orthopedic implants as well as on the development of low temperature coating processes for temperature sensitive materials.

Chapter 4: Equipment

A) Preparation and characterization of thin films and multilayers

1. multi–chamber molecular beam epitaxy system (Pink GmbH) comprising
    a. deposition chamber
    (electron beam and Knudsen sources, RHEED, LEED, Auger)
    b. scanning tunneling and atomic force microscopy chamber
    (*in-situ* STM/AFM, Park Scientific)
    c. Brillouin light scattering and Kerr magnetometry chamber
    (magnetic field 1.2 T, temperature range 80 – 400 K)
    d. load lock chamber
    e. preparation chamber
    (optical coating, heating station 2300°C)
    f. transfer chamber
    g. atom beam oxidization chamber with *in-situ* four-probe resistively measurement stage
2. two-chamber UHV multideposition system
    a. deposition chamber
    (electron beam and Knudsen sources, LEED, Auger)
    b. ion beam sputtering chamber with ion beam oxidation module and mask system
3. two-chamber UHV deposition system with *in-situ* 5 keV ion beam irradiation station
4. two-magnetron sputtering system
5. two atomic force microscopes (TopoMetrix and Solver, NT-MDT)
6. clean room facility with flow box, spin coater, etc.

B) Magnetic characterization

1. vibrating sample magnetometer with alternating gradient magnetometer option
(magnetic field 1.6 T, room temperature)
2. vibrating sample magnetometer
(magnetic field 5 T, temperature range 2 – 350 K)
3. two vector Kerr magnetometer
(longitudinal and transverse Kerr effect, magnetic field 1.2 T, temperature range 2 – 350 K, automated sample positioning)
4. high-field polar Kerr magnetometer
(magnetic field 5 T, temperature range 2 – 350 K)
5. Kerr magnetometer with time resolution and setup for generation of short field pulses
6. scanning Kerr microscope with time resolution
7. magnetic force microscope with magnet (NT-MDT)

8. two Brillouin light scattering spectrometers, computer controlled and fully automated (magnetic field 2.2 T) with stages for
   a. low temperature measurements (2 – 350 K)
   b. space-time resolved measurements for spin wave intensity mapping (resolution 50 µm, 0.83 ns)
   c. *in-situ* measurements
   d. elastic measurements
9. microwave setup (up to 32 GHz) comprising a network analyzer, microwave amplifiers, modulators, pulse generators, etc.
10. magnetotransport setups (magnetic field 1.5 T, temperature range 20 – 400 K)

C) Equipment at the Institute for Thin Film Technologies (IDST), Rheinbreitach

1. Preparation of thin films:
   a. chemical vapor deposition (CVD) facility
   b. physical vapor deposition (PVD) facility
   c. plasma enhanced CVD (PECVD) facilities with an inductively coupled rf-plasma beam source and several magnetrons of different sizes
2. Surface and thin film analysis:
   a. profilometer: measurement of coating thickness and roughness determination of intrinsic stress and Young modulus
   b. Ball on Disk: measurement of friction coefficient analysis of surface friction
   c. Revetest: determination of adhesive strength analysis of microcracks
   d. microindention: determination of plastic and elastic microhardness (Vickers)
   e. optical contact angle measurement: determination of solid surface free energy and surface tension evaluation of hydrophobicity and hydrophilicity
   f. reflection- and transmission-spectroscopy (UV-VIS): optical measurements with wavelength range from 185 nm to 915 nm (resolution 1 nm), determination of absorption coeffizient and optical gap (Tauc)
   g. (environmental) scanning electron microscopy (ESEM)[1] : comprehensive structural microanalysis of conducting, isolating, anorganic, organic and wet samples
   h. energy dispersive X-ray microanalysis (EDX)[1]: non-destructive fast analysis of elements
   i. neutron activation analysis (NAA)[2] : qualitative und quantitative analysis of main and trace components
   j. elastic recoil detection analysis (ERDA)[2]: analysis of trace elements with depth resolution analysis of hydrogen content
   k. Rutherford Backscattering (RBS)[2]: analysis of trace elements with depth resolution
   l. synchrotron-X-ray-fluorescence (SYXRF)[2]: non-destructive analysis of elements

---

[1] in cooperation with NTTF GmbH, Rheinbreitbach

[2] accelarator enhanced analysis in cooperation with the accelarator laboratories of the Universities of Munich, Bonn and Cologne

Chapter 5: Transfer of Technology

1. Magnetism

With our facilities within the Department of Physics at the University of Kaiserslautern we offer consultance and transfer of technology in the areas of thin film magnetism, magnetic film structures and devices, magnetic sensors, and in corresponding problems of metrology.

We are equipped to perform magnetic, transport, elastic and structural measurements of films and multilayer systems.

This is in detail:

- magnetometry (magnetic field up to 5 T, temperature range 2 - 400 K) using vibrating sample magnetometry, Kerr magnetometry, Brillouin light scattering spectroscopy
- magnetic anisotropies, optionally with high spatial resolution
- magneto-transport properties
- test of homogeneity of magnetic parameters
- exchange stiffness constants in magnetic films
- elastic constants
- surface topography

2. Institut für Dünnschichttechnologie (IDST) - Transferstelle der Universität Kaiserslautern, Rheinbreitbach

(Institute for Thin Film Technology - Center for Technology Transfer of the University of Kaiserslautern, Rheinbreitbach)

As part of technology transfer the Institute of Thin Film Technology (IDST) offers among other activities

- consultance in tribological problems
- development of product specific coatings
- optimization of coatings especially for medical applications
- coating of samples and small scale production series
- management for R&D-projects

The institute is located in Rheinbreitbach about 20 km south of Bonn in the Center for Surface Technologies (TZO) to support the economy in the northern part of the Rheinland-Pfalz State.

Address:

Institut für Dünnschichttechnologie
Maarweg 30
53619 Rheinbreitbach, Germany

Scientific director:

Prof. Dr. B. Hillebrands	phone:	+49 631 205 4228
	e-mail:	hilleb@physik.uni-kl.de

Contact:

Dr. K. Jung	phone:	+49 631 205 2278
	e-mail:	jung@physik.uni-kl.de

Representative in Rheinbreitbach:

Lisa Kleinen	phone:	+49 2224 900 693
	fax:	+49 2224 900 694
	e-mail:	kleinen@physik.uni-kl.de

Please contact us for more information.

Chapter 6: Experimental Results

A. Dynamic Magnetic Phenomena

6.1 Spin wave wells with multiple states created in small magnetic elements

C. Bayer, S.O. Demokritov, and B. Hillebrands[1]

For a non-ellipsoidal magnetic element the internal static magnetic field H_i is usually strongly inhomogeneous. We consider a thin long stripe of rectangular cross section magnetized along its width. For zero or weak external field strengths, areas near the side walls of the stripe show a canting of the magnetization away from the mean direction, and the corresponding internal field is zero due to compensation of the external and the demagnetizing field. For weak fields the internal field can be zero across the entire stripe. With increasing field and above a critical field strength H^* the internal field becomes nonzero in the center of the stripe, still coexisting with $H_i = 0$ regions near the stripe walls.

Here we are interested in the dynamic properties, i.e. the spectrum of eigen excitations in such an inhomogeneous system. As a function of position within the stripe, the internal magnetic field H_i undergoes especially sharp changes near the boundary between the zero-field and the saturated region in the middle of the stripe. This strong inhomogeneity causes spin wave localization in so-called “spin wave wells” (SWW), which has been recently observed by means of Brillouin light scattering (BLS) [1] and later confirmed by time-resolved Kerr effect microscopy [2].

The investigated samples were prepared from thermally evaporated permalloy films. Patterning was performed by means of e-beam lithography. Stripes with a width of 1 μm, a length of 90 μm, and a thickness of 33 nm were prepared.

Thermally excited spin waves were investigated using BLS in the backscattering geometry. In all experiments the magnetic field and the wavevector **q** transferred in the light scattering process lie in the plane of the sample and were oriented perpendicular to the long axis of the stripe. The wavevector was varied in the range $(0-2.2)\cdot 10^5\,\mathrm{cm}^{-1}$, while the external magnetic field H_e was varied in the range $(0-1.1)\,\mathrm{kOe}$.

Figure 1 shows a typical BLS spectrum for a transferred wavevector $q = 0.47\cdot 10^5\,\mathrm{cm}^{-1}$ and an external field of $H_e = 800\,\mathrm{Oe}$. As it is seen, the spectrum contains several peaks corresponding to spin wave modes. The high frequency peaks can be identified as the exchange dominated perpendicular standing spin wave modes (PSSW or thickness modes), existing in the saturated central region of the stripe, where the internal field is close to $H_i = 600\,\mathrm{Oe}$, and a similar mode existing in unsaturated regions near the stripe edges ($y = \pm\, 0.5\,\mu\mathrm{m}$), where the effective internal field is close to $H_i = 0$. In the low frequency region one can see three distinct peaks. The strongest broad peak near 8 GHz corresponds to a band of non-localized quantized spin wave modes [1]. The two peaks with the lowest frequencies are localized spin wave modes corresponding to two spin wave eigenstates of the SWW created by a strongly inhomogeneous internal field near the boundaries between the saturated and unsaturated regions.

---

[1] In collaboration with A.N. Slavin, Department of Physics, Oakland University, USA, and C. Fermon and M. Bailleul, CEA Saclay, France.

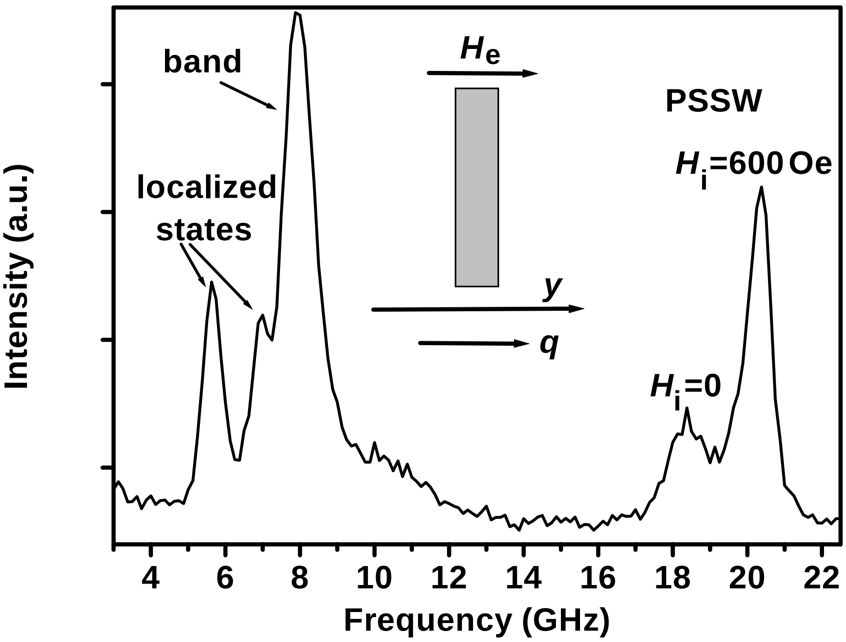

Fig. 1: BLS spectrum for a transferred wavevector $q = 0.47 \cdot 10^5\,\mathrm{cm}^{-1}$ and an external field of $H_e = 800\,\mathrm{Oe}$. PSSW indicates the perpendicular standing spin wave (thickness mode). The inset shows the used experimental geometry.

The formation of the SWW can be understood as follows: let us consider a spin wave of frequency ν_0, propagating within the saturated region ($\mathbf{H}_i \| \mathbf{M}_S \| \hat{y}$) towards the center of the stripe (wavevector $\mathbf{q} \| \hat{y}$). With changing $H_i(y)$ the wave changes its wavevector to fulfill the dispersion equation $\nu_0 = \nu(\mathbf{q}(y), H_i(y))$ [3]. The wave, however, will be reflected at the point $y = y_l$, where H_i becomes so large, that no solution $\nu_0 = \nu(\mathbf{q}, H_i)$ with a real $\mathbf{q}$ exists anymore. The wave will also be reflected when it enters the zero-field region, since in this region the static magnetization rotates away from the direction of H_e.

Figure 2 shows the dependence of the observed frequencies on the external field H_e. While the magnitude of H_e is small and not sufficient to saturate the stripe, the internal field is zero across the stripe and only a single PSSW mode corresponding to $H_i = 0$ is present in the spectrum. At some critical field $H_e = H^*$ the PSSW peak begins to split. The first peak corresponding to $H_i = 0$ retains its frequency, but looses intensity with increasing H_e. The frequency of the second peak (which appears at $H_e = H^*$) increases with the applied field, indicating the increase of H_i in the central part of the stripe. The observed value of the critical field $H^* = 220\,\mathrm{Oe}$ is in agreement with the calculated demagnetizing field in the stripe center, $H_d(y = 0)$, based on the approach presented in [4]. Static magnetometry also shows a sharp increase of the stripe magnetic moment for $H_e > H^*$, indicating partial magnetic saturation of the stripe.

Describing the low-frequency part of the observed spectrum, it should be mentioned that for $H_e < H^*$ one observes several Damon-Eshbach modes quantized due to confinement in the stripe. They are not presented in Fig. 2 for the sake of clarity.

For $H_e > H^*$ a broad band of non-resolved spin wave excitations is seen in the experimental spectra [1]. At higher H_e at first one and then more narrow peaks are observed in addition to the band. One such peak has been observed previously and has been identified as a localized state in the spin wave well (SWW).

To understand the appearance of several well-resolved spin wave modes corresponding to the multiple states in a SWW, one should take into account that the depth of the well strongly depends on H_e. In fact, the bottom of the well corresponds to $H_i = 0$ independently of H_e. The field, which determines the position of the top of the well, however, can be roughly estimated as

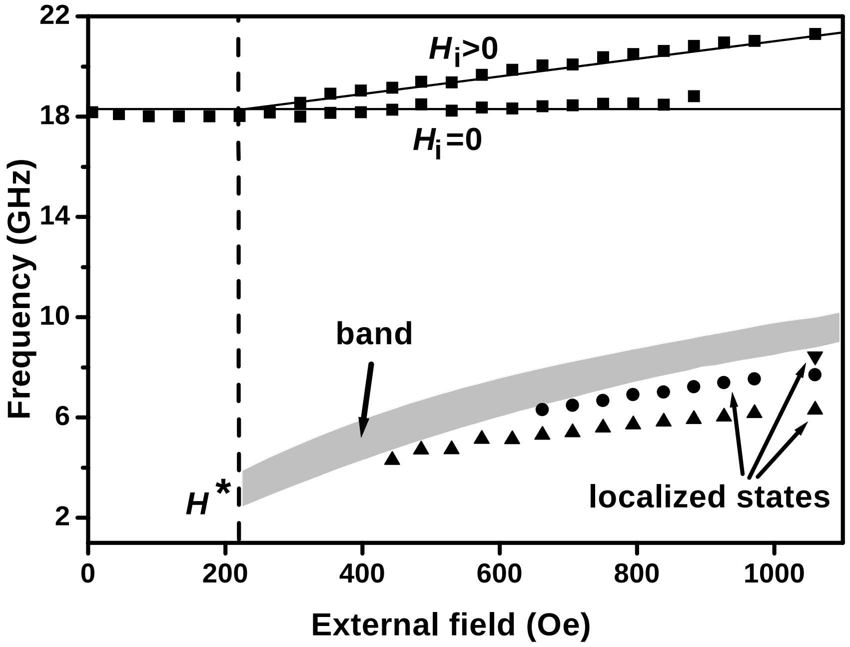

Fig. 2: Frequencies of the modes observed in the stripes at $q = 0.47 \cdot 10^5\,\text{cm}^{-1}$ as a function of H_e. The vertical dashed line marks the critical field H^*. Note the constant frequency of one PSSW mode and the increase in frequency for the other mode for $H_e > H^*$. The gray region illustrates the band of non-resolved quantized excitations.

$H_e - H_d(y = 0) \approx H_e - H^*$. For a small difference $H_e - H^*$ the well is too shallow, and there is no room in the well for a localized spin wave state. With increasing H_e the well becomes deeper, and as a result of that, at first one, and then more localized spin wave states appear in the well.

The quantization condition for localized spin wave states in a SWW can be written in analogy to the quasi-classical quantization condition in a potential well in quantum mechanics. It states that the total frequency shift of a wave propagating from one turning point to another and then returning back is a multiple of 2π;

$$\Delta\phi_l + \Delta\phi_r + 2 \times \int_{y_l}^{y_r} q(H_i(y), \nu)dy = 2n\pi \quad , \tag{1}$$

where $n = 1, 2, 3....$ $\Delta\phi_l, \Delta\phi_r \in [0, \pi]$ are the phase jumps at the left and right turning points, respectively. Henceforth we will call the third term in (1) the quantization integral. Note, that since the dispersion of the spin waves differs from that of an electron, the results for the phase jumps obtained for an electron in a quantum well may not be used for SWW. The calculation of $\Delta\phi$ for SWW is a challenge for the wave theory. However, the difference between the quantization integrals calculated for two successive modes should be equal to 2π, if $\Delta\phi_l$ and $\Delta\phi_r$ are the same for all the localized modes.

To determine the turning points and the quantization integrals for the different spin wave states in the SWW, the profile of H_i in the saturated region (see solid curve in Fig. 3) has been calculated using the approach proposed in [4]. The equation $\nu = \nu(q(y), H_i(y))$ [5] has been numerically solved for the experimentally measured values of ν. As it is discussed above, the point, where a solution $q(y)$ disappears for real $q(y)$, is the turning point. The second turning point was assumed to be at the boundary between the saturated and zero-field regions. Based on the obtained dependencies $q(y)$ the quantization integrals for the modes have been calculated.

The main results of the calculation can be summarized as follows: a) The calculated quantization integrals for the localized states in the SWW decrease with increasing external field, probably due to the field dependence of $\Delta\phi_l, \Delta\phi_r$. b) The localization length $\xi = y_r - y_l$ is about 50 nm for the

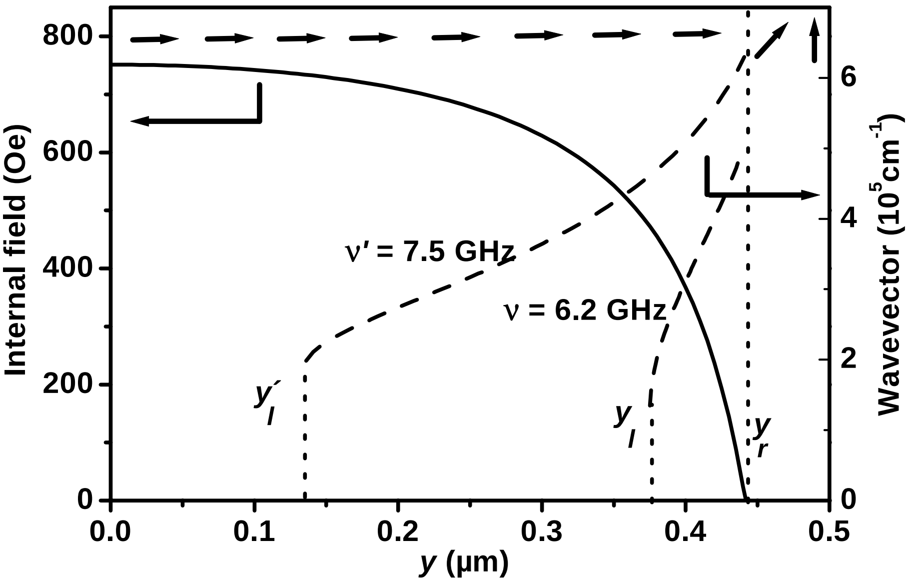

Fig. 3: Internal field (solid line) and wavevector of the observed states (dashed lines) calculated as functions of y for an applied field of 970 Oe. y_l,y_l', and y_r are the turning points of the localized modes with the frequencies as indicated. The arrows at the top of the figure illustrate the orientation of the static magnetization.

lowest localized state and $200-300$ nm for the states having higher frequency. The localization lengths decrease with increasing H_e. c) Although the quantization integrals for the two lowest localized modes depend on H_e, their difference is almost constant and equal to $(4.2\pm0.4)\,\pi$. This is a direct confirmation of the applicability of the quasi-classical quantization condition Eq. (1) to the spin wave modes localized in a SWW.

The fact that the difference between the quantization integrals corresponding to the two lowest localized spin wave states in the SWW is close to 4π (and not to 2π) suggests that we see two odd-numbered modes ($n=1$ and $n=3$) having a similar (symmetrical) distribution of the spin wave intensity about the center of the well. The reason why we see only the symmetric modes in the BLS experiment is related to the strong spatial localization of these modes: $q\xi \ll 1$, where $q=(1-2)\cdot 10^5\,\mathrm{cm}^{-1}$ is a typical wavevector transferred in the BLS process. This inequality means that the light fields are practically homogeneous on the spatial scale of the spin wave mode localization length and, similar to the case of standing spin wave resonance experiments [6], only the odd (symmetric) spin wave states contribute to the observed BLS intensity.

We thank P. Crowell for communicating his results prior to publication. Support by the Deutsche Forschungsgemeinschaft is gratefully acknowledged. C. B. acknowledges support by the Studienstiftung des Deutschen Volkes.

References

[1] J. Jorzick, S.O. Demokritov, B. Hillebrands, D. Berkov, N.L. Gorn, K. Guslienko, A.N. Slavin, Phys. Rev. Lett. **88**, 047204 (2002).
[2] J.P. Park, P. Eames, D.M. Engebretson, J. Berezovsky, P.A. Crowell, submitted to Phys. Rev. Lett. (2002).
[3] E. Schlömann, J. Appl. Phys. **35**, 159 (1964).
[4] R.I. Joseph, E. Schlömann, J. Appl. Phys. **36**, 5 (1965).
[5] B.A. Kalinikos, A.N. Slavin, J. Phys. C **19**, 7013 (1986).
[6] C. Kittel, Phys. Rev. **110**, 1295 (1958).

6.2 Numerical simulations for potential polyvalent devices

M. Weber, H. Nembach, and J. Fassbender

Much effort has been put into enhancing the speed, bit density and reliability of magnetic memory devices. In the case of magnetic random access memory (MRAM) devices, fast coherent magnetization rotation by precession of the entire memory cell is desired. In principle, the fundamental limit of the switching speed via precession is given by half of the precession period. Ultrafast precessional switching was shown by simulations [1,2] and recently experimentally by several groups for spin-valve systems [3–5].

Besides storage speed an increasing storage density for precessional switching devices plays an important role in current memory research. One way to solve this problem is making use of anisotropy contributions of higher symmetry to store more than one bit in a memory cell. Polyvalent devices might become feasible in which the final magnetization state is addressed via the duration and direction of a magnetic field pulse in a precessional switching event.

In the following we consider a small, four-fold magnetocrystalline anisotropy, which for instance can be realized experimentally with an epitaxial (001)-oriented permalloy film. Typical parameters used are the Gilbert damping parameter $\alpha = 0.005$ and the saturation magnetization $4\pi M_S = 10.8\,\mathrm{kG}$ [6].

The in-plane x- and y-directions are the easy magnetization directions. Initially the magnetization is oriented along the $+x$-direction and the magnetic field pulse is applied along the $+y$-axis. The field pulse magnitude is 5 Oe and its duration varies between 100 and 500 ps. The pulse rise time is 50 ps and the fall time is 150 ps. All pulse parameters are chosen to be experimentally accessible with commercial electronic pulse generators.

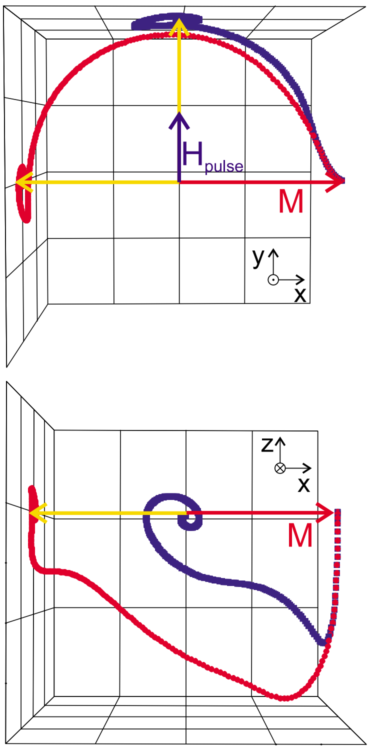

Fig. 1: Magnetization dynamics of an epitaxial (001)-oriented permalloy film ($\mathbf{H}_{ani,cub} = 2\,\mathrm{Oe}$). The initial magnetization and the magnetic field pulse directions are indicated in the graph. For a field pulse duration of 150 ps (300 ps) the data are displayed in black (grey), respectively. The final magnetization directions are indicated in light grey. The z-axis is exaggerated. The magnetization trajectories are presented with a top-view (top) and a side-view (bottom).

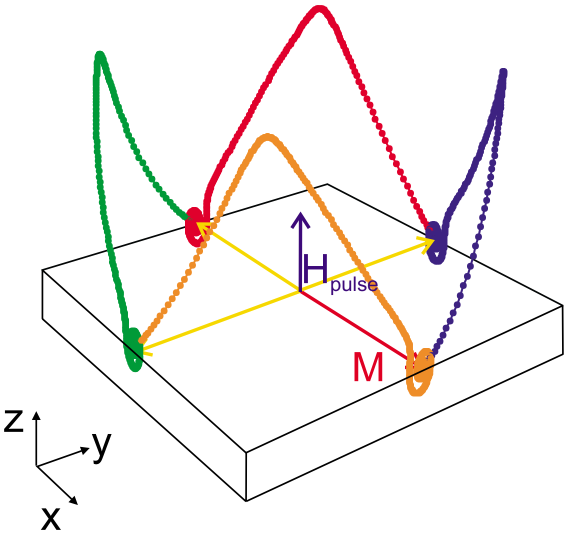

Fig. 2: Magnetization dynamics $\mathbf{M}(t)$ of an epitaxial (001)-oriented permalloy film ($H_{ani,cub}$ = 10 Oe). The field pulses are applied perpendicular to the film plane. Different final magnetization states can be reached by repetitive application of the field pulse. The z-axis is exaggerated.

In Fig. 1 the magnetization trajectories are shown for two different magnetic field pulse durations. For a pulse duration of 150 ps the data are displayed in black; for 300 ps in grey. Since the field pulse is oriented along the $+y$-axis a $-z$-component of the magnetization arises due to the torque acting. This $-z$-component in turn creates a demagnetizing field. The effective field is thus rotated slightly to the $+z$-direction creating a torque on the magnetization in $+y$-direction. For both pulse durations the trajectories are the same until the falling edge of the short field pulse is reached. After the magnetic field pulse is terminated the magnetization movement is governed by the remaining demagnetizing field. Due to the small value of the anisotropy field it affects the trajectory only to a minor degree. The final magnetization state is determined mainly by the energy that is contained in the magnetization state at the time of pulse termination. Depending on the pulse duration the magnetization relaxes either to the $+y$- or x-direction. If the field pulse direction is inverted a final magnetization direction pointing along the $-y$-axis becomes also possible. Thus an adjustment of the magnetic field pulse duration allows one to address different final magnetization states. However in all cases a final relaxation step by magnetic damping is required since the magnetization direction does not exactly align with the corresponding easy axis.

The situation becomes very different if the magnetic field pulse is applied perpendicular to the film plane (see Fig. 2). Since at first no demagnetizing field appears the magnetic field pulse magnitude must be chosen much larger than for in-plane field pulses. Figure 2 shows a simulation for a magnetic field pulse magnitude of 222 Oe. The time structure of the field pulse is 250 ps rise time, 1 ns duration and 750 ps fall time. Again these values are chosen to mimic realistic experimental situations.

First, the torque created by the field pulse leads to an in-plane rotation of the magnetization. The arising contribution of the anisotropy field leads then to a $+z$-component of the magnetization creating a demagnetizing field. Due to the fact that the demagnetizing field and the field pulse have the same symmetry the magnetization trajectory is only influenced by the reduction of the effective field magnitude. If the initial magnetization direction is along the $+x$-direction the magnetization will point close to the $+y$-direction after pulse termination. Thus nearly no relaxation is required to align the magnetization with the easy magnetization direction. Due to the symmetry of the system multiple pulse applications lead to a successive rotation of the magnetization by 90°.

References

[1] J. Miltat, G. Albuquerque, A. Thiaville, in *Spin Dynamics in Confined Magnetic Structures I*, B. Hillebrands, K. Ounadjela (Eds.), Springer-Verlag, Berlin (2002).
[2] M. Bauer, J. Fassbender, B. Hillebrands, R.L. Stamps, Phys. Rev. B **61**, 3410 (2000).
[3] H.W. Schumacher, C. Chappert, P. Crozat, R.C. Sousa, P.P. Freitas, J. Miltat, J. Fassbender, B. Hillebrands, submitted to Phys. Rev. Lett. and cond-mat/0207546.
[4] S. Kaka, S.E. Russek, Appl. Phys. Lett. **80**, 2958 (2002).
[5] Th. Gerrits, H.A.M. van den Berg, J. Hohlfeld, L. Bär, Th. Rasing, Nature **418**, 509 (2002).
[6] M.R. Freeman, W. Hiebert, A. Stankiewicz, J. Appl. Phys. **83**, 6217 (1998).

6.3 Phase coherent precessional switching of microscopic spin-valve elements

J. Fassbender and B. Hillebrands[1]

Here we report a collaboration between the Université Paris Sud, Orsay, where B. Hillebrands has spent a sabbaticcal stay, the Instituto de Engenharia de Sistemas e Computadores (INESC) and the University of Kaiserslautern. The samples have been prepared at INESC, the time resolved magnetoresistance measurements have been performed and analyzed in Orsay, and the numerical simulations were made in Kaiserslautern.

The demand for speed in data processing must be matched by the fast response of memory devices. One promising path is the realization of magnetic random access memory (MRAM): a logical bit is stored in a unit cell of magnetic material by setting the orientation of the magnetization vector inside the cell in one of two possible directions, coding the logical values '0' and '1'. Since a few years much effort has been put on the experimental verification of phase coherent precessional switching.

In November 2001 at the MMM conference in Seattle, U.S.A., three groups have independently shown that precessional switching can be achieved [1–3]. Here we demonstrate that stable, reversible and highly efficient magnetization switching is triggered by transverse field pulses as short as 140 ps with energies down to 15 pJ. At high fields a phase coherent reversal regime is found revealing periodic transitions between switching and non-switching under variation of pulse parameters. At the low field limit the existence of relaxation dominated switching is established allowing precessional magnetization reversal by field amplitudes below the static field threshold.

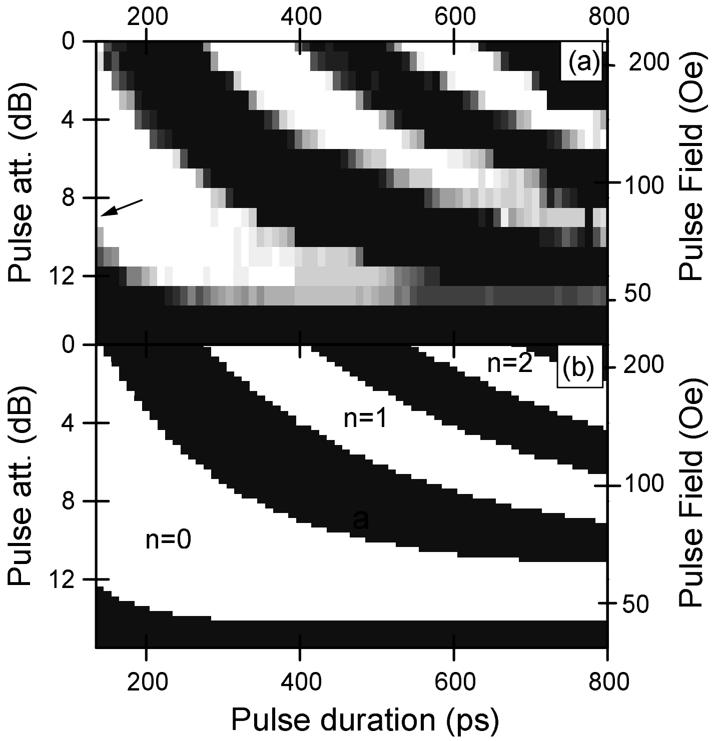

Fig. 1: Pulse field dependence of the precessional switching of the spin-valve cell. (a) $|\Delta GMR|$ as a function of T_{pulse} and H_{pulse}. gray: $|\Delta GMR| \leq 0.1$, white: $|\Delta GMR| \geq 0.8$. H_{pulse} is attenuated in steps of 1 dB. Switching pulse energies are as low as 15 pJ (arrow). (b) calculated switching map for the same device derived from macro spin simulations. Black: no switching, white: switching. The order n of switching is indicated.

---

[1] In collaboration with H.W. Schumacher, C. Chappert, P. Crozat, J. Miltat, Université Paris Sud, France, R.C. Sousa, P.P. Freitas, INESC Lissabon, Portugal.

A characterization of the switching properties over a wide range of H_{pulse} and T_{pulse} is displayed in Fig. 1. The magnetoresistance results are shown in the upper panel and the results of a macro spin simulation based on the model described in [4] in the lower one. Switching of the spin-valve cell is coded in white whereas black denotes non-switching of the cell. In the lower part the order n of the switching is indicated, i. e., the magnetization has undergone $n+0.5$ revolutions. In the upper part also grey values are obtained which indicate incomplete switching of the spin-valve cell. The simulated field dependence of the coherent regimes is in good agreement with the measurements, and the minimum switching field of about 50 Oe is well reproduced. A decrease of H_{pulse} first shifts the switching regions towards larger values of T_{pulse}. This is expected from simple ferromagnetic resonance arguments [5], since the precession period generally increases with decreasing field. Interestingly enough, just above the switching field limit of about 50 Oe, simulations predict $n=0$ switching independent of T_{pulse}. Thus, the coherence criterion appears to be no longer valid. However, now the condition that the pulse field is much larger than the anisotropy field is no longer fulfilled. M will overcome the hard axis only once during pulse application and it will precess around an equilibrium direction defined by the ratio of pulse field and the anisotropy field.

Owing to the damping, an oscillation back across the in-plane hard magnetization axis is inhibited and the x-component of the magnetization changes sign only once. Thus, independently of T_{pulse}, switching will be completed. Note again, that switching can be achieved although the pulse field is smaller than the anisotropy field.

Figure 1 also allows us to find parameters for optimum switching efficiency. Switching is obtained by pulses of T_{pulse}= 140 ps and only 15 pJ energy (arrow), proving high efficiency when compared to conventional easy axis switching schemes [6, 7].

B. H. acknowledges support by CNRS during his sabbatical stay at the Université Paris Sud, Orsay.

References

[1] S. Kaka, S. Russek, Appl. Phys. Lett. **80**, 2958(2002).
[2] T. Gerrits, H.A.M. van den Berg, J. Hohlfeld, L. Bär, Th. Rasing, Nature **418**, 509 (2002).
[3] H.W. Schumacher, C. Chappert, P. Crozat, R.C. Sousa, P.P. Freitas, J. Miltat, J. Fassbender, B. Hillebrands submitted to Phys. Rev. Lett. and /cond-mat/0207546.
[4] M. Bauer, J. Fassbender, B. Hillebrands, R.L. Stamps, Phys. Rev. B **61**, 3410 (2000).
[5] C. Kittel, *Introduction to Solid State Physics,* 5th ed., Wiley, New York (1976).
[6] R.H. Koch, J.G. Deak, D.W. Abraham, P.L. Trouilloud, R.A. Altman, Y. Lu, W.J. Gallagher, R.E. Scheuerlein, K.P. Roche, S.S.P. Parkin, Phys. Rev. Lett. **81**, 4512 (1998).
[7] B.C. Choi, M. Belov, W.K. Hiebert, G.E. Ballentine, M.R. Freeman, Phys. Rev. Lett. **86**, 728 (2001).

6.4 Phase control of non-adiabatic parametric amplification of spin wave packets

A.A. Serga, S.O. Demokritov, and B. Hillebrands[1]

It has been shown earlier, that for packets of dipolar spin waves propagating in a ferrite film it is possible to realize a non-adiabatic regime of parametric pumping interaction, where the pumping field is strongly localized in the region of the order of the spin wave (SW) carrier wavelength [1]. This regime of interaction is particularly important for the amplification of SW envelope solitons, as it allows to realize simultaneous amplification and compression of SW packets and thus to obtain extremely large single-soliton amplification gains of up to 17 dB [2, 3].

Parametric amplification of spin wave solitons is achieved by interaction of propagating SW packets with a pulsed localized electromagnetic pumping field of double frequency [4, 5]. In this process, and in addition to the amplification of the initial spin wave, a new phase conjugated spin wave or so-called “idle” wave is generated. In the non-adiabatic case, as considered here, this “idle” wave co-propagates with the initial spin wave and can lead both to an increase of the amplitude of the output signal by a factor of two or to its suppression as a result of constructive or destructive interference [1]. Thus, if the signal and pumping pulses have random initial phases, interference causes random modulation (beating) of the output amplified signal, which is undesirable for signal processing.

In this contribution we report on the first experimental realization of a fixed-phase non-adiabatic amplification of a SW packet. The output signal is stable, and no beating was observed. We show, that the amplitude of the amplified output pulse can be changed in the range of 15 dB by varying the phase shift between the signal and the pumping waves.

Figure 1 shows a schematic diagram of the experimental setup. Its main part is a spin wave delay line, which consists of a strip of an yttrium-iron-garnet (YIG) film and a pair of short-circuited microstrip antennae. The YIG film is indicated by the gray rectangular strip in Fig. 1. The parameters are: width: 1.5 mm, length: 18 mm, thickness: 5 μm, saturation magnetization $4\pi M_s = 1750\,\mathrm{G}$, ferromagnetic resonance linewidth $2\Delta H = 0.35\,\mathrm{Oe}$.

The antennae are made on one side of a shielded dielectric substrate with dielectric permeability 9.8. They are situated transversely to the long side of the YIG sample and are separated by 8 mm. One of the antennae is used for the excitation of spin waves and the other for their detection after traveling the distance between the antennae. The antennae’s width and length are 50 μm and 2.5 mm respectively. In the middle between the input and the output antenna we placed a thin (50 μm) microstrip pumping transducer which was oriented transversely to the long side of the YIG strip. This transducer was made as a half-wavelength resonator (quality factor 30) connected to the pumping transmission line by a capacitive coupling. Due to the high dielectric permeability of the substrate the pumping microwave field is localized close to the resonator and forms an active area of parametric interaction with length L of the order of several microstrip widths ($50-100\,\mu\mathrm{m}$) in the direction of SW propagation.

A bias magnetic field of $\mathbf{H}_0 = 1850\,\mathrm{Oe}$ was applied along the YIG strip, i.e., along the spin wave propagation direction, as shown in Fig. 1. In this geometry, backward volume magnetostatic waves

---

[1] In collaboration with Seong-Gi Min, Department of Physics, Chungbuk Nat, Cheongju, Chungbuk, South Korea, and A.N. Slavin, Department of Physics, Oakland University, Rochester, Michigan, USA.

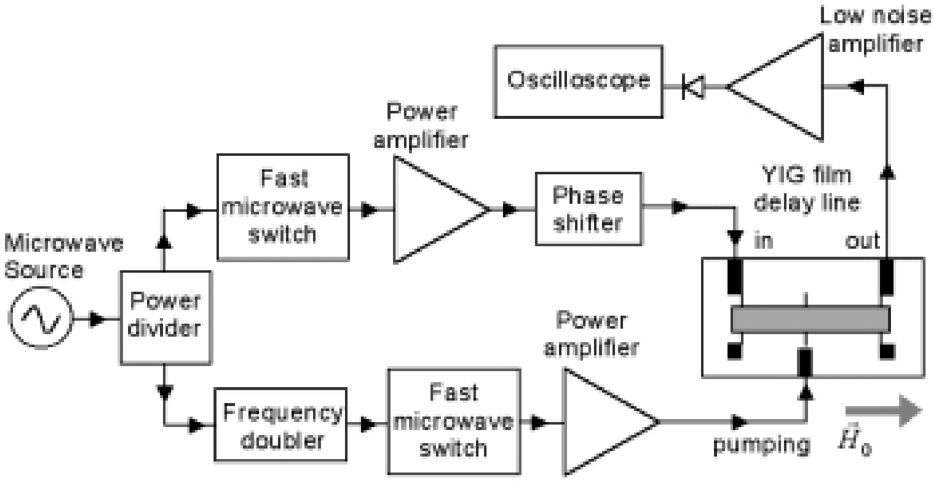

Fig. 1: Schematic diagram of the microwave experimental setup.

(BVMSW) exist and are able to form bright envelope solitons, which can be efficiently parametrically amplified by the external microwave magnetic field. These BVMSW modes are usually used in experiments on parametric amplification of linear and nonlinear spin wave pulses [1–5]. In these experiments linear SW packets were amplified to simplify the situation and to avoid any spurious influence of any nonlinear effects on the amplification process and shape of the output signal. The input SW packet was exited by a rectangular electromagnetic pulse of 30 ns duration having a carrier frequency of $f_{sg} = 7258\,\mathrm{MHz}$ and a power of $P_{sg} = 2\,\mathrm{mW}$. The shape of the output signal was bell-like with 24 ns duration (measured on half-height level) due to the distortions created by the limited frequency band of the delay line and by the spin wave dispersion in the film. The delay time T_D was equal to 300 ns. Using an applied field of 1850 Oe, a carrier frequency of 7258 MHz, and a total value of the uniaxial and the cubic crystallographic anisotropy field of $-85\,\mathrm{Oe}$, a calculation yields the BVMSW group velocity of $v_{gr} = 2.6\,\mathrm{cm}/\mu\mathrm{s}$ at the carrier wave number k_{sg} of approximately $120\,\mathrm{rad}/\mathrm{cm}$. This value corresponds well to the experimental delay time T_D of the non-amplified SW pulse. The wavelength of the carrier spin wave is $2\pi/k_{sg} = 520\,\mu\mathrm{m}$. This value is much larger than the length L of the active area of parametric interaction and satisfies well the non-adiabatic condition $k_{sg}L \leq 1$ [1].

A double-frequency ($f_{pm} = 2f_{sg}$) pumping pulse of duration 30 ns and power $P_{pm} = 8\,\mathrm{W}$ was supplied to the pumping transducer when the input pulse has approached the area of the pumping field localization. The pumping pulse duration of 30 ns was approximately equal to the time that was necessary for the SW packet to move through the area of parametric interaction. The maximum amplification of the output signal was 15 dB. A further increase of the duration of the pumping pulse had no influence on the amplification factor.

The pulse repetition rate of the input and pumping signals was set at 10 kHz to avoid an overheating of the sample by the pumping power.

Since the carrier wave of the pumping pulse was produced by doubling the frequency of the signal carrier wave (see Fig. 1), it was easy to control the phase shift between these waves using a phase shifter situated either in the signal (as demonstrated in Fig. 1) or in the pumping channel of the microwave circuit. The used phase shifter enables us to shift the phase of the signal and the pumping currier waves in the range $(0, 2\pi)$ and $(0, 4\pi)$ respectively.

The first result of applying the pump wave to the YIG film waveguide was the aforementioned amplification of input SW packets of up to 15 dB, which was identified by the increase in intensity of the pulses received by the output antenna. In addition, a strong compression of the amplified wave packet was observed, i.e. the width of the output pulse at half-height level decreased from 24 ns without pumping to 17 ns. Such compression can arise either as a consequence of a nonlinear interaction inside the SW packet or as a result of an amplification of only a part of the SW packet [3]. However, since in our experiment the duration of the pumping pulse was the same as the duration of the input signal, and since the increase in pumping duration did not influence the duration of the amplified signal, the compression could not be directly associated with the process of parametric interaction. Therefore, we interpret this compression as being due to the process of soliton formation started after the amplification of the input wave packet.

The second important result is that the output signal is stable, showing no amplitude pulsation, and the output pulse preserves its bell-shaped appearance in the entire range of amplification gain.

The amplification is easily controlled by the phase shift between the pumping and signal carrier waves using the external phase shifter (Fig. 1). The power of the output signal could be changed from its maximum value corresponding to 15 dB amplification to the minimum value corresponding to almost no gain. The dependence of the power of the amplified signal pulse on the phase shift of the signal carrier waves is shown in Fig. 2. This curve clearly demonstrates the oscillation of the power of the output signal with the period of π. A similar dependence of the output pulse peak power on the phase shift of the *pumping* carrier wave demonstrates the oscillation of the amplification with a period of 2π. The observed behavior of the power of the output signal is caused by the interference of two waves: the parametrically amplified input spin wave and the co-propagating idle wave, created by non-adiabatic pumping of the input wave. The frequency f_i and the propagation direction (or the wave vector k_i) of the created idle wave are defined by the energy and momentum conservation laws. For the one-dimensional case of three-wave (first order) parametric interaction discussed here (the waves propagate along the direction of the bias magnetic field) the conservation laws are formulated as scalar equations

$$f_i = f_{pm} - f_{sg} \tag{1-a}$$

$$k_i = k_{pm} - k_{sg} \tag{1-b}$$

where f_{pm} and k_{pm} are the frequency and wave number of the parametric pumping. Since we are using doubled-frequency ($f_{pm} = 2f_{sg}$) pumping, the frequencies of the signal and the idle waves are equal. In our non-adiabatic case the length L of the pumping localization area is such that $2\pi/L \geq 2k_{sg}$, and thus the wave number spectrum of the pumping contains components with $k_{pm} = 2k_{sg}$. It means that there is an idle wave that co-propagates with the signal wave. Thus we have a situation where two spin waves of equal frequency propagate in one direction and interfere. It is well known from the theory of parametric interaction [6] that the phase of the amplified signal wave coincides with the phase of the input signal ϕ_{sg}. On the other hand, the phase ϕ_i of the idle wave depends also on the phase of the pumping wave, ϕ_{pm}: $\phi_i = \phi_{pm} - \phi_{sg} + \pi/2$. It is evident that a phase shift of the input signal wave by π (or a phase shift of the pumping phase by 2π) will lead to a phase shift between the signal and the idle wave by 2π. As a result the output signal formed by the two interfering waves consecutively changes its peak power from one extremum to another as it is shown in Fig. 2.

It was also found that the peak power of the output pulse oscillates between its minimum and its maximum value both as functions of the bias magnetic field and the frequency of the microwave source. For example, for a constant bias magnetic field $\mathbf{H}_0 = 1850\,\mathrm{Oe}$, the transition between two

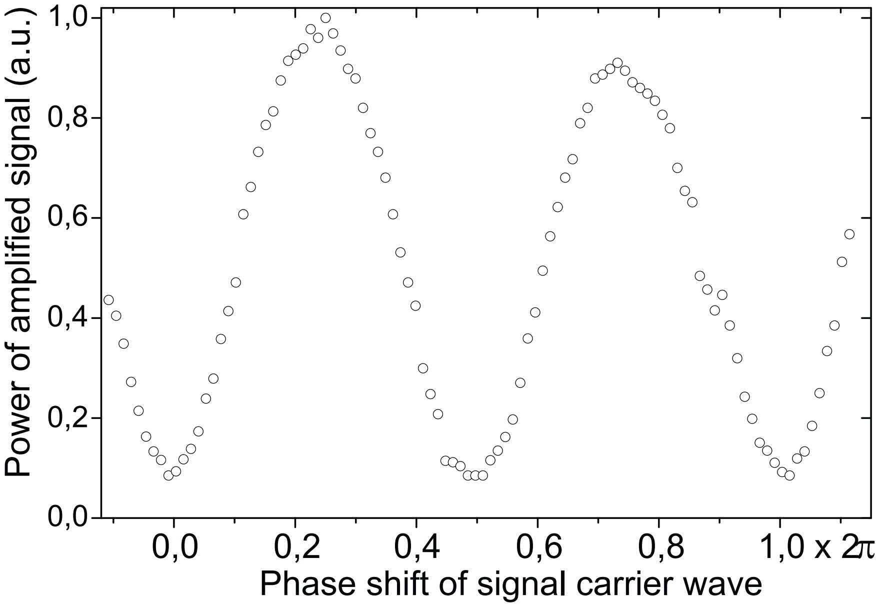

Fig. 2: Dependence of the power of the amplified signal on the phase shift of the signal carrier wave with respect to the pumping carrier wave.

consecutive minima of the peak power of the output pulse was obtained for a frequency change of 3.1 MHz. It is evident that the nature of these effects is the same as the above-analyzed case of controlled phase shift and is based on the change of the phase of the carrier spin wave with respect to the phase of the electromagnetic pumping in the area of parametric interaction. The origin of this phase shift is a time delay of the input signal wave in the YIG film. Since such a delay depends on both the bias magnetic field and the SW signal carrier frequency, the YIG waveguide plays a role of an additional tunable phase shifter situated in the signal channel of the experimental setup. The additional phase shift $\Delta\phi_{sg}$ arising from a signal frequency change of $\Delta f_{sg} = 3.1\,\text{MHz}$ can be calculated as $2\pi f_{sg} l/\nu_{ph}$, where l and ν_{ph} are the distance from the input antenna to the active area and the phase velocity of the spin wave, respectively. For our experimental conditions this phase shift can be estimated as $\Delta\phi_{sg} \simeq 0.9\pi$. This value is in good agreement with the observed period of the oscillation of the output power (Fig. 2).

To summarize, the non-adiabatic regime of parametric amplification of propagating spin wave packets was realized for the case of a controlled phase shift between the carrier spin wave and the electromagnetic pumping field. The strongly (15 dB) amplified and significantly (1.4 times) compressed output signal is stable and exhibits no magnitude pulsation. The amplitude of the amplified signal is controlled in the range of 15 dB (between maximum and minimum values) by changing the phase of either the signal's carrier wave by $\pi/2$ or the pumping wave by π. Thus, the potential for practical applications of a non-adiabatic parametric amplifier for the amplification and compression of propagating microwave radio-pulses has been clearly demonstrated.

This work was partially supported by the Deutsche Forschungsgemeinschaft, by the National Science Foundation, Grant No. DMR-0072017, and by the Oakland University Foundation.

References

[1] G.A. Melkov, A.A. Serga, V.S. Tiberkevich, Yu.V. Kobljanskij, A.N. Slavin, Phys. Rev. E **63**, 066607 (2001).
[2] G.A. Melkov, Yu.V. Kobljanskyj, A.A. Serga, V.S. Tiberkevich, A.N. Slavin, phys. stat. solidi (a) **189**, 1007 (2002).

[3] G.A. Melkov, Yu.V. Kobljanskyj, A.A. Serga, V.S. Tiberkevich, A.N. Slavin, J. Appl. Phys. **89**, 6689 (2001).
[4] A.V. Bagada, G.A. Melkov, A.A. Serga, A.N. Slavin, Phys. Rev. Lett. **79**, 2137 (1997).
[5] P.A. Kolodin, P. Kabos, C.E. Patton, B.A. Kalinikos, N.G. Kovshikov, M.P. Kostylev, Phys. Rev. Lett. **80**, 1976 (1998).
[6] W.H. Louissel, *Coupled Mode and Parametric Electronics* (J. Wiley and Sons, Inc., New York, 1960).

6.5 Formation of envelope solitons from parametrically amplified and conjugated spin wave pulses

A.A. Serga, S.O. Demokritov, and B. Hillebrands[1]

Envelope solitons are stable localized wave packets that preserve their shapes while propagating in nonlinear dispersive media because of a fine balance between competing effects of nonlinearity, dispersion, and diffraction. The amplification of spin wave (SW) envelope solitons by means of microwave parametric pumping has been investigated in [1,2]. It was shown that the interaction of an input SW pulse with a pumping microwave pulse of a relatively large duration, that is applied in a spatially extended region, leads not only to an amplification, but also to a strong compression of the output SW packets when they are detected at a distance of several millimeters from the pumping localization region [3,4]. The observed compression can be caused by different mechanisms.

If SW packets are compressed during the *interaction with pumping*, the compression could be caused by collective oscillations [5,6] in the system of nonlinear spin waves parametrically coupled to the pumping field. On the other hand, if the compression develops *after* the amplification in the course of further propagation of the amplified SW packet, it may be caused by the process of envelope soliton formation.

In traditional microwave spectroscopy [1,2,4] the positions of the input and output antennae (where the output signals are detected) are fixed and, therefore, the SW packet in the course of propagation is not accessible for observation. Thus, it is difficult to determine which compression mechanism is dominant. In this study we use the space- and time-resolved Brillouin light scattering technique to investigate the influence of parametric pumping on the dynamics of linear and nonlinear spin wave packets *in the course of their propagation*. We show that the compression of both forward and reversed (phase conjugated) SW packets, generated as a result of interaction with pumping, is developed in the course of their further propagation. Thus, it must be caused by the four-wave focusing nonlinearity in the medium, that, in competition with dispersion, is responsible for the formation of envelope solitons.

Figure 1 shows a diagram of our experimental setup. It is based on the well-known magnetostatic delay-line structure with a pair (input and output) of short-circuited microstrip antennae (width 50 µm, length 2.5 mm) and a spin wave waveguide cut from an yttrium-iron-garnet (YIG) film. The distance between the antennae was chosen to be 12 mm. The thickness of the YIG film was 5 µm while the width of the SW waveguide was 1.4 mm. A bias magnetic field of $\mathbf{H}_0 = 1827\,\mathrm{Oe}$ was applied along the axis of the YIG waveguide and the SW propagation direction (see Fig. 1). Rectangular microwave pulses of duration 28 ns, carrier frequency 7125 MHz, and varying power $2 \leq P_{in} \leq 44\,\mathrm{mW}$ were supplied to the input antenna. They excited the initial SW packets in the waveguide. The pumping magnetic field (parallel to $\mathbf{H}_0$) was created by a thin disk-shaped dielectric resonator situated approximately in the middle between the microstrip antennae and coupled to the pumping transmission line by a coaxial wire loop. The thickness of the resonator was 0.4 mm, the dielectric permeability was 80, and the loaded quality factor was 150. The waveguide was placed in a thin slot made in the center of the disk, where the intensity of the pumping microwave magnetic field concentrated by the dielectric resonator had its maximum. Due to the small thickness of the resonator the pumping magnetic field was not entirely localized in the slot, but also

---

[1] In collaboration with A.N. Slavin, Department of Physics, Oakland University, Rochester, Michigan, USA.

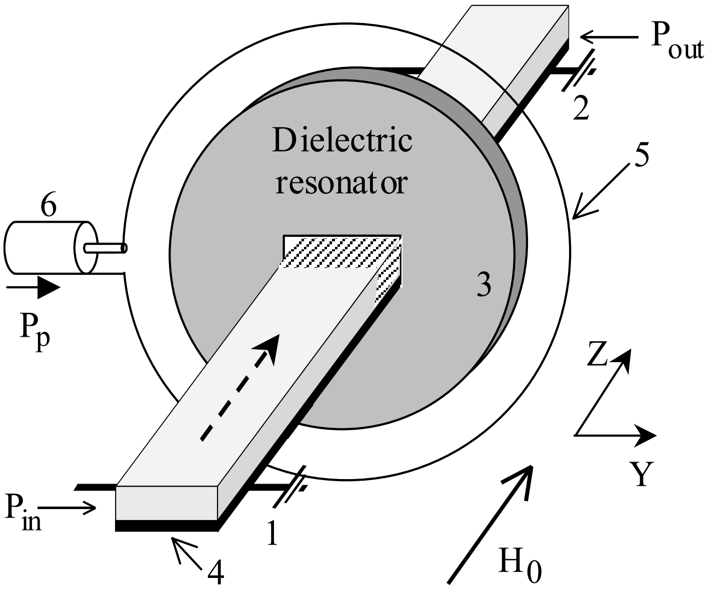

Fig. 1: Experimental setup: (1) and (2) input and output antennae, respectively; (3) open dielectric resonator (ODR); (4) YIG film wave-guide; (5) wire loop for coupling of the open dielectric resonator with pumping transmission line (6). The dashed arrow indicates the direction of propagation of the input spin wave packet. The shaded area near the ODR indicates the effective region of pumping localization.

around it, so the pumping localization region had the effective width of about 1 mm. The geometry of our experiment corresponds to the excitation of backward volume magnetostatic waves (BVMSW) that are a usual object of microwave experiments with bright envelope solitons (see e.g. [1, 2, 4]). According to a theoretical estimation, for the applied field of 1827 Oe and carrier frequency of 7125 MHz the excited BVMSW packet has a carrier wave number of $k_z = 180\,\mathrm{rad/cm}$ and a group velocity of $v_g = -2.5\,\mathrm{cm/ms}$.

When the input SW packet reaches the region of pumping localization it is strongly (gain up to 20 dB) amplified by the pulsed parametric pumping of duration 80 ns, carrier frequency of 14250 MHz, and power 8 W. The maximum amplification has been achieved when the pumping pulse was supplied at the moment when the leading edge of the input spin wave packet reached the left boundary of the pumping localization area. The repetition rate of the input and pumping pulses was set at 50 kHz. The signals received by the antenna 2 in Fig. 1 were used for the determination of the characteristics of the exited spin waves as well as for the initial examination of the behavior of the parametrically amplified delayed pulses.

The detailed investigation of the dynamics of SW packets in the process of their propagation (before and after the interaction with the pulsed pumping field) was made by means of space- and time-resolved inelastic BLS spectroscopy [7]. A two-dimensional distribution of the BLS-intensity $I(y,z,t)$ (which is proportional to the squared amplitude of the local dynamic magnetization in the film $m^2(y,z,t)$) was collected over the YIG film with spatial resolution of 0.1 mm at successive moments of time t separated by the time interval of 1.7 ns. The coordinates $(z_0(t), y_0(t))$ characterizing the instantaneous position of the maximum of the propagating SW packet on the plane (z,y) were calculated as first moments of the distribution $I(y,z,t)$. The sizes of the SW packet along the propagation direction L_z and the transverse direction L_y were calculated as standard deviations of the distribution $I(y,z,t)$. The described statistical approach to the determination of the parameters of propagating SW packets allows us to compare the characteristics of wave packets with substantially different shapes and to diminish the spurious influence of noise on the accuracy of our experimental results.

The chosen values of the input pulse powers allow us to investigate the amplification of either linear ($P_{in} = 2-30\,\mathrm{mW}$) or nonlinear ($P_{in} = 44\,\mathrm{mW}$) input SW packets. The frame (a) in Fig. 2 demonstrates the evolution of the length L_z of a propagating SW packet when pumping is absent.

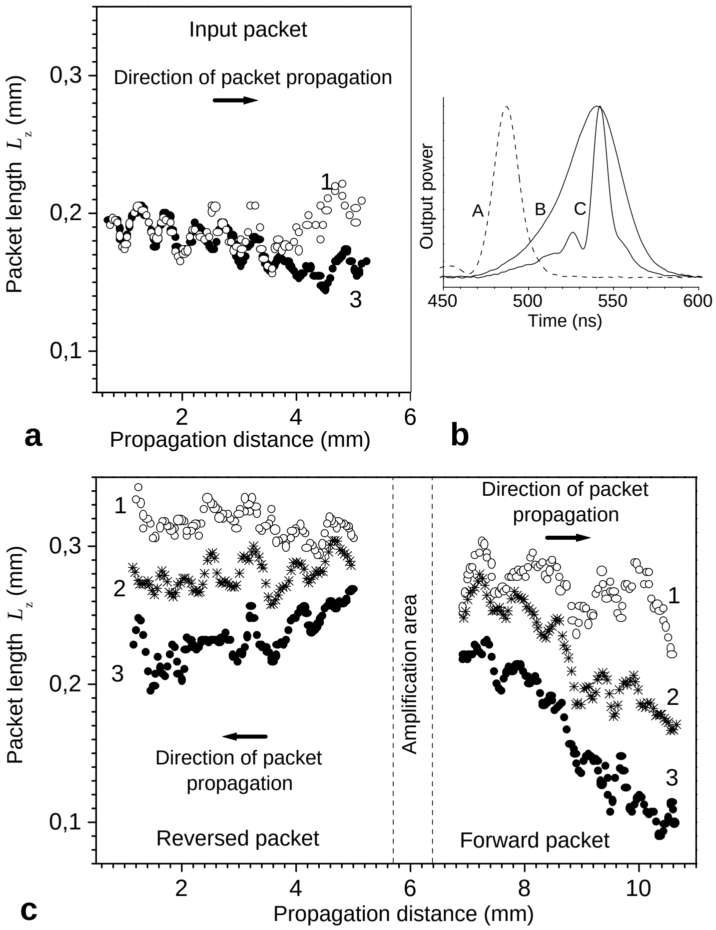

Fig. 2: Evolution of the length L_z of propagating SW packets with the distance from the input antenna. Curves (1), (2), and (3) correspond to the input powers P_{in} of 2 mW, 28 mW, and 44 mW. Frame (a) shows the length of the input SW packet before its interaction with pumping. Frame (c) shows the lengths of forward and reversed SW packets formed as a result of this interaction. Frame (b) shows the normalized profiles of the SW pulses detected at the output antenna: (A) non-amplified signal with initial power $P_{in} = 44$ mW; (B) amplified pulse with $P_{in} = 2$ mW; (C) amplified pulse with $P_{in} = 44$ mW.

One can see that L_z increases slightly for a linear packet ($P_{in} = 2$ mW), while for a nonlinear packet (having $P_{in} = 44$ mW) it slightly decreases due to the initial stages of envelope soliton formation.

The normalized profiles of the SW packets at the output antenna obtained by conventional microwave spectroscopy for the case of no pumping (A) and after interaction with pumping ((B) and (C)) are shown if Fig. 2 (b). Although the group velocities calculated from the BLS data on the SW packet positions before and after the interaction with pumping were found to be practically the same, the data in Fig. 2 (b) shows that the forward packet formed after the interaction with pumping reaches the output antenna 55 ns later than in the case when no pumping is applied. This time shift is caused by the distortion of the packet's shape in the process of parametric amplification [8].

The other important result is a significant compression of the output amplified SW pulse at the large input power $P_{in} = 44$ mW. This is illustrated by the data in Fig. 2 (b). Note, that the narrowing of a *non-amplified* pulse of the same input power is almost negligible (see curve (3) in Fig. 2 (a)).

The microwave pumping field in our experimental set-up is relatively weakly localized in the region of the width of about 1 mm which is almost three times larger than the signal carrier wavelength $2\pi/k_z = 0.35$ mm. In this case the interaction of the input SW pulse with pumping leads not only to the amplification of the initial signal, but also to the formation of a new phase conjugated and reversed SW packet [8, 9]. The frame (c) in Fig. 2 illustrates the evolution of these forward and phase conjugated reversed SW packets. The curves (1) and (2) correspond to linear initial SW packets with input powers of 2 mW and 28 mW, while the curve (3) corresponds to a nonlinear wave packet of $P_{in} = 44$ mW, which almost formed an envelope soliton before reaching the pumping region (see Fig. 2 (a) curve (3)).

It is clear from Fig. 2 (a,c) that the immediate result of parametric interaction of the input SW packet with pumping is a substantial (almost two times) increase in length of both forward and reversed amplified SW packets in comparison with the length of the initial SW packet. This effect, as well as the earlier mentioned shift of the maximum of the output SW packet by 55 ns, is caused by the amplification of the tail of the input SW packet by the relatively long (80 ns) pumping pulse.

It can also be seen from Fig. 2 (c) that in the course of further propagation both forward and reversed SW packets demonstrate a significant compression in length (up to 3.2 times), which is a clear signature of envelope soliton formation. The degree of compression is roughly proportional to the input power P_{in}. Our measurements of the transverse widths L_y of propagating SW packets have shown that the packets' shapes in the transverse direction are stable and, therefore, the influence of diffraction on the observed phenomena is negligible. Thus, we can interpret the observed nonlinear compression of the SW packets in the YIG waveguide as a formation of quasi-one-dimensional SW envelope solitons in both forward and reversed (phase-conjugated) SW packets.

It has been demonstrated that weakly localized and relatively long parametric pumping can transform initially linear SW pulses into envelope solitons and can also successfully amplify envelope solitons formed spontaneously from initially nonlinear input pulses. The formation of SW envelope solitons from a *reversed phase-conjugated* SW pulse resulting from a parametric interaction of the input SW pulse with weakly localized microwave pumping has been experimentally observed for the first time.

This work was supported in part by the Deutsche Forschungsgemeinschaft, by the National Science Foundation, Grant No. DMR-0072017, and by the Oakland University Foundation.

References

[1] A.V. Bagada, G.A. Melkov, A.A. Serga, A.N. Slavin, Phys. Rev. Lett. **79**, 2137 (1997).

[2] P.A. Kolodin, P. Kabos, C.E. Patton, B.A. Kalinikos, N.G. Kovshikov, M.P. Kostylev, Phys. Rev. Lett. **80**, 1976 (1998).

[3] G.A. Melkov, Yu.V. Kobljanskyj, A.A. Serga, V.S. Tiberkevich, A.N. Slavin, phys. stat. solidi (a) **189**, 1007 (2002).

[4] G.A. Melkov, Yu.V. Kobljanskyj, A.A. Serga, V.S. Tiberkevich, A.N. Slavin, J. Appl. Phys. **89**, 6689 (2001).

[5] V.S. L'vov, *Wave Turbulence under Parametric Excitation* (Springer, Berlin, 1994).

[6] V.B. Cherepanov, A.N. Slavin, Phys. Rev. B **47**, 5874 (1993).

[7] O. Büttner, M. Bauer, S.O. Demokritov, B. Hillebrands, Yuri S. Kivshar, V. Grimalsky, Yu. Rapoport, A.N. Slavin, Phys. Rev. B **61**, 11576 (2000)

[8] G.A. Melkov, A.A. Serga, A.N. Slavin, V.S. Tiberkevich, A.N. Olijnyk, A.V. Bagada, Sov. Phys. JETP **89**, 1189 (1999).

[9] G.A. Melkov, A.A. Serga, V.S. Tiberkevich, A.N. Olijnyk, A.N. Slavin, Phys. Rev. Lett. **84**, 3438 (2000).

B. Magnetic Films and Double Layers

6.6 Control of interlayer exchange coupling in Fe/Cr/Fe trilayers by ion beam irradiation

S.O. Demokritov, C. Bayer, S. Poppe, M. Rickart, J. Fassbender, and B. Hillebrands[1]

Since the discovery of the antiferromagnetic interlayer exchange coupling effect in the Fe/Cr/Fe layered system by Grünberg et al. [1] this effect has been widely investigated both theoretically and experimentally (for a recent review see [2]). Antiferromagnetically coupled layers are now used in applications like antiferromagnetically coupled media (AFC-media [3]) and artificial antiferromagnets, (AAF [4]). In many cases such applications greatly gain from a potential of lateral modification of the media parameters with high resolution, after the preparation process of the layered system has been completed. It is not trivial to change the interlayer coupling strength after sample preparation. Until now, to our knowledge, the only reported methods are annealing [5] and charging of the spacer with hydrogen or deuterium [6–8]. However, such techniques can hardly provide any reasonable lateral resolution. On the contrary, beams of light ions with keV energies known for their ability to deeply penetrate into a solid can be focused down to 20 nm [9–11], and should provide a promising pass to accomplish the goal. One of the key advantages of ion irradiation is that magnetic nanopatterning becomes feasible without a change of the sample topography. This is especially important to avoid tribology problems in so-called patterned media [12].

In this contribution, we present first experimental results demonstrating that the strength of the interlayer exchange coupling between two ferromagnets, separated by a non-ferromagnetic spacer, can be modified in a controlled manner by ion beam irradiation. It is also shown, that for some values of the spacer thickness the ion beam bombardment *enhances* the coupling.

Interaction between two magnetic layers separated by a nonmagnetic spacer layer can be phenomenologically described by:

$$E = -J_1 \cos\phi - J_2 \cos^2\phi \quad , \tag{1}$$

where E is the magnetic coupling interface energy, ϕ is the angle between the magnetizations of two magnetic layers and the parameters J_1 and J_2 represent the strength of the bilinear and biquadratic coupling, respectively [13]. If J_2 dominates and is negative, it promotes perpendicular (90°) orientation of the two magnetization vectors. The microscopic origin of the bilinear coupling is a long-range interaction between the magnetic moments via conduction electrons of the spacer. For smooth interfaces J_1 oscillates as a function of the spacer thickness [14, 15]. Essential roughness diminishes the bilinear coupling strength and the amplitude of the oscillations [16, 17]. For perfect layered systems J_2 is thought to be small [18]. The experimentally observed strong biquadratic coupling is believed to be due to extrinsic effects [19, 20].

Light ion irradiation is known to be an excellent tool to modify magnetic parameters of multilayer systems. Chappert et al. [21] have shown that ion irradiation of Co/Pt multilayers leads to a reduction of the perpendicular interface anisotropy. This has been attributed to an interfacial mixing of

---

[1] In collaboration with D.I. Kholin and N.M. Kreines, Institute for Physical Problems, Russian Academy of Science, Moscow, Russia, O.M. Liedke, Institute of Experimental Physics, University of Bialystok, Poland.

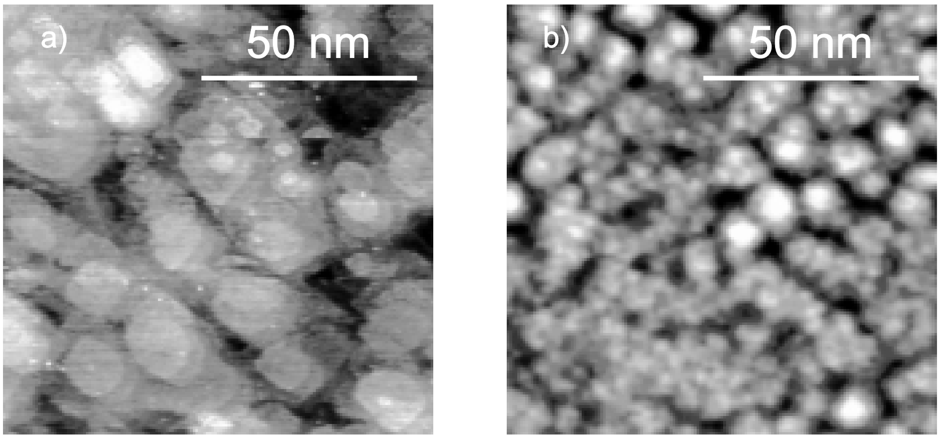

Fig. 1: STM images of the film surfaces: a) bottom Fe film, z-scale 1.3 nm, RMS = 0.11 nm; b) Cr spacer, z-scale 1.5 nm, RMS = 0.18 nm.

both atom species. In FePt alloy systems an increase of the perpendicular magnetic anisotropy due to a short-range chemical ordering has been observed after ion irradiation [22]. The technique has been recently applied to exchange-bias systems, consisting of adjacent ferromagnetic and antiferromagnetic layers. It was shown that the magnitude and direction of the exchange-bias field can be tailored by ion irradiation if a magnetic field is applied during bombardment [23, 24].

Epitaxial Fe/Cr/Fe(001) samples used in the current studies were prepared in an ultra-high vacuum molecular-beam epitaxy system with the base pressure below $5 \cdot 10^{-11}$ mbar. A Cr buffer with a thickness of 100 nm providing a lattice matched template for the subsequent growth of the Fe/Cr/Fe [26] system was deposited on a MgO(001) substrate. Two Fe films separated by an wedge-shape, 0.4 to 4 nm thick Cr spacer were deposited on the buffer. Different samples with the thickness of the Fe films from 5 to 10 nm have been prepared. Finally the system was covered by a 3 nm thick Cr layer to avoid corrosion for *ex-situ* measurements. The details of substrate preparation and the growth procedure are published elsewhere [25]. Figure 1 displays the topography of the lower Fe film and of the Cr spacer as observed by STM. Atomic terraces and monoatomic steps are clearly seen in the images.

Using the measured RMS values of the surface roughness (0.11 and 0.18 nm for the Fe and the Cr surface, respectively) and assuming uncorrelated thickness fluctuations for the two films, one obtains an RMS value for the thickness fluctuations of the Cr spacer of 0.14 nm, which is close to the thickness of one monolayer (ML). Based on this value and assuming a Gaussian distribution of the probability for the spacer to consist of a given number of monolayers, one obtains, for example, for a nominal thickness of the Cr spacer, d_{Cr} of 4 ML that: 31.4% of the film area is thicker than $d_{Cr} = 4$ ML, 38% has $d_{Cr} = 4$ ML, 24% has $d_{Cr} = 3$ ML, 6% 2 ML, 0.6% 1 ML, and 0.025% corresponds to direct contact between the two Fe films (so-called “magnetic bridges”). The latter provide a strong ferromagnetic coupling between the Fe films.

Irradiation was performed with 5 keV He^+ ions without applied magnetic field with the sample being kept at room temperature. TRIM simulations [27] show that for the used parameter set most ions pass both magnetic layers and are stopped in the Cr buffer layer. The maximum fluence used was $8 \cdot 10^{14}$ ions/cm^2. The interlayer coupling was derived from the magnetization curves recorded by longitudinal magneto-optical Kerr-effect (MOKE) magnetometry. A magnetic field of up to 6 kOe was applied in the plane of the sample parallel either to the easy or to the hard magnetic axes of the four-fold magnetic anisotropy of the Fe(001) films.

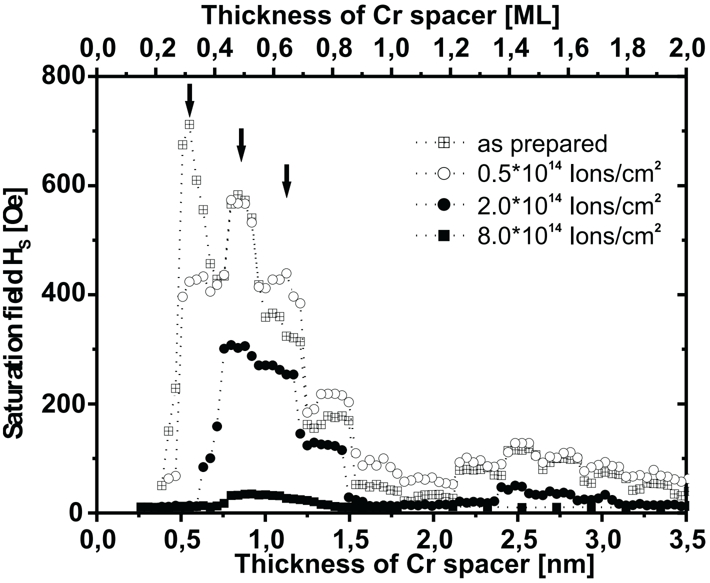

Fig. 2: Saturation field H_S as a function of the Cr spacer thickness for the 10 nm Fe/d_{Cr} Cr/10 nm Fe trilayer system as prepared and after the irradiation with the fluences as indicated. The arrows indicate the first three maxima of the interlayer coupling.

The magnetization curves measured for the field applied along the easy [100]-axis show several jumps, characteristic for magnetic double layers with antiferromagnetic and 90°-coupling [13]. The saturation field, H_S, which is proportional to $|J_1 + 2J_2|$ extracted from the magnetization curves is shown in Fig. 2 as a function of the nominal Cr-spacer thickness for different ion irradiation fluences. The data obtained on the as-prepared sample clearly demonstrates both long- and short-period oscillations with a moderate amplitude in agreement with the RMS value of the spacer thickness fluctuation obtained from the STM studies. The arrows indicate the first three oscillation maxima of the coupling strength. As it is seen in Fig. 2, such a well prepared layered magnetic system is very sensitive to ion irradiation. The first oscillation maximum (d_{Cr} = 0.58 nm = 4 ML) exhibits the strongest effect of the irradiation on the coupling strength. Even the lowest used ion fluence of $0.5 \cdot 10^{14}$ ions/cm^2 reduced H_S by more than 30 %. For the fluences above $2 \cdot 10^{14}$ ions/cm^2 no antiferromagnetic coupling is observed for this thickness of the Cr-spacer. The change of the measured coupling strength for thicker Cr-spacers is more intriguing: the coupling *increases* for small ion fluences and then decreases for fluences above $1 \cdot 10^{14}$ ions/cm^2 [28].

An additional study made by means of Brillouin light scattering on spin waves has indicated no change in the four-fold in-plane and out-of-plane anisotropy constants after the bombardment for the studied fluence range.

Of particular interest are the dependencies of the coupling constants J_1 and J_2 as functions of ion fluence and spacer thickness. From the measured remagnetization curves the fluence dependence of those constants for the spacer thicknesses corresponding to the first (4 ML), second (6 ML), and third (8 ML) oscillation maximum have been evaluated. Note that only the values of the antiferromagnetic ($J_1 < 0$) and 90° ($J_2 < 0$) coupling constants can be usually derived in such a way. The data is presented in Fig. 3. It is clearly seen from the figure, that $|J_1|$ strongly decreases with the fluence for d_{Cr} = 4 ML, while it shows a maximum for fluences near $0.5 \cdot 10^{14}$ ions/cm^2 for d_{Cr} equal to 6 and 8 ML. $|J_2|$ instead shows a monotonic decrease. Thus, one can conclude from Fig. 3 that the increase of the saturation field at small irradiation fluences is caused by the increase of $|J_1|$.

The origin of the observed phenomena is not understood in all details yet, but they are definitely connected with the surface intermixing caused by the He ions. To understand this qualitatively let us first consider the fluence dependence of $|J_1|$ for the nominal thickness d_{Cr} = 4 ML. Direct

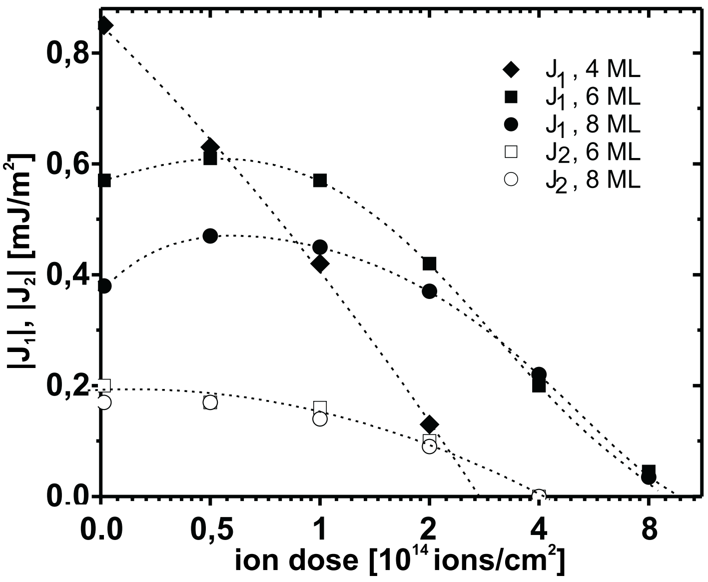

Fig. 3: $|J_1|$ and $|J_2|$ obtained from the remagnetization curves for different maxima versus the fluence. The lines are guides to the eye.

magnetic bridges between the two Fe films provide strong direct ferromagnetic coupling, $J_{direct} \approx 2A/d_{ML}$= 280 mJ/m^2, where $A = 2 \cdot 10^{-11}$ J/m is the bulk exchange constant of Fe and d_{ML} = 0.144 nm is the thickness of one monolayer. The contribution to the measured interlayer coupling due to the magnetic bridges can be then easily estimated, since the percentage area of those bridges is known from the RMS analysis of the STM images discussed above. For the as-prepared sample the obtained value of 0.07 mJ/m^2 is essentially smaller than the measured one and indicates that the interlayer coupling via the spacer is an order of magnitude larger than direct coupling across the bridges.

It is known that an ion propagating within a lattice partly dissipates its energy due to nuclear collisions [27]. Such collisions cause recoil of atoms of the lattice and creation of lattice defects and intermixing. Although light ions, like helium, have a low displacement rate and cause a short range intermixing, these processes are of importance if taking place at the interface. Estimations show that a 5 keV He ion initiates in average between one and two atom pair exchange events per monolayer in Fe and Cr [29]. In the areas with d_{Cr} = 1 ML such an exchange event induces an atomic size magnetic bridge. Assuming that each ion generates one exchange event per monolayer as a lower bond and taking into account also a possibility of two successive exchange events at adjacent lattice sites, one obtains that for the fluence of $2 \cdot 10^{14}$ ions/cm^2 the relative area of the magnetic bridges increases to 0.2% and their contribution to the interlayer coupling is 0.6 mJ/m^2. This is in rather good agreement with the experimentally observed coupling reduction of 0.72 mJ/m^2. The calculation also demonstrates that the probability for formation of magnetic bridges due to the bombardment decreases exponentially with the nominal spacer thickness at a given interface roughness. Thus, it is not surprising that the effect of the irradiation is weaker for larger spacer thicknesses (the second and third maximum).

Surprising is, however, the observation of an *increase* of the antiferromagnetic coupling strength. This finding might be related to the fact, that, first, an intermixing at the Fe/Cr(001) interface with a width of 1-2 monolayers is supposed to be energetically favorable [30–32], but it is usually not completely achieved during the film growth because of kinetic growth effects. Second, He ions in the discussed energy range very effectively transfer energy to phonons (8 – 12 eV per monolayer), which in turn help the system to relax into this optimum.

It is known that the interlayer coupling in the Fe/Cr/Fe(001) layered system can be increased by a gentle annealing [5]. Stronger coupling in this case is usually connected with higher lateral homogeneity of interface intermixing between Fe and Cr. On the other hand, a close relation between a homogeneous intermixing at the interface and the interlayer coupling has been recently nicely demonstrated for Fe/Si/Fe [33]: the introduction of two monolayers of $Fe_{0.5}Si_{0.5}$ at every Fe/Si interface brought about a much stronger coupling, as observed on the samples where the intermixing took place naturally.

Using all the above presented facts, the observed increase of the interlayer coupling can be qualitatively understood as the effect of ”phonon annealing”: An ion propagating in the lattice creates pulses of hyperthermic phonons along its trajectory. The emitted phonons increase the probability that those parts of the interfaces, where the energetically favorable mixing has not been reached during the growth, move towards this equilibrium. Note here, that since this process at its end can produce additional energy, the phonons do not spend their energy and act just as a catalyst. In a similar way as it is observed in the Fe/Si/Fe system [33], a higher degree of the interface homogeneity causes higher interlayer coupling.

Support by the Deutsche Forschungsgemeinschaft is gratefully acknowledged. C.B. acknowledges support by the Studienstiftung des Deutschen Volkes. The authors are also indebted to H. Urbassek for his fruitful comments on the ion intermixing power.

References

[1] P. Grünberg, R. Schreiber, Y. Pang, M.B. Brodsky H. Sowers, Phys. Rev. Lett. **57**, 2442 (1986).
[2] D.E. Bürgler, S.O. Demokritov, P. Grünberg, M.T. Johnson, Handbook of Magnetic Materials, vol 13, Ed. K.J.H. Buschow, Elsevier, Amsterdam, 2001.
[3] E. Fullerton, D.T. Margulies, M.E. Schabes, M. Carey, B. Gurney, A. Moser, M. Best, G. Zelter, K. Rubin, H. Rosen, M. Doerner, Appl. Phys. Lett. **77**, 3806 (2000).
[4] J. Schmalhorst, H. Brückl, G. Reiss, R. Kinder, G. Gieres, J. Wecker, Appl. Phys. Lett. **77**, 3456 (2000).
[5] Q. Leng, V. Cross, R. Schäfer, A. Fuss, P. Grünberg, W. Zinn, J. Magn. Magn. Mater. **126**, 367 (1993).
[6] F. Klose, Ch. Rehm, D. Nagengast, H. Maletta A. Weidinger, Phys. Rev. Lett. **78**, 1150 (1997).
[7] B. Hjövarsson, J.A. Dura, P. Isberg, T. Watanabe, T.J. Udovic, G. Andersson, C.F. Majkrzak, Phys. Rev. Lett. **79**, 901 (1997).
[8] V. Leiner, M. Au, T. Schmitte, H. Zabel, Appl. Phys. A, in print (2002).
[9] T. Aign, P. Meyer, S. Lemerle, J.P. Jamet, J. Ferré, V. Mathet, C. Chappert, J. Gierak, C. Vieu, F. Rousseaux, H. Launois, H. Bernas, Phys. Rev. Lett. **81**, 5656 (1998).
[10] P. Warin, R. Hyndman, J.N. Chapman, J. Ferré, J.P. Jamet, V. Mathet , C. Chappert, J. Appl. Phys. **90**, 3850 (2001).
[11] J. Lohau, A. Moser, C.T. Rettner, M.E. Best, B.D. Terris, Appl. Phys. Lett. **78**, 990 (2001).
[12] R.M.H. New, R.F.W. Pease, R.L. White, J. Vac. Sci. Technol. B **12**, 3196 (1994).
[13] M. Rührig, R. Schäfer, A. Hubert, R. Mosler, J.A. Wolf, S. Demokritov, P. Grünberg, Phys. Stat. Sol. (a) **125**, 635 (1991).
[14] S.S.P. Parkin, N. More, K.P. Roche, Phys. Rev. Lett. **64**, 2304 (1990).
[15] S.S.P. Parkin, Phys. Rev. Lett. **67**, 3598 (1991).
[16] J. Unguris, R.J. Celotta, D.T. Pierce, Phys. Rev. Lett. **79** 2734 (1997).
[17] Y. Wang, P.M. Levy, J.L. Fry, Phys. Rev. Lett. **65**, 2732 (1990).
[18] R.P. Erikson, K.B. Hathaway, J.R. Cullen, Phys. Rev. B **47**, 2626 (1993).
[19] J.C. Slonczewski, Phys. Rev. Lett. **67**,3172 (1991); J.C. Slonczewski, J. Magn. Magn. Mater. **150**, 13 (1995).
[20] S. Demokritov, E. Tsymbal, P. Grünberg, W. Zinn, I.K. Schuller, Phys. Rev. B **49**, 720 (1994).
[21] C. Chappert, H. Bernas, J. Ferré, V. Kottler, J.-P. Jamet, Y. Chen, E. Cambril, T. Devolder, F. Rousseaux, V. Mathet, H. Launois, Science **280**, 1919 (1998).
[22] D. Ravelosona, C. Chappert, V. Mathet, H. Bernas, Appl. Phys. Lett. **76**, 236 (2000).
[23] T. Mewes, R. Lopusnik, J. Fassbender, B. Hillebrands, M. Jung, D. Engel, A. Ehresmann, H. Schmoranzer Appl. Phys. Lett. **76**, 1057 (2000).

[24] A. Mougin, T. Mewes, M. Jung, D. Engel, A. Ehresmann, H. Schmoranzer, J. Fassbender, B. Hillebrands, Phys. Rev. B **63**, 060409(R) (2001).

[25] M. Rickart, B.F.P. Roos, T. Mewes, J. Jorzick, S.O. Demokritov, B. Hillebrands, Surf. Sci. **495**, 68 (2001).

[26] E.E. Fullerton, M.J. Conover, J.E. Mattson, C.H. Sowers, S.D. Bader, Appl. Phys. Lett. **63**, 1699 (1993).

[27] J. Ziegler, J. Biersack, U. Littmark, The Stopping of Ions in Matter, Pergamon, New York, 1985.

[28] Although the effect of ion bombardment on the coupling is observed on all investigated samples, its absolute value varies from sample to sample. This is due to slight variations of the RMS roughness constant of the prepared films. Therefore, for a quantitative description of the bombardment effect on a given sample, the STM data of this particular sample must be used.

[29] H. Urbassek, private communication.

[30] B. Heinrich, J.F. Cochran, T. Monchesky, R. Urban, Phys. Rev. B **59**, 14520 (1999).

[31] Ch. Sauer, F. Klinkhammer, E. Yu. Tsymbal, S. Handschuh, Q. Leng W. Zinn, J. Magn. Magn. Mater. **161**, 49 (1996).

[32] M. Freyss, D. Stoeffler, H. Dreyssé, Phys. Rev. B **56**, 6047 (1997).

[33] R.R. Gareev, D.E. Bürgler, M. Buchmeier, R. Schreiber, P. Grünberg, submitted to Appl. Phys. Lett.

6.7 Temperature dependence of the interlayer coupling in a Fe/Cr/Fe wedge sample: Static and dynamic studies

S.O. Demokritov, D.I. Kholin, H. Nembach, and M. Rickart[1]

The magnetic coupling of two iron layers across a thin chromium spacer has been extensively studied during the last several years and still attracts a lot of attention. The interlayer exchange is known to change between ferromagnetic and antiferromagnetic, depending on the spacer thickness [1]. Two oscillation periods of the coupling were observed in Fe/Cr/Fe systems: a short one (about 3 Å) and a long one (about 18 Å) [2, 3]. There are also numerous experimental evidences that a non-collinear magnetic ordering of neighboring ferromagnetic layers can take place in such systems [4, 5]. The interaction energy in the usual Heisenberg form $J_1\left(\mathbf{M}_1\mathbf{M}_2\right)$ (bilinear with respect to the iron magnetization vectors) is not sufficient to describe this effect. The so-called biquadratic coupling term $J_2\left(\mathbf{M}_1\mathbf{M}_2\right)^2$ is usually introduced to explain the non-collinear magnetic ordering, the unusual magnetization process, and the magnetic resonance and spin-wave spectra in Fe/Cr multilayer samples (see ref. [4] and review article [5]). Some authors use other forms of interlayer coupling to interpret their experimental data [6]. In spite of many theoretical works devoted to this problem the origin of the coupling and its relation to the antiferromagnetic ordering

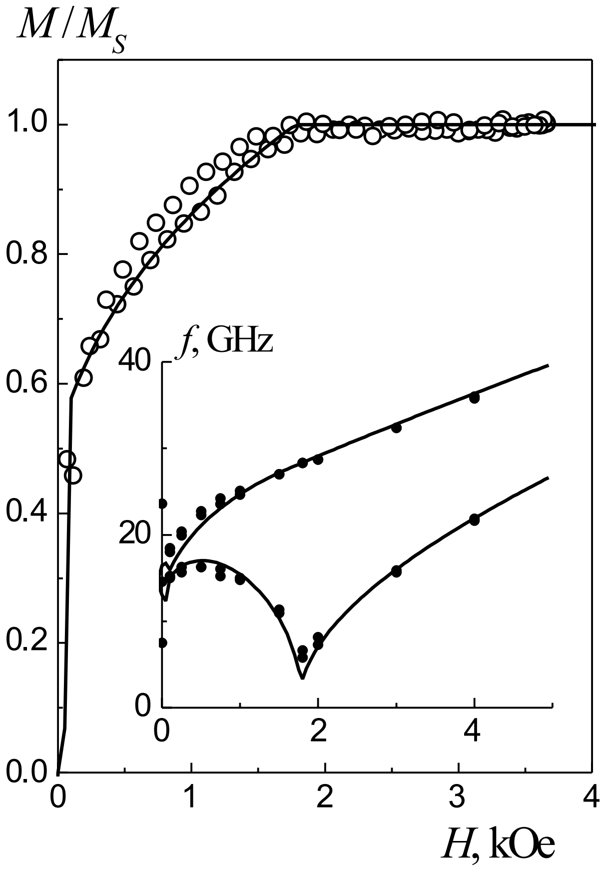

Fig. 1: Magnetization curve and BLS spectrum of a Fe/Cr/Fe sample at $t_{\mathrm{Cr}} = 8.3$Å. Circles: experimental data, solid lines: results of numerical calculations, performed on the basis of the biquadratic coupling model.

---

[1] In collaboration with A.B. Drovosekov and N.M. Kreines, Kapitza Institute for Physical Problems, Russian Academy of Science, Moscow, Russia.

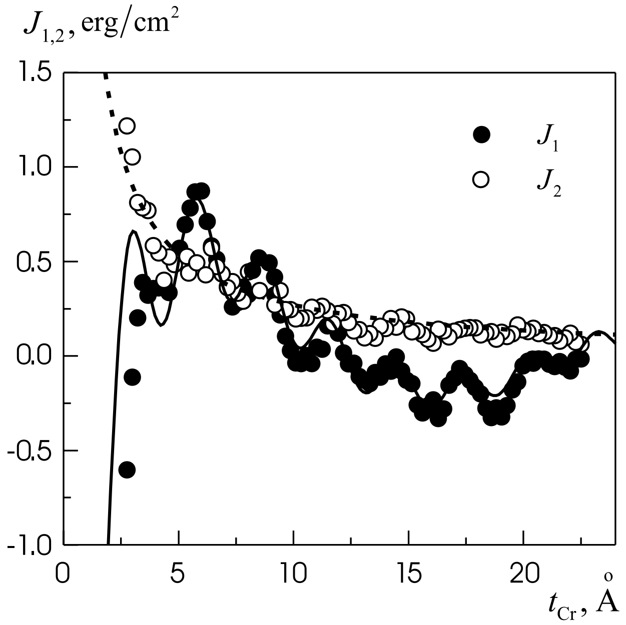

Fig. 2: Dependence of two coupling constants on the chromium spacer thickness at room temperature. Circles: experimental data, solid and dashed lines: results of approximation (see in text for details).

of the chromium spacer is not clear. Detailed measurements of interlayer coupling as a function of spacer thickness and temperature could provide a way to differentiate between different exchange mechanisms proposed by the theory. We have performed such measurements in the 0 – 21 Å spacer thickness interval at temperatures from 77 K up to 473 K. The static properties and spin-wave spectrum of the system proved to be in a good agreement with the biquadratic coupling model predictions. We obtained comprehensive information about both the bilinear and the biquadratic exchange behavior and could analyze the coupling effect much more reliably.

The Fe(100 Å)/Cr(0 – 22 Å)/Fe(100 Å) wedge-type structure was deposited at 200°C onto a MgO substrate with a 1000 Å Ag buffer layer. The *in-situ* LEED measurements have shown a well-defined monocrystalline structure of the sample with smooth interlayer interfaces. A 20 Å chromium cover layer was used to protect the sample from oxidation.

We used two different methods to study the interlayer coupling in our sample: static MOKE magnetometry at temperatures from 77 K to 473 K and dynamic Brillouin light scattering (BLS) to measure the frequency of the Damon–Eshbach spin wave modes [7] at room temperature. The static magnetization curve and the field dependence of the spin wave frequencies at $q = 1.57 \cdot 10^5\,\mathrm{cm}^{-1}$ for $t_{\mathrm{Cr}} = 8.3$ Å at room temperature are shown in Fig. 1. The solid lines represent the calculated magnetization curve and spectrum, obtained in the frame of the biquadratic coupling model. The following energy expression was used to describe the magnetic properties:

$$\begin{aligned} E = -d \cdot \mathbf{H}(\mathbf{M}_1 + \mathbf{M}_2) - \frac{J_1}{M_S^2} \cdot (\mathbf{M}_1\,\mathbf{M}_2) - \frac{J_2}{M_S^4}(\mathbf{M}_1\,\mathbf{M}_2)^2 \\ + d\,\frac{K_{eff}}{2}\left[(\mathbf{M}_1 \cdot \mathbf{z})^2 + (\mathbf{M}_2 \cdot \mathbf{z})^2\right] \\ -d\,\frac{H_a}{4M_S^3}\left[(\mathbf{M}_1 \cdot \mathbf{x})^4 + (\mathbf{M}_1 \cdot \mathbf{y})^4 + (\mathbf{M}_1 \cdot \mathbf{z})^4 + (\mathbf{M}_2 \cdot \mathbf{x})^4 + (\mathbf{M}_2 \cdot \mathbf{y})^4 + (\mathbf{M}_2 \cdot \mathbf{z})^4\right] \quad , \end{aligned} \tag{1}$$

where J_1 and J_2 are the bilinear and biquadratic coupling constants, $\mathbf{M}_1$ and $\mathbf{M}_2$ are the magnetization vectors of the iron layers, d is the thickness of each iron layer, K_{eff} is the effective surface anisotropy coefficient, which includes the demagnetization field and the surface anisotropy, H_a is

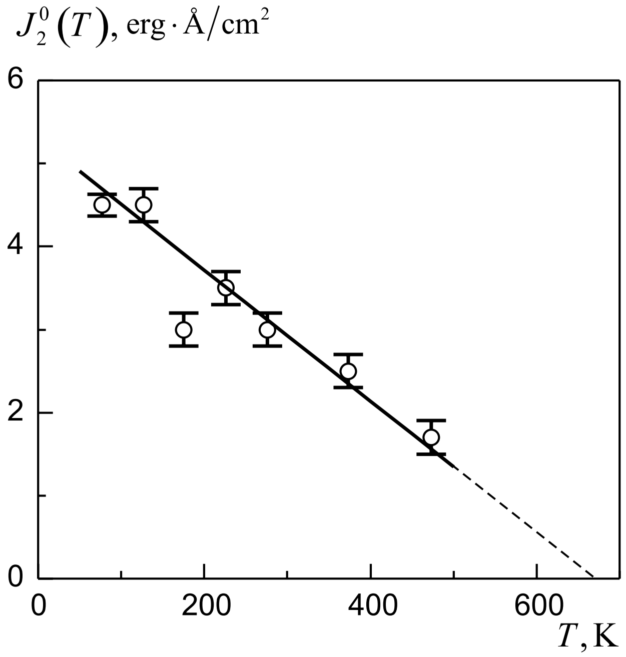

Fig. 3: The biquadratic coupling approximation parameter J_2^0 as a function of temperature. Circles: experimental data, solid line: linear approximation of experimental points.

the effective fourfold anisotropy field with easy axes $\hat{x}$, $\hat{y}$ and $\hat{z}$, where the $\hat{z}$-axis is perpendicular to the sample plane. The detailed description of these calculations can be found elsewhere [8]. Figure 1 shows that both the magnetization curve and the spin wave frequencies can be simultaneously fitted using one set of coupling parameters. So we affirm that the biquadratic coupling model works well in our case.

The thickness dependencies of the constants J_1 and J_2 extracted from the MOKE measurements at room temperature are shown in Fig. 2. It is important to mention, that these data are in a good agreement with the BLS results. J_1 shows well-defined short-wavelength oscillations. The solid line represents the approximation of this data by an RKKY-like formula with two oscillation periods: 2.8 Å and 17 Å.

The J_2 value monotonically decays with chromium thickness and can be best approximated by a J_2^0/t_{Cr} dependence, shown in the plot by a dashed line. It should be mentioned that this behavior seems to be in contradiction with existing theoretical models and needs an extra consideration, which we are going to publish elsewhere [8].

Within the given accuracy the $J_1(t_{\mathrm{Cr}})$ dependence exhibits no changes with temperature. On the contrary, $J_2(t_{\mathrm{Cr}})$ is quite sensitive to temperature changes. As at all investigated temperatures $J_2(t_{Cr})$ obeys the J_2^0/t_{Cr} law, we plot the value J_2^0 as a function of temperature in Fig. 3. J_2^0 decreases with temperature and tends to vanish at about 700 K, as demonstrated by a straight line in the plot. This temperature is close to the paramagnetic to commensurate spin density wave phase transition which is known to take place in thin chromium layers near the iron–chromium interface [9]. This is one more corroboration of the idea that the biquadratic coupling in Fe/Cr/Fe systems is directly connected to the antiferromagnetic order in the chromium spacer, which is known to exist in Fe/Cr/Fe multilayers at much higher temperatures than in bulk samples.

References

[1] P. Grünberg, R. Schreiber, Y. Pang, M.B. Brodsky and H. Sowers, Phys. Rev. Lett. **57**, 2442 (1986).
[2] S.S.P. Parkin, N. More, K.P. Roche, Phys. Rev. Lett. **64**, 2304 (1990).

[3] J. Unguris, R.J. Celotta, D.T. Pierce, Phys. Rev. Lett. **67**, 140 (1991).
[4] M. Rührig, R. Schäfer, A. Hubert, R. Mosler, J.A. Wolf, S.O. Demokritov, P. Grünberg, Phys. Stat. Sol. A **125**, 635 (1991).
[5] D.T. Pierce, J. Unguris, R.J. Celotta, M.D. Stiles, J. Magn. Magn. Mater. **200**, 290 (1999).
[6] A. Schreyer, J.F. Anker, Th. Zeidler et al., Phys. Rev. B **52**, 16066 (1995).
[7] R.W. Damon, J.R. Eshbach, J. Phys. Chem. Solids **19**, 308 (1961).
[8] S.O. Demokritov, A.B. Drovosekov, D.I. Kholin, N.M. Kreines et al., JETP, in press.
[9] H. Zabel. J. Phys.: Condens. Matter **11**, 9303 (1999).

6.8 Correlation of morphology and magnetic anisotropies of epitaxial Fe(001) films on vicinal Au(001) surfaces with different step orientation

M. Rickart, T. Mewes, S.O. Demokritov, and B. Hillebrands

Much research in the recent years was undertaken on growing artificially structured magnetic materials. Vicinal surfaces with their periodic steps provide an excellent model system to investigate the correlation of the surface morphology and the magnetic properties of 2D ferromagnetic thin films. In this connection magnetic anisotropies have to be considered in the design of new magnetic materials. The missing bonds of atoms at the surface (Néel's mechanism [1]) and strain within the film [2] are believed to originate the step induced uniaxial anisotropy. A study of the dependence of the effective anisotropy strength on the film thickness d helps to determine the surface contribution to the anisotropy, since the $1/d$ dependence of the anisotropy strength is an characteristic feature of surface anisotropies [1].

In this contribution a study of the structure and morphology of vicinal Au(001) and Fe(001) surfaces with step edges perpendicular to the [100] as well as to the [110] direction is reported. A strong correlation of the surface morphology of the films with the magnetic properties is found. The dependence of the step induced uniaxial in-plane anisotropy on the step density for the Fe/Au(001) system with step edges perpendicular to the [100] as well as to the [110] direction originates directly from the surface morphology, the latter determined by STM. We show that for one direction of the step edges the interface contribution of the uniaxial in-plane anisotropy changes its sign with increasing vicinal angle.

MgO(001) substrates with a vicinal miscut angle between 0.5° and 7° were prepared in a multichamber molecular-beam epitaxy system. The deposition rates ranged between 0.01 and $0.1\,\mathrm{nm/s}$ as monitored by a quartz microbalance. The analysis of the surface morphology and the sample structure was performed *in-situ* with low energy electron diffraction (LEED). To image the surface topography in real space in UHV, scanning tunneling microscopy (STM) was carried out with a commercial Park Scientific Instruments Autoprobe VP 2 UHV device. All topographic images were obtained at room temperature in a constant-current mode with a tunneling current of $0.3\,\mathrm{nA}$ using electrochemically etched W tips. The tip bias was 0.1 or 1 V in the case of Fe and 0.1 V for Au.

From the STM data the height-height correlation function $H(\mathbf{r}) = \langle [z(\mathbf{r}) - z(0)]^2 \rangle$ has been calculated using a procedure described in Ref. [3]. $z(\mathbf{r})$ is the surface height at position $\mathbf{r}$ of the surface. For a self-affine and isotropic surface $H(\mathbf{r})$ can be expressed as [4]

$$H(r) = 2w^2 \left[1 - \exp\left(- \left(\frac{r}{\xi} \right)^{2\alpha} \right) \right] \quad , \tag{1}$$

where α is the roughness exponent describing the texture of roughness, ξ is the lateral correlation length defining a typical lateral size of the roughness pattern, and w is the interface width (saturation value of the root-mean-square (RMS) roughness). A corresponding fit of these parameters to our experimental data is shown in Fig. 1. Since stepped surfaces were investigated in this study, two predominant orientations have to be considered: one parallel to the step edges and one perpendicular to them. Therefore two different lateral correlation lengths are introduced: $\xi_\perp$ ($\xi_\|$) for the correlation length perpendicular (parallel) to the miscut direction.

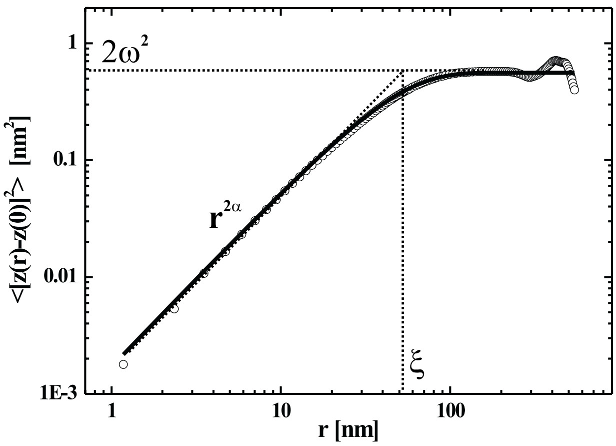

Fig. 1: Height-height correlation curve for the STM image of a Au film with 2° miscut along $[110]_{\mathrm{Au}}$ direction as presented in Fig.2 (f). The correlation was calculated perpendicular to the miscut direction. The straight line is a fit to the data (open circles).

Epitaxially grown Au buffers on vicinal to MgO(001) surfaces were used as the base for the preparation of ultrathin *bcc* Fe films as published in [5, 6]. To clarify the notation of the directions and to prevent from irritations, we indicate the direction *perpendicular* to the steps with the respective material as subscript. The step edges of the Au(001) surface perpendicular to the $[100]_{\mathrm{Au}}$ direction correspond to step edges perpendicular to the $[110]_{\mathrm{Fe}}$ of the Fe film (see below). The typical 5×20 reconstruction [7, 8] of the Au(001) surface is observed by LEED as shown in the insets in Fig. 2. For step edges perpendicular to the $[110]_{\mathrm{Au}}$ direction the reconstruction is oriented along one predominant direction on a vicinal sample. The corresponding STM images of different vicinal Au(001) surfaces corroborate this fact. The 5×20 reconstruction in atomic resolution is displayed in Fig. 2 (a) with a grey scale setting of 0.2 nm. The following larger image scans are shown to illustrate the change in the morphology with increasing vicinal miscut angle for different directions of the step edges. First, Fig. 2 (b) represents a (001) surface without miscut. The atomic rows of the reconstructed surface are orientated parallel the $[110]_{\mathrm{Au}}$ directions. The existence of domains with different orientation ($[110]_{\mathrm{Au}}$ or $[1\bar{1}0]_{\mathrm{Au}}$) of the reconstruction restores a fourfold symmetry of the surface, as confirmed by the LEED patterns, shown in the inset of Fig. 2 (b). For a scan area of 0.2 µm × 0.2 µm the RMS roughness of the surface is 0.33 nm. The images from Fig. 2 (c-h) represent Au surfaces with a miscut along the $[110]_{\mathrm{Au}}$ direction. For the samples with miscut smaller than 1.5°, elongated rectangular terraces with their longer step edge parallel to the miscut direction are observed. The parallel alignment of the reconstruction rows and the longer edge of the terraces seems to be energetically more favorable. For higher vicinal angles ($1.5^\circ - 7^\circ$) a transition in the morphology takes place. The step edges are found to be perpendicular to the nominal miscut direction demonstrating regular monatomic steps. The 5×20 reconstruction prefers the orientation along the step edges. Therefore the direction of arrays of the reconstruction rows coincides in most cases with that of the monatomic steps. For a miscut along the $[100]_{\mathrm{Au}}$ direction the steps have a zig-zag like shape as shown in Fig. 2 (i-k). With increasing vicinal angle the size of the triangular shaped terraces is decreasing. The step edges are oriented along the $[110]_{\mathrm{Au}}$ and $[1\bar{1}0]_{\mathrm{Au}}$ direction, whereas the miscut direction is along the $[100]_{\mathrm{Au}}$ direction.

For the STM data the height-height correlation function of the surface morphology was determined. The correlation length parallel to the miscut direction ($\xi_{\|}$) and perpendicular ($\xi_{\perp}$) to the nominal miscut direction were evaluated. We determine parameters describing the in-plane anisotropy in the correlation length and the roughness exponent:

$$\Xi = \frac{\xi_{\|} - \xi_{\perp}}{\xi_{\perp} + \xi_{\|}} \text{ and } A = \frac{\alpha_{\perp} - \alpha_{\|}}{\alpha_{\perp} + \alpha_{\|}} \quad . \tag{2}$$

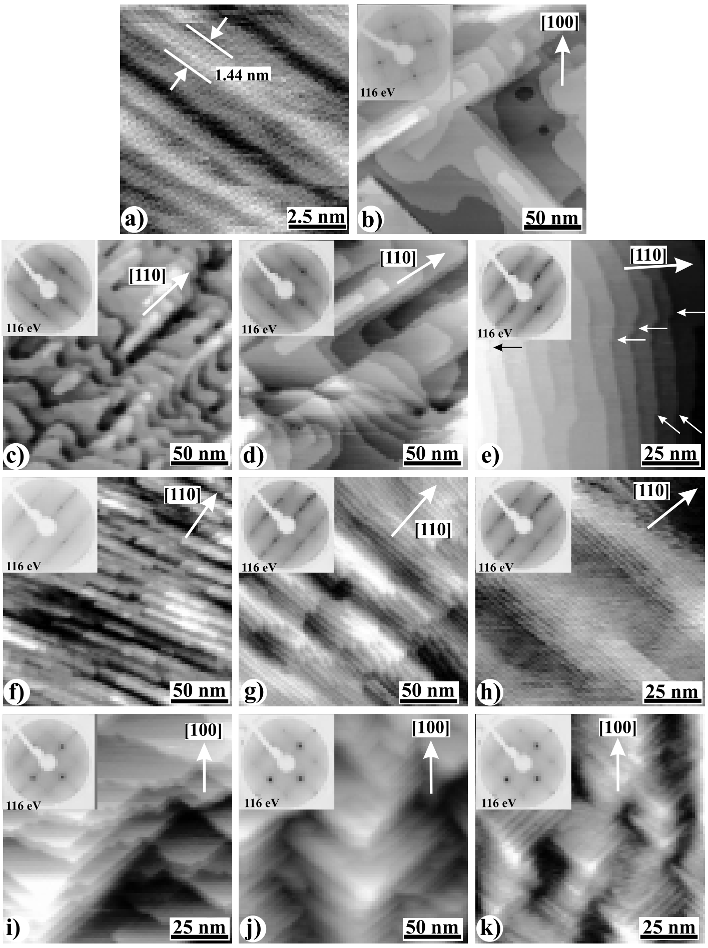

Fig. 2: STM images of the surface morphology of vicinal Au(001). The arrows indicate the direction of the miscut. a) atomic resolution of the 5 × 20 reconstruction; b) Au surface without miscut, the inset shows the corresponding LEED pattern; c) Au surface with 0.5° miscut along $[110]_{Au}$ direction; d) 1°, $[110]_{Au}$; e) 1.5°, $[110]_{Au}$, here the scan direction in the STM image is rotated by 45° with respect to the LEED image; f) 2°, $[110]_{Au}$; g) 4°, $[110]_{Au}$; h) 7°, $[110]_{Au}$; i) 2°, $[100]_{Au}$; j) 4°, $[100]_{Au}$; k) 7°, $[100]_{Au}$;

For step edges perpendicular to the $[100]_{Au}$ direction the value of Ξ decreases with increasing vicinal angle. This coincides with the decreasing size of the zig-zag-shaped terraces in both correlation directions, for which the lengths ($\xi_{||}$ and $\xi_{\perp}$) have the same values and therefore Ξ becomes almost zero. The roughness exponent α has almost the same values for both directions and therefore A becomes zero. However, for step edges perpendicular to the $[110]_{Au}$ direction a more interesting behavior is found: due to the uniaxial orientation of the step edges the anisotropy in the correlation length Ξ first increases and then decreases crossing zero at a vicinal angle of about $1.3° \pm 0.2°$. This clearly states the change of the morphology, i.e., the change of the main orientation of the step edges and the reconstruction rows, respectively. The dependence of Ξ on the vicinal angle is presented in Fig. 4.

Fe(001) grows in the *bcc* phase with a 45° rotation of its lattice about the film normal on *fcc* Au(001) with a corresponding in-plane lattice mismatch of less than 1 % [9,10]. The Fe films were deposited at room temperature at a rate of $0.006\,\mathrm{nm/s}$. By means of Auger electron spectroscopy (AES) it was found that a small amount of Au is floating on top of the Fe surface. The obtained LEED patterns (Fig. 3 (a)) confirm an epitaxial growth of Fe(001) films on Au buffers. The energy dependence of the spot width demonstrates an oscillating behavior, indicating that the atomic steps of the Fe film roughen the surface. This coincides with the STM image of Fe shown in Fig. 3 (b). Large islands with the mean island size of about $15\,\mathrm{nm}^2$ and the height of 3 to 4 monolayers are observed also in agreement with [11]. Note, that large atomically smooth terraces and the orientation of the step edges of the underlying Au buffers can clearly be traced on the Fe surface, as it is seen in Fig. 3 (c-k). The orientation of the step edges of the Fe islands is randomly distributed. This

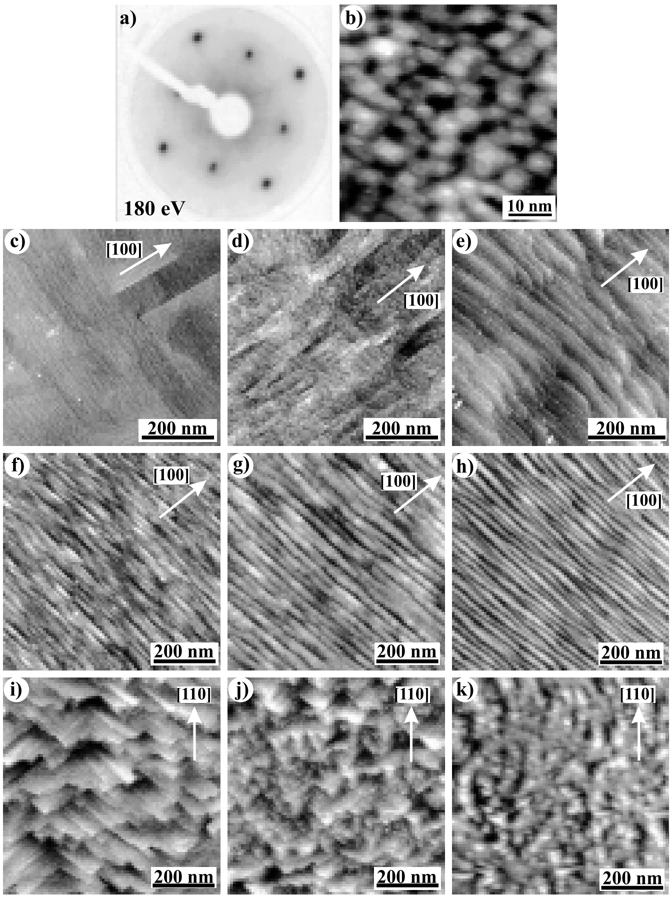

Fig. 3: STM images of the surface morphology of vicinal Fe(001) films. The arrows indicate the direction of the miscut. a) For all vicinal miscuts a typical LEED pattern (E=180 eV) is shown. b) STM image of an Fe film showing islands; c) Fe(001) surface without miscut; d) Fe topography with 0.5° miscut along $[100]_{\mathrm{Fe}}$ direction; e) 1.5°, $[100]_{\mathrm{Fe}}$; f) 2°, $[100]_{\mathrm{Fe}}$; g) 4°, $[100]_{\mathrm{Fe}}$; h) 7°, $[100]_{\mathrm{Fe}}$; i) 2°, $[110]_{\mathrm{Fe}}$; j) 4°, $[110]_{\mathrm{Fe}}$; k) 7°, $[110]_{\mathrm{Fe}}$; Note that $[110]_{\mathrm{Fe}}$ corresponds to $[100]_{\mathrm{Au}}$.

corroborates the LEED and RHEED patterns where no predominant orientation can be observed as it is the case for the reconstruction of the Au surface. Since no reconstruction on the Fe surface is present, as in the case of Au, one will find the same LEED pattern for all vicinal miscuts and different orientations as displayed in Fig. 3 (a). Since the morphology of the Au buffer is copied to the Fe layer, the angular anisotropy in the correlation length Ξ and in the roughness exponent A of the Fe films show the same behavior as functions of the vicinal angle as observed for the Au buffer layers. Additionally a short correlation length ξ of $3-5\,\mathrm{nm}$ is observed being independent of the correlation direction. This length corresponds to the mean distance of the Fe islands. The Fe grown on Au(001) surfaces is a perfect combination for lattice matched growth since the in-plane lattice mismatch is less than 1 % as already mentioned.

Magnetic anisotropies of Fe films were derived from the frequencies of the spin waves determined by means of Brillouin light scattering spectroscopy (BLS) [12, 13] and the evaluation of hysteresis loops obtained with the magneto-optical Kerr effect (MOKE) [14]. In both cases a focused laser beam was used as a probe. The Fe films were grown in the shape of a wedge, having the advantage that a large range of Fe-thicknesses (typically $0.7-8\,\mathrm{nm}$) is available on one single sample by scanning the laser beam along the wedge. Due to the extremely small slope of the wedge ($0.66\,\mathrm{nm/mm}$) the wedge shape of the Fe films does not influence the obtained results.

The total magnetic anisotropy energy density of a vicinal (001) film can be expressed by

$$E_{ani} = K^{(2)}_{s,\,eff}\cos^2\theta + K^{(4)}_{p,\,eff}\sin^4\theta\cos^2\varphi\sin^2\varphi + K^{(2)}_{p,\,eff}\sin^2\theta\sin^2(\varphi-\varphi_0) \quad , \tag{3}$$

where $K^{(2)}_{p,\,eff}, K^{(2)}_{s,\,eff}$ and $K^{(4)}_{p,\,eff}$ are the effective constants of in-plane and out-of-plane uniaxial

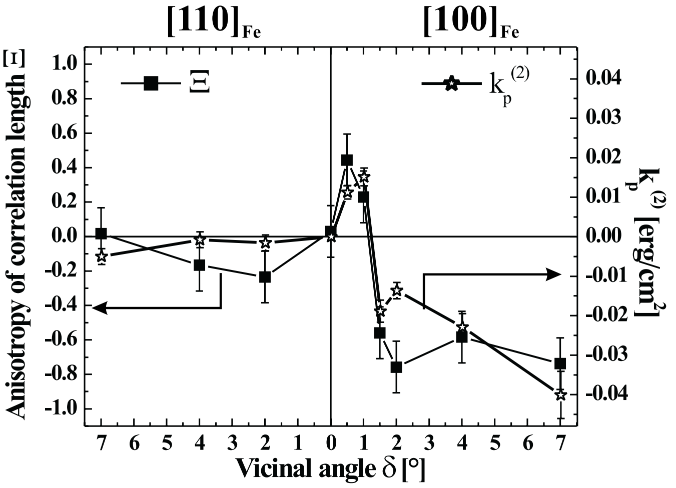

Fig. 4: Comparison of the anisotropy of the correlation length and the step induced magnetic anisotropy. For step edges perpendicular to the $[100]_{\text{Fe}}$ direction the behaviour of both curves is very similar.

and in-plane fourfold anisotropy contributions. The attribute "effective" indicates that at this stage no separation in volume and interface contribution has been made. θ and φ are the polar and the azimuthal angles of the magnetization, and the angle φ_0 determines the orientation of the uniaxial in-plane easy axis with respect to the fourfold anisotropy. For $\varphi_0 = 0$ both easy axes coincide along the $[100]_{\text{Fe}}$ miscut direction, for $\varphi_0 = 45°$ the uniaxial easy axis is along the fourfold hard axis. The anisotropy, which originates from broken bonds at the step edges due to the broken translational invariance at the surface, is the uniaxial in-plane anisotropy $K^{(2)}_{p,\,eff}$. Alternatively $K^{(2)}_{p,\,eff}$ can be determined by the evaluation of static magnetization loops with the magnetic field applied perpendicular to the easy axis [14].

To determine the thickness independent volume contribution and the thickness dependent surface contribution of the uniaxial in-plane anisotropy in detail, the dependence of $K^{(2)}_{p,\,eff}$ on the Fe film thickness was studied. For a linear dependence of the data the curve can be fitted by the usual expression $K^{(2)}_{p,eff} = K^{(2)}_{p} + \frac{2k^{(2)}_{p}}{d}$, where $K^{(2)}_{p}$ and $k^{(2)}_{p}$ describe the volume and surface contributions, respectively. For the samples with low vicinal angle (0.5° and 1°) the long side of the step edges is oriented parallel to the miscut direction as seen in the STM images in Fig. 2 (c) and (d), and the easy axis is found to be perpendicular to the miscut direction. In the case of the samples with a miscut ranging from 1.5°–7°, the easy axis is oriented perpendicular to the step edges. The evaluated dependence of $k^{(2)}_{p}$ on the miscut angle is presented in Fig. 4 for both investigated directions of the miscut. The interface contribution for the Fe films with the miscut direction along the $[110]_{\text{Fe}}$ direction $k^{(2)}_{p}$ is negligible as there is no preferred direction of the step edges. This may be due to the zig-zag-shaped steps with average direction perpendicular to $[110]_{\text{Fe}}$. The surface contribution of the anisotropy seems to annihilate itself, since the steps are oriented alternating along $[100]_{\text{Fe}}$ and $[010]_{\text{Fe}}$. For the other miscut direction along $[100]_{\text{Fe}}$ direction $k^{(2)}_{p}$ demonstrates the change of its sign in a profound way, indicating the surface nature of this effect corroborated by the LEED and STM investigations.

We have shown that the magnetism of vicinal thin Fe(001) films is strongly correlated with the surface morphology of the Au(001) buffer layers prepared on MgO(001) substrates. The Au buffers show a different morphology dependent on the direction of the miscut, i.e. $[100]_{\text{Au}}$ and $[110]_{\text{Au}}$ direction. For the miscut direction along the $[110]_{\text{Au}}$ direction an additional transition in the morphology is found. The orientation of the 5×20 reconstruction is dependent on the long edge of the step edges on the surface. As a consequence the reconstruction changes its orientation with increasing vicinal angle due to the change of the direction of the step edges at the surface as observed by LEED and STM. The epitaxial grown Fe films copy the morphology present on the Au buffer layers, although the morphology of Fe consists of large islands of $3-4\,$ML height. The magnetic uniaxial in-plane anisotropy follows the behavior introduced by the morphological changes on the surface. The surface contribution of the uniaxial in-plane anisotropy shows a significant change of sign at a vicinal angle of about $\alpha = 1.5^\circ$. This clearly proofs the surface character of $k_p^{(2)}$.

References

[1] M.L. Néel, J. Phys. Rad. **15**, 376 (1954).
[2] D.S. Chuang, C.A. Ballentine, R.C. O'Handley, Phys. Rev. B **49**, 15084 (1994).
[3] H.-N. Yang, Y.-P. Zhao, A. Chan, T.-M. Lu, G.-C. Wang, Phys. Rev. B **56**, 4224 (1997).
[4] S.K. Sinha, E.B. Sirota, S. Garoff, H.B. Stanley, Phys. Rev. B **38**, 2297 (1988).
[5] M. Rickart, B.F.P. Roos, T. Mewes, J. Jorzick, S.O. Demokritov, B. Hillebrands, Surf. Sci. **495**, 68 (2001).
[6] M. Rickart, S.O. Demokritov, B. Hillebrands, J. Phys: Cond. Mat. **14**, 8947 (2002).
[7] D.G. Fedak, N.A. Gjostein, Surf. Sci. **8**, 77 (1967).
[8] G. Binnig, H. Rohrer, C. Gerber, E. Stoll, Surf. Sci. **144**, 321 (1984).
[9] P. Grünberg, S. Demokritov, A. Fuss, R. Schreiber, J.A. Wolf, S.T. Purcell, J. Magn. Magn. Mat. **104-107**, 1734 (1995).
[10] J.J. Krebs, B.T. Jonker, G.A. Prinz, J. Appl. Phys. **61**, 2596 (1987).
[11] D.E. Bürgler, C.M. Schmidt, J.A. Wolf, T.M. Schaub, H.-J. Güntherodt, Surf. Sci. **366**, 295 (1996).
[12] S. Demokritov, E. Tsymbal, J. Phys.: Cond. Mat. **6**, 7145 (1994).
[13] B. Hillebrands, *Brillouin light scattering from layered magnetic structures*, Topics in Applied Physics **75** (2000).
[14] W. Weber, R. Allenspach, A. Bischof, Appl. Phys. Lett. **70**, 520 (1997).
[15] B. Hillebrands, Phys. Rev. B **41**, 530 (1990).

C. Exchange Bias Effect

6.9 Spacer induced variation of the coupling strength in the exchange bias FeMn/Cu/NiFe system

H. Nembach, T. Mewes, M. Blanco-Mantecón, S.O. Demokritov, J. Fassbender, and B. Hillebrands

The mechanism of the coupling between a ferromagnet and an antiferromagnet is still subject of debate. To shed more light on this a single crystalline system of a ferromagnetic and an antiferromagnetic layer separated by a metallic spacer layer of varying thickness has been studied. We chose the epitaxial (001)-oriented $Fe_{50}Mn_{50}/Cu/Ni_{81}Fe_{19}$ trilayer system. Details of the growth process have been reported elsewhere [1, 2]. The thicknesses of the $Fe_{50}Mn_{50}$ and the $Ni_{81}Fe_{19}$ layers are 10 nm and 5 nm respectively. The Cu spacer layer was grown as a wedge with a thickness ranging from 0 to 0.8 nm. This allows us the determination of the magnetic properties as a function of the interlayer thickness on a single sample. Therefore deviations caused by different preparation conditions can be excluded. A unidirectional anisotropy was induced by cooling the sample from above the Néel temperature with an applied field pointing along the [100]-direction of $Ni_{81}Fe_{19}$. The [100]-direction is collinear to an easy direction of the induced four-fold anisotropy as determined by Brillouin light scattering spectroscopy. Hysteresis curves were measured with MOKE magnetometry along the wedge with the applied field along the [100]-direction. With increasing Cu thickness the absolute value of the exchange bias field H_{eb} decreases exponentially with a superimposed oscillation $H_{eb,osc}$, see Fig. 1:

$$H_{eb}(d_{cu}) = H_{eb,exp}(d_{cu}) + H_{eb,osc}(d_{cu}) \quad . \tag{1}$$

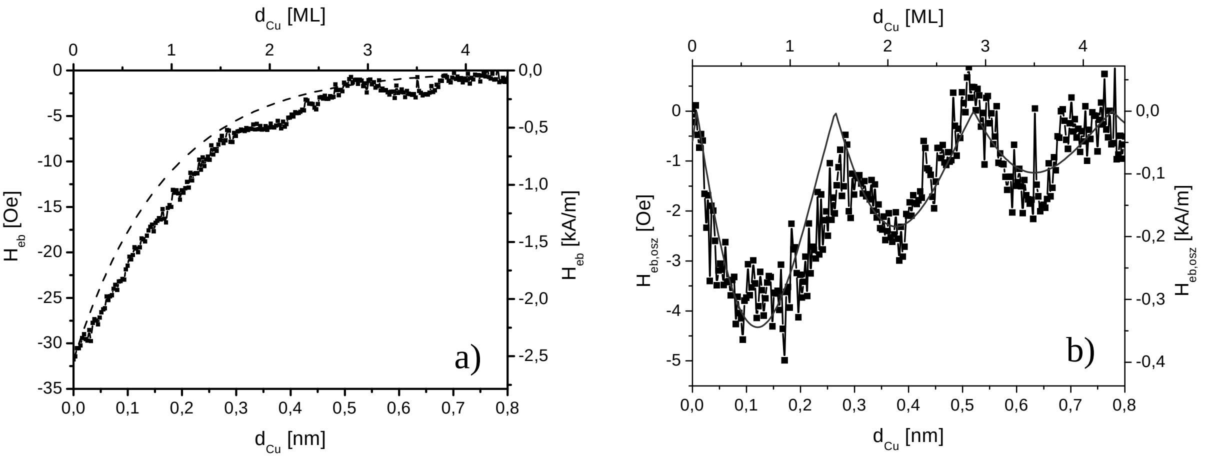

Fig. 1: a) Exchange bias field H_{eb} as a function of the Cu interlayer thickness. The dashed line shows the exponentially decaying contribution. b) Oscillating contribution to the exchange bias field $H_{eb,osc}$ after substracting the exponential part. The line shows a fit to the data using Eq.(2).

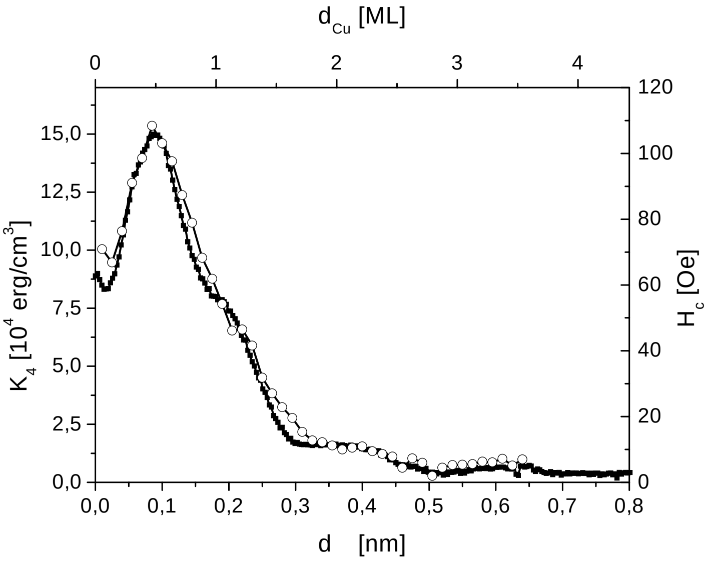

Fig. 2: Coercive field H_C (closed symbols) and biaxial anisotropy K_4 (open symbols) as a function of the Cu interlayer thickness.

The exponential contribution $H_{eb,exp} = H_{eb,0}e^{-d_{Cu}/L}$ is characterized by a decay length $L = (0.17 \pm 0.02)\,\mathrm{nm}$. The oscillatory contribution can be described by the following equation, see [3]:

$$H_{eb,osc} = -A_0 e^{-d_{Cu}/L_{osc}} \left| \cos\left(2\pi \frac{d_{Cu}}{\lambda} - \phi\right) \right| \quad , \tag{2}$$

with A_0 the amplitude, L_{osc} the decay length, λ the period and ϕ the phase of the oscillation. A fit to the experimental data in Fig. 1 results in an amplitude of $A_0 = (5.9 \pm 0.5)\,\mathrm{Oe}$ and a decay length $L_{osc} = (0.41 \pm 0.05)\,\mathrm{nm}$. The oscillation periode is $\lambda = (0.51 \pm 0.01)\,\mathrm{nm} = (2.77 \pm 0.06)\,\mathrm{ML}$ and the phase is $\phi = 96^\circ \pm 3^\circ$. Equation (2) is derived under the assumption that the exchange bias field is proportional to the absolute value of the interlayer coupling strength J. This is supported by current microscopic models describing the exchange bias effect. The oscillations described by Eq. (2)

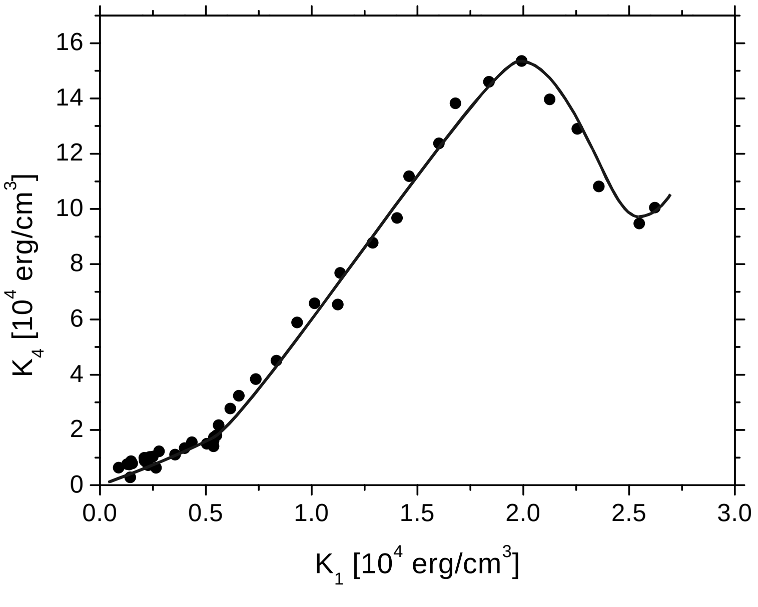

Fig. 3: Biaxial anisotropy K_4 as a function of the unidirectional anisotropy K_1. The open symbols show the experimental values, the line is a guide to the eye.

are understood by a Ruderman-Kittel-Kasuya-Yoshida (RKKY) type interlayer coupling, which leads to an oscillation of the interlayer coupling strength J with the interlayer thickness. P. Bruno and C. Chappert have predicted [4,5] for ferromagnetic trilayer systems with a Cu(001)-interlayer a short and a long oscillation period with 2.56 ML and 5.88 ML, respectively. The oscillation period of 2.77 ML observed here for the exchange bias field agrees well with the predicted short oscillation periode for interlayer coupling. The long oscillation periode could not be observed because the exchange bias field H_{eb} decays too rapidly limiting the accessible interlayer thickness range. The dependence of H_C on the Cu interlayer thickness can be attributed to a corresponding variation of the induced biaxial anisotropy as can be seen in Fig. 2. The biaxial anisotropy was determined by Brillouin light scattering measuring the spinwave frequencies along the easy [100]-direction and the hard [110]-direction as a function of the Cu thickness. The biaxial anisotropy shows a pronounced maximum for a Cu interlayer thickness of about 0.5 ML and then decreases with increasing Cu interlayer thickness. In Fig. 3 the properties of the system are summarized by showing the induced biaxial anisotropy as a function of the unidirectional anisotropy $K_1 = -H_{eb}/M_s$. The nonlinear and nonmonotonic relation between these two anisotropies is in agreement with recent micromagnetic calculations [6,7] which suggest that the induced higher order anisotropies and the exchange bias effect, i.e. the unidirectional anisotropy, have different microscopic origins.

References

[1] T. Mewes, M. Rickart, A. Mougin, S.O. Demokritov, J. Fassbender, B. Hillebrands, M. Scheib, Surf. Sci. **481**, 87 (2001).

[2] T. Mewes, H. Nembach, M. Rickart, S.O. Demokritov, J. Fassbender, B. Hillebrands, Phys. Rev. B **65**, 224423 (2002).

[3] T. Mewes, B.F.P. Roos, S.O. Demokritov, B. Hillebrands J. Appl. Phys. **87**, 5064 (2000).

[4] P. Bruno, C. Chappert, Phys. Rev. Lett. **67**, 1602 (1991).

[5] P. Bruno, C. Chappert, Phys. Rev. B **46**, 261 (1992).

[6] T.C. Schultess, W.H. Butler, Phys. Rev. Lett. **81**, 2516 (1998).

[7] T.C. Schultess, W.H. Butler, J. Appl. Phys. **85**, 5510 (1999).

6.10 Probing the interface magnetism in the $Fe_{50}Mn_{50}/Ni_{81}Fe_{19}$ exchange bias system using second harmonic generation

S. Poppe, T. Mewes, J. Fassbender and B. Hillebrands[1]

The presented results have been obtained during and following a sabbatical stay of Burkard Hillebrands in the group of Jacques Ferré at the Université Paris Sud, Orsay. The second harmonic generation measurements and the data analysis have been performed in Orsay. The samples and the ion irradiation were made in Kaiserslautern.

The magnetic exchange interaction between an antiferromagnetic (AFM) and an adjacent ferromagnetic (FM) layer leads under certain conditions to the exchange bias coupling, resulting in a shift of the magnetization reversal of the FM layer along the field axis. Several models have been proposed in order to account for this employing (i) domain walls or partial domain walls in the AFM layer which are either parallel or perpendicular to the interface, and (ii) uncompensated magnetic moments of the AFM layer at the interface or in the bulk of the AFM layer. Especially in systems with otherwise compensated spin structure at the interface, most models rely on the presence of uncompensated spins at the FM/AFM interface resulting in a residual net moment. This moment is supposed to act as an internal field on the FM layer resulting in exchange bias.

The second-harmonic magneto-optic Kerr effect (SHMOKE) is ideally suited to deliver information about the magnetism of buried interfaces. Here we report on the first successful application of SHMOKE to an exchange bias system, revealing the magnetic properties of the interface between a FM and a AFM layer. A second-harmonic signal in centrosymmetric materials like $Ni_{81}Fe_{19}$ and $Fe_{50}Mn_{50}$ is selectively generated within 2 monolayers around the interfaces where symmetry is broken. Polycrystalline bilayers of $Ni_{81}Fe_{19}$ and $Fe_{50}Mn_{50}$ were used in order to benefit from the reported tailoring of the exchange bias coupling by ion irradiation [1]. For details of sample preparation see Chapter 6.11. After preparation, different areas of one sample were irradiated with $5\,\mathrm{keV}$ He^+ ions in a dose range between $9 \cdot 10^{13}\,\mathrm{ions/cm^2}$ and $2 \cdot 10^{16}\,\mathrm{ions/cm^2}$ leading to a variation of the exchange bias field H_{eb} between $100\,\mathrm{Oe}$ and $350\,\mathrm{Oe}$. SRIM (Stopping and Range of Ions in Matter [2]) calculations show that the interface width is not significantly increased with ion doses less than $10^{16}\,\mathrm{ions/cm^2}$.

In general, the second harmonic polarization, $\mathbf{P}(2\omega)$, generated at a single interface, consists of two contributions resulting from the magnetic optical susceptibility tensor $\chi_m^{(2)}$ and the non-magnetic one, $\chi_{nm}^{(2)}$. For calculating the SHMOKE intensity, effective susceptibilities χ_m and χ_{nm} (both complex numbers) are used which are functions of the elements of the tensors $\chi_m^{(2)}$ and $\chi_{nm}^{(2)}$, and depend on the measurement configuration. Since each interface of a multilayer sample contributes to the SHMOKE signal, one has to evaluate all of them (here $Cu/Fe_{50}Mn_{50}$, $Fe_{50}Mn_{50}/Ni_{81}Fe_{19}$, $Ni_{81}Fe_{19}/Cr$, and Cr/air) in order to extract information about the magnetization of the FM/AFM interface. Due to the same crystallographic structure of the $Fe_{50}Mn_{50}$ and $Ni_{81}Fe_{19}$ layers, χ_{nm} from this interface has a rather small value, independent of the measurement configuration. In contrast, most of the magnetic SH signal originates from the $Fe_{50}Mn_{50}/Ni_{81}Fe_{19}$ interface we are interested in.

---

[1] In collaboration with L.C. Sampaio, A. Mougin, J. Ferré, P. Georges, A. Brun, H. Bernas, Université Paris Sud, France.

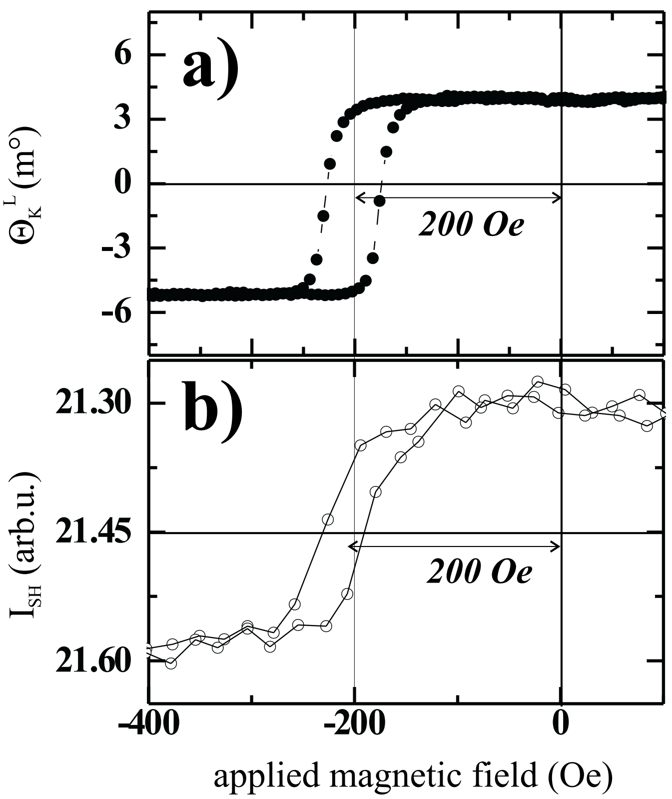

Fig. 1: Bulk and interfacial magnetization reversal loops measured by linear MOKE (a), and SHMOKE (b), respectively. θ_K^L is the linear Kerr rotation and I_{SH} is the SHMOKE intensity in the transversal configuration.

SHMOKE experiments were performed in Orsay with a home made mode-locked Ti:Sapphire laser operating at a central wavelength of 800 nm emitting pulses of 100 fs width with a repetition rate of 86 MHz. Using a p-polarized laser beam at an angle of incidence of 45°, the SH signal was measured in the transversal configuration and in the longitudinal one in combination with a polarisation analysis. Figure 1 (b) shows a magnetization loop measured in the transversal configuration, i.e., the SH intensity is measured as a function of the applied field, which is oriented perpendicular to the plane of incidence and parallel to the exchange bias direction. Since χ_{nm} of the $Fe_{50}Mn_{50}/Ni_{81}Fe_{19}$ interface has a small value, the transverse magnetic SH intensity is related to this interface [4, 5]. Within the error bars, an exchange bias field of 200 Oe for the interface magnetization is observed, consistent with the linear MOKE measurements shown in Fig. 1 (a).

Moreover, the same ion fluence dependence of the exchange bias field is observed both with SHMOKE and linear MOKE (see Fig. 2 (a)).

A more quantitative measure of the in-plane component in the magnetization at the interface along the unidirectional coupling direction was performed the following way. Since both magnetic and non-magnetic contributions enter the SHMOKE signal, the fluence dependence of the non-magnetic part was determined in order to separate out the magnetic one. This was obtained by evaluating the average SHMOKE intensity $\bar{I}$ in the transversal configuration:

$$\bar{I} = \frac{I_{2\omega}^{+H}+I_{2\omega}^{-H}}{2} \propto \alpha\chi_{nm}^2+\beta\chi_m^2 \approx \alpha\chi_{nm}^2 \quad . \tag{1}$$

α and β are the effective Fresnel factors [4]. Usually, $\bar{I}$ reproduces the effective non-magnetic optical susceptibility because the magnetic term is negligibly small compared to the average part of the SH intensity [5]. $\bar{I}$ and thus also χ_{nm} is shown in Fig. 2 (b) as a function of ion fluence. Almost no evolution with the ion fluence is observed, which further supports the assumption that

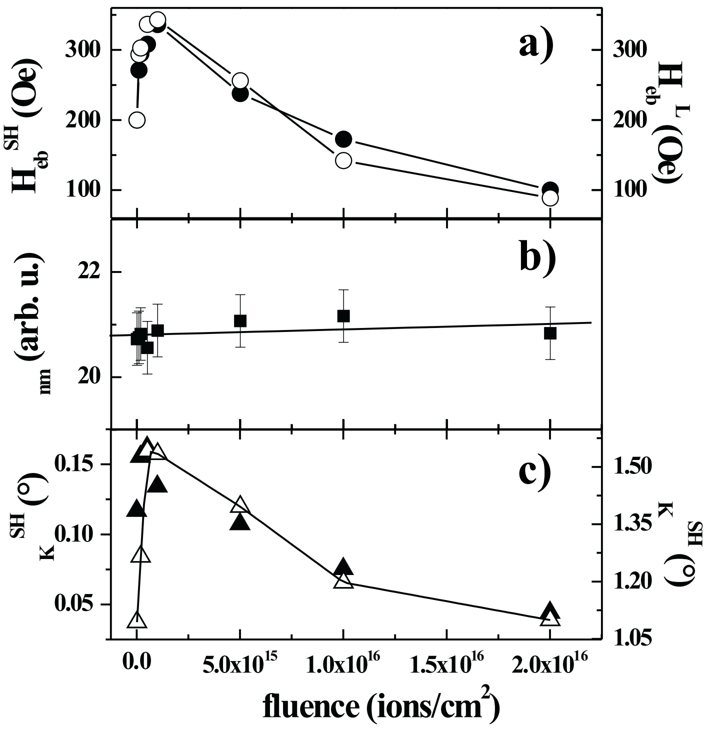

Fig. 2: Ion fluence dependence of: a) exchange bias field (full symbols: MOKE, open symbols: SHMOKE), b) non-magnetic contribution to the SHMOKE signal in transversal configuration, and c) the SH Kerr rotation θ_K^{SH} (empty triangles, left scale) and the ellipticity ε_K^{SH} (full triangles, right scale) in longitudinal configuration. Solid lines are guides to the eye.

the interfaces are not significantly broadened upon irradiation. This is particular true for the upper $Ni_{81}Fe_{19}$/Cr and Cr/air interfaces (which give the main contribution to $\bar{I}$). However, considering our SRIM calculations, this also holds for the $Fe_{50}Mn_{50}/Ni_{81}Fe_{19}$ interface of interest.

The magnetic contribution to the SH signal was then determined by measuring the intensity asymmetry, given by

$$A_L = \frac{I_{2\omega}^{+H} - I_{2\omega}^{-H}}{I_{2\omega}^{+H} + I_{2\omega}^{-H}} = \frac{2R_L\ \tan\psi \cdot \cos\varphi_L}{1 + R_L^2\ (\tan\psi)^2} \tag{2}$$

in the longitudinal configuration. φ_L is the phase angle between χ_m and χ_{nm}, and ψ the analyzer angle. R_L is given by $|\frac{\chi_m}{\chi_{nm}}|_L$. The SH Kerr rotation and ellipticity are given by $\theta_K^{SH} = |\Phi| \cdot \cos\varphi_L$ and $\varepsilon_K^{SH} = |\Phi| \cdot \sin\varphi_L$, respectively, where $\pm\cos\varphi_L$ are the extremal values of the asymmetry A_L at the analyzer angle positions $90° \pm |\Phi|$. Usually, θ_K^{SH} and ε_K^{SH} reflect the ratio of the effective magnetic and non-magnetic contribution to the total SH signal. Since the effective non-magnetic contribution is constant, they are directly proportional to the magnetization component along the magnetic field [3]. Moreover, the magnetic component from which the SH signal arises, is engendered by the AFM/FM interface: i) no signal is expected from the bulk AFM layer; at its interface with Cu, each sublattice could have a SH contribution but it is unlikely that those exhibit the same fluence/field behavior as A_L; ii) as pointed out before, χ_{nm} from the $Fe_{50}Mn_{50}/Ni_{81}Fe_{19}$ interface is rather small. Subsequently, R_L associated with the $Fe_{50}Mn_{50}/Ni_{81}Fe_{19}$ interface is much larger than R_L originating from the upper $Ni_{81}Fe_{19}$/Cr interface. Therefore, the magnetic signal originates mainly from the FM/AFM interface we are interested in.

In summary, the ion fluence dependence of the SH Kerr rotation and ellipticity is directly related to the configuration of the AFM interfacial spins. It is shown in Fig. 2 (c) compared to the evolution of the exchange bias field measured with linear (full symbols) and SH (open symbols) MOKE in Fig. 2 (a). The evolution of the SH Kerr rotation and ellipticity with ion fluence reproduces that of the exchange bias field whereas the linear Kerr rotation (not shown), which describes the behavior of the bulk FM layer, is constant in the same fluence regime [1].

As the main conclusion, our measurements clearly prove that along the bias direction an in-plane ferromagnetic component occurs in the vicinity of the FM/AFM interface showing a reversal loop similar to that of the bulk FM layer. Its size scales perfectly with the macroscopic exchange bias field. Finally, we have shown that the second-harmonic magneto-optic Kerr effect is a vital tool to investigate the interface magnetism in exchange bias systems.

Support by the Deutsche Forschungsgemeinschaft, CNPq/Brazil, and CNRS is gratefully acknowledged. T.M. acknowledges support by the Studienstiftung des Deutschen Volkes. B. H. acknowledges support by CNRS during his sabbatical stay at the Université Paris Sud, Orsay.

References

[1] A. Mougin, T. Mewes, M. Jung, D. Engel, A. Ehresmann, H. Schmoranzer, J. Fassbender, B. Hillebrands, Phys. Rev. B **63**, 060409R (2001).

[2] J.F. Ziegler, J.P. Biersack, U. Littmark, The Stopping and Range of Ions in Solids. Pergamon, New York, Oxford (1985).

[3] K.H. Bennemann, *Non linear optics in metals*. chap. 2 and 3, Clarendon Press, Oxford (1998).

[4] J. Güdde, U. Conrad, V. Jähnke, E. Matthias, Phys. Rev. B **59**, 6608 (1999).

[5] J. Hohlfeld, E. Matthias, R. Knorren, K.H. Bennemann, Phys. Rev. Lett. **78**, 4861 (1997).

6.11 In-situ irradiation of NiFe/FeMn exchange bias bilayers

S. Poppe, J. Fassbender, and B. Hillebrands

Recently, it has been shown that the exchange bias field of $Ni_{81}Fe_{19}/Fe_{50}Mn_{50}$ bilayers can be modified by means of He ion irradiation. A phenomenological model has been proposed which is based on structural effects in the antiferromagnetic (AFM) layer and at its interface to the ferromagnetic (FM) layer [1]. Defects placed in the AFM layer are supposed to act as pinning sites for domain walls. Irradiation thereby reduces the average size of domains in the AFM layer and increases the shift field [2]. Bombardment of the AFM/FM interface is supposed to cause intermixing and thus decreases the coupling between both layers resulting in an exponential decay of the shift field with high ion doses. For a more detailed description of the model see Ref. [1]. The main purpose of the present work is to test the assumptions of the model. Therefore, the irradiation has been performed *in-situ* between the various deposition steps of the layers. Hence, the influence of ion bombardment has been restricted to certain layers of the sample, and different contributions to the effect were examined separately.

All samples are polycrystalline and have been prepared by thermal evaporation in a UHV-system with a background pressure of $5 \cdot 10^{-10}$ mbar. A 150 Å thick Cu buffer has been deposited on top of a thermally oxidized Si substrate in order to promote (111) texture of the following layers. For the FM (AFM) layer 50 Å (100 Å) of $Ni_{81}Fe_{19}$ ($Fe_{50}Mn_{50}$) has been used. Samples with the AFM layer on top of (below) the FM layer will be denoted “top configuration” (“bottom configuration”) samples in the text. The stacking sequence has no significant effect on the observed exchange bias field (typically 180 Oe) or the dose dependence after irradiation. Finally the sample is covered with 20 Å Cr to protect it from oxidation. The ion source is attached to the same vacuum system and is operated with 5 keV He ions. Background pressure during irradiation is $5 \cdot 10^{-8}$ mbar. Different ion doses can be exposed onto several areas of one sample by scanning the ion beam and changing exposure time. All magnetic characterization has been done using magnetooptical Kerr effect (MOKE) magnetometry in longitudinal geometry. The dose dependence of the exchange bias field for a sample that has been irradiated after complete preparation is shown in Fig. 2 (full symbols). A strong enhancement of the shift field is observed for low ion doses. At higher doses, the shift field drops in an exponential manner.

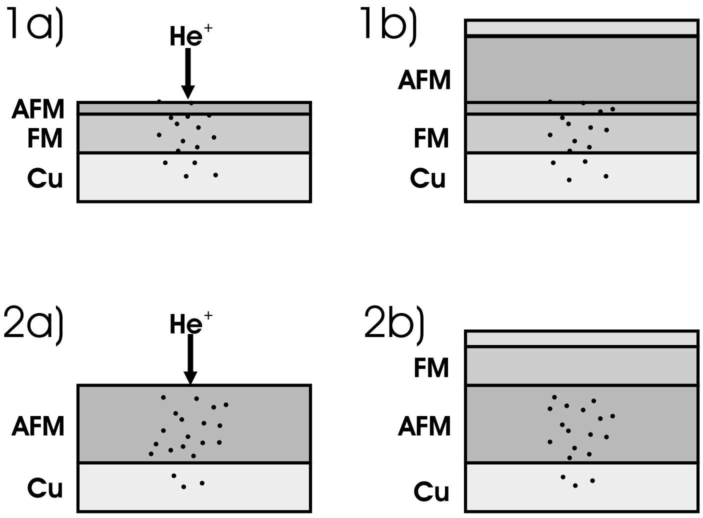

Fig. 1: Scheme of the experiments for investigation of defects in 1) the interface region only, 2) the volume AFM layer only. Black dots symbolize created defects.

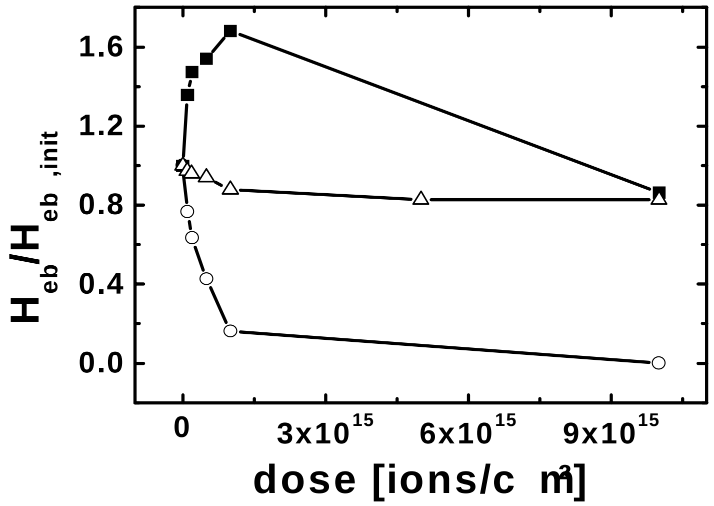

Fig. 2: Dose dependence of H_{eb} normalized to the as-prepared value. Closed squares: irradiation after completed growth; open circles: irradiation of the interface region according to Fig. 1-1; open triangles: irradiation of the AFM layer only as in Fig. 1-2.

First, we discuss the influence of ion bombardment at the AFM/FM interface only. For this purpose, a sample in "top configuration" was prepared. Growth of the AFM layer was stopped at a thickness of 15 Å. At that thickness the interface should be well defined but the sample exhibits neither bias shift nor coercivity enhancement, yet. Several areas with ion doses ranging from $9 \cdot 10^{13}$ ions/cm^2 to $2 \cdot 10^{16}$ ions/cm^2 were irradiated on the sample. During the bombardment a field of 30 Oe was applied to saturate the FM layer. Afterwards, deposition of the AFM layer was completed to obtain a total thickness of 100 Å. A scheme of the experiment is shown in Fig. 1(a).

The sample was then heated above the blocking temperature at 200 °C and cooled in an applied field of 250 Oe to initialize the exchange bias. It should be stated that the absolute value of H_{eb} at zero dose is reduced to 80 Oe in this sample. This is probably due to contaminations of the surface during irradiation and a thereby reduced overall coupling. In Fig. 2 the corresponding dose dependence of the normalized exchange bias field is shown (open circles). In contrast to irradiation after completed growth (Fig. 2, closed squares) only a decay of the exchange bias field is observed. This is consistent with the model, since no defects in the bulk AFM layer have been induced.

In a second experiment the effect of bombardment on the volume AFM layer was studied. Therefore, the AFM layer was grown first completely and irradiated. Then the $Ni_{81}Fe_{19}$ and Cr layers were deposited. The sample was also annealed under the same conditions and exhibited a shift field of 180 Oe on unirradiated areas. Although within our model a strong increase of H_{eb} is expected, the exchange bias field displays only a weak dependence on the ion dose (Fig. 2, open triangles). In contrast to the previous experiment where the AFM/FM interface was present during irradiation (cf. open circles in Fig. 2) no exponential-like decay to zero is observed. Only a slight reduction of the bias field is observed which can be attributed to interface contamination during the irradiation process.

This result leads to the conclusion that the FM layer has to be present during irradiation for the enhancement mechanism to work. The question remains how the FM layer affects the modification process. One possible mechanism is that elastic stress/strain induced by the FM layer influence the interaction of the atoms with the penetrating ions. Another reason could be that the magnetic interaction between both layers is required. In order to answer this, a third experiment was carried out.

A sample in "top configuration" was grown completely in one step and annealed afterwards. Then, half of the sample area was irradiated at room temperature and the remaining area of the sample was irradiated at a temperature of 260 °C. This temperature is above the Néel temperature of

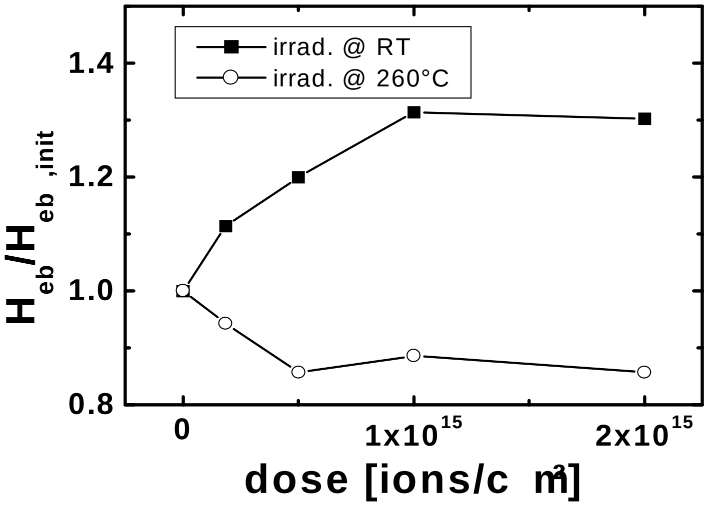

Fig. 3: Dose dependence of H_{eb} for a sample irradiated after complete preparation. Closed squares: irradiation at room temperature; open circles: irradiation at 260 °C.

$Fe_{50}Mn_{50}$ and thus the coupling between the AFM spins is eliminated whereas elastic forces should persist. Subsequently, the whole sample was annealed in an applied field at 200 °C. The resulting dose dependencies of H_{eb} for both cases are shown in Fig. 3. Only the part of the sample which was irradiated with the AFM order present shows an enhancement of the exchange bias field. Irradiation at 260 °C only leads to a decay. Consequently, elastic strains can be ruled out as the origin of the discussed enhancement mechanism.

The mechanism for reduction and suppression of the exchange bias effect by ion irradiation in the $Ni_{81}Fe_{19}/Fe_{50}Mn_{50}$ system has clearly been identified to be caused by interactions of the ions with the atoms in the vicinity of the FM/AFM interface. Most likely, this effect can be attributed to interface mixing. The modifications that cause the enhancement of the bias field do not take place at the interface but in the volume of the AFM layer. These findings are consistent with the models as proposed in Refs. [1,4]. Following those assumptions further, one expects a strong linear enhancement of the exchange bias field in the case of the second experiment. Due to the induced defects, after a field-cooling procedure the AFM layer will develop more domains compared to the as-prepared case and therefore exhibit stronger bias, especially as the suppressing effect of interface mixing is avoided in this experiment. The FM layer is not involved in this scenario at all. Surprisingly, our experiment leads to the conclusion that the FM layer has to be present during irradiation. Our third experiment shows that it is not due to potential elastic effects caused by the presence of the FM layer, since these effects should persist at temperatures of 260° C. In contrast, one has to conclude that both the magnetic order in the AFM layer and the exchange coupling to a FM layer are necessary for the enhancement mechanism to work. The (saturated) FM layer is needed to provide a preferred direction in which the bias is optimized during irradiation.

In conclusion, we have shown that the observed enhancement of the exchange bias field in irradiated $Ni_{81}Fe_{19}/Fe_{50}Mn_{50}$ bilayers is caused by modifications of the bulk AFM layer. Our findings cannot be explained in terms of a pure statistical domain size argument, and in this point this differs from the phenomena observed in diluted antiferromagnets. The influence of the magnetic exchange force across the FM/AFM interface has to be taken into account. Suppression of the exchange bias effect can be attributed to changes at the FM/AFM interface.

Fruitful discussions with R.L. Stamps and M.D. Stiles are gratefully acknowledged. This work was supported by the Deutsche Forschungsgemeinschaft.

References

[1] A. Mougin, T. Mewes, M. Jung, D. Engel, A. Ehresmann, H. Schmoranzer, J. Fassbender, B. Hillebrands, Phys. Rev. B **63**, 060409R (2001).
[2] A.P. Malozemoff, Phys. Rev. B **35**, 3679 (1987).
[3] J.F. Ziegler, J.P. Biersack, U. Littmark, The Stopping and Range of Ions in Solids. Pergamon, New York, Oxford (1985).
[4] P. Miltényi, M. Gierlings, J. Keller, B. Beschoten, G. Güntherodt, U. Nowak, K.D. Usadel, Phys. Rev. Lett. **84**, 4224 (2000).

6.12 Phase diagrams of exchange bias systems with additional fourfold anisotropy

T. Mewes, H. Nembach, J. Fassbender, and B. Hillebrands[1]

Phase diagrams have been shown to be a useful tool for describing magnetic ordering in an applied field in uniaxial ferromagnets [1, 2]. We have extended the idea to magnetic heterostructures and present a detailed analysis of the magnetic ordering in exchange biased bilayers. In the following we use a general form of the free enthalpy which includes unidirectional and fourfold in-plane anisotropy contributions:

$$\begin{aligned} g = \; & - \; K_1 \cos(\alpha_M) \\ & + \; K_4 \sin^2(\alpha_M - \alpha_4) \cos^2(\alpha_M - \alpha_4) \\ & - \; H M_S \cos(\alpha_M - \alpha_H) \quad , \end{aligned} \tag{1}$$

where K_1 and K_4 denote the unidirectional and fourfold in-plane anisotropy constants respectively. The situation here resembles an epitaxial (001)-oriented ferromagnetic layer with intrinsic fourfold anisotropy exchange coupled to an antiferromagnetic layer. The more simple case of uniaxial and unidirectional anisotropy has already been discussed in the literature [6]. The easy direction of the unidirectional anisotropy for $K_1 > 0$ is chosen as a reference for the definition of angles specifying the orientation of the applied field α_H, the easy axis and the fourfold anisotropy α_4. The calculation of phase diagrams and magnetization reversal in the examples which follow is performed by minimizing the free enthalpy with respect to the angle of the magnetization α_M. In order to do this we use the so called perfect delay convention [3], which assumes that the magnetization remains in

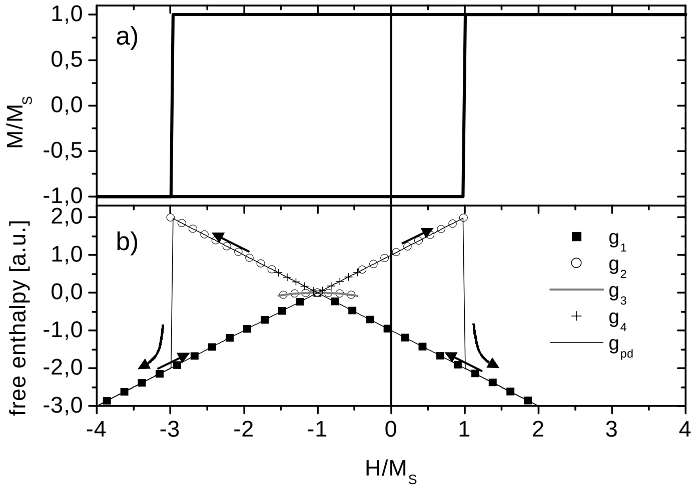

Fig. 1: a) Magnetization reversal for a system with unidirectional and fourfold anisotropy with $K_1/K_4 = 1$, using the perfect delay convention. The field is applied along the easy direction of the unidirectional anisotropy. b) Field dependence of the four different minima of the free enthalpy $g_1 \dots g_4$ and of the free enthalpy during reversal assuming perfect delay g_{pd}.

---

[1] In collaboration with J.V. Kim and R.L. Stamps, University of Western Australia, Perth, Australia.

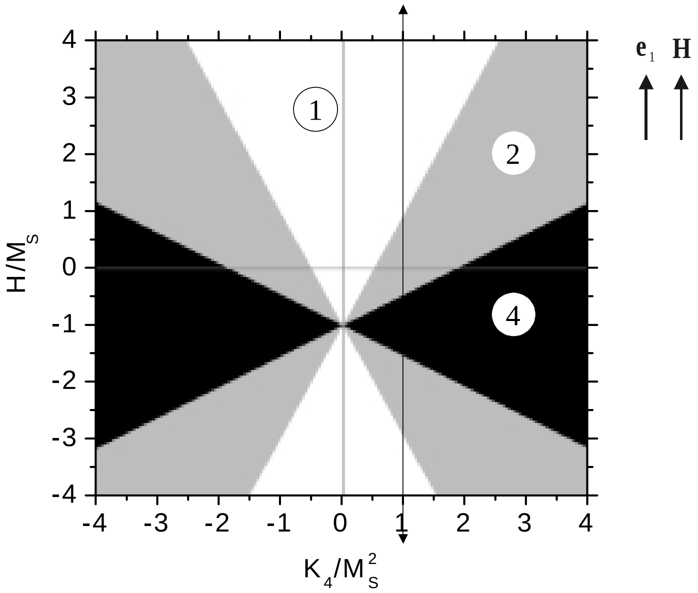

Fig. 2: Phase diagram of a system with fixed unidirectional anisotropy $K_1/M_S^2 = 1$ and variable fourfold anisotropy K_4 with the field aligned along the easy direction of the unidirectional anisotropy. The phases with one, two and four minima in the free enthalpy are labeled 1, 2 and 4 accordingly. The position of the magnetization reversal given in Fig. 1 is indicated by a double arrow. Note that for $K_4 > 0$ the easy direction of the unidirectional anisotropy is parallel to the easy axis of the fourfold anisotropy while for $K_4 < 0$ the easy direction of the unidirectional anisotropy is parallel to the hard axis of the fourfold anisotropy.

the local minimum of the free enthalpy as long as this minimum exists. The perfect delay convention results in hysteretic behavior and gives an upper limit for the coercivity. We focus here on the effects of the ratio of the different anisotropy contributions. A detailed analysis of the influence of the direction of the applied magnetic field will be given elsewhere [4]. When the external magnetic field is applied along the easy direction of the unidirectional anisotropy a magnetization reversal as shown in Fig. 1(a) results.

The magnetization reversal exhibits a coercivity as expected for coherent rotation for a fourfold anisotropy of magnitude K_4. A discontinuous change of the magnetization direction accompanied by a discontinuous change of the free enthalpy of the system occurs as can be seen in Fig. 1(b). The reason for this can be understood by following the path of the magnetization reversal in the phase diagram shown in Fig. 2. This phase diagram has the same structure as a phase diagram for a system with a fourfold anisotropy only, but it is shifted along the field axis due to the presence of the unidirectional anisotropy. Three different phases can be seen in Fig. 2: phase 1 where only one minimum exists in the free enthalpy; and phases 2 and 4 where two and four minima of the free enthalpy exist.

The phase boundaries separating phase 1 and phase 2 are of special importance for the magnetization reversal shown in Fig. 1. In this case $K_4 > 0$ and the transition from phase 2 to phase 1 with changing applied field occurs via an associated instability of the magnetic configuration. This is due to the discontinuous change of the free enthalpy which accompanies the discontinuous change of the magnetization direction at the phase boundary. Note that there are possible states present in the phase diagram that may not be accessed during the course of magnetization reversal. The reason is that the system remains in a local minimum until the configuration either becomes unstable, or thermal fluctuations are larger than the energy barrier stabilizing the state. A state such as that with enthalpy g_3 in Fig. 1 can only be accessed by thermal excitation of the system over a rela-

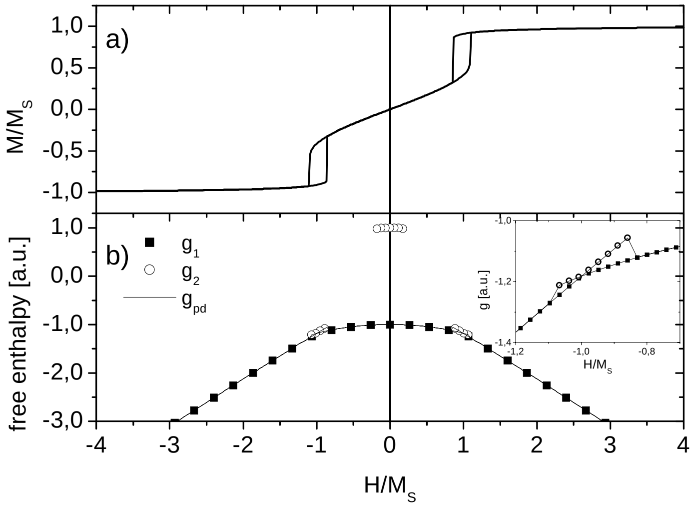

Fig. 3: a) Magnetization reversal for a system with unidirectional and fourfold anisotropy with $K_1/K_4 = 1$. The field is applied perpendicular to the easy direction of the unidirectional anisotropy. b) Field dependence of two different minima of the free enthalpy, g_1, g_2, and of the free enthalpy during reversal assuming perfect delay g_{pd}, a magnified view for $H = -1.2 \ldots -0.7$ is shown in the inset.

tively high energy barrier. A detailed description of the influence of thermal activation is given in Chapter 6.13. No shift of the magnetization reversal along the field axis is observed if the magnetic field is applied perpendicular to the easy axis. Minor hysteresis loop features such as those shown in Fig. 3 appear depending on the ratio of the anisotropy constants ($K_1/K_4 = 1$ in this figure). The reason for this complicated behavior are the different phases present in the system, where one, two, three and four minima exist in the free enthalpy. The multiple minima for this choice of values are indicated in Fig. 4. The magnetization reversal process shown in Fig. 3 involves phases with one

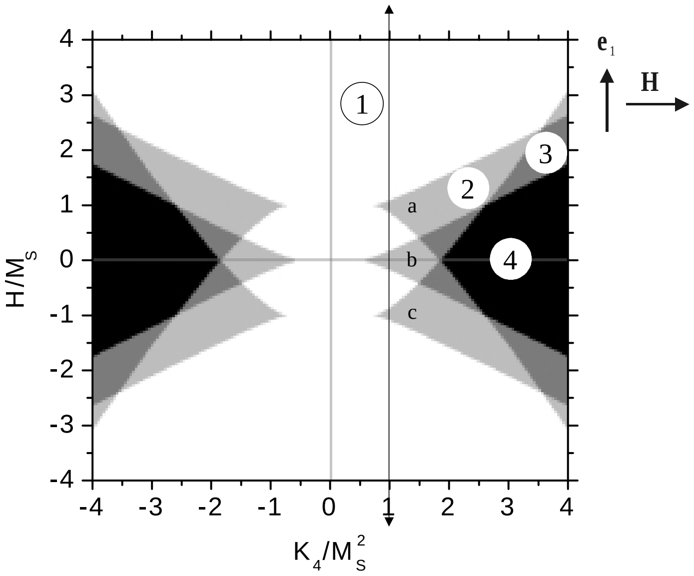

Fig. 4: Phase diagram of a system with fixed unidirectional anisotropy $K_1/M_S^2 = 1$ and variable fourfold anisotropy K_4 with the field aligned perpendicular to the easy direction of the unidirectional anisotropy. The phases with one, two, three and four minima in the free enthalpy are labeled 1, 2, 3 and 4 accordingly. The position of the magnetization reversal given in Fig. 3 is indicated by a double arrow. The different parts of phase 2 crossed during this reversal are labeled a,b and c.

and two minima as follows. A new minimum appears in the region labeled “a” as the magnetic field is lowered after saturation in positive field. The enthalpy minimum g_2, in which according to the perfect delay convention the magnetization is in, becomes unstable when leaving region “a”, giving rise to the first discontinuous change in the magnetization shown in Fig. 3.

If the magnetic field is lowered further, the magnetization rotates and a new energy minimum appears in region “b”. This new minimum is at an energy higher than the state the magnetization is in and cannot therefore be accessed unless the energy of the magnetic system is increased. The configuration again becomes unstable as the field is changed and the system leaves region “c”. This appears as a second discontinuous change in Fig. 3. Because of symmetry, the system follows the same evolution in reverse as the field is increased from negative saturation.

The concept of phase diagrams can be easily extended to include further anisotropies like uniaxial or tridirectional contributions. Furthermore the dependence of the system properties on the in-plane angle of the applied magnetic field can be easily evaluated [4].

T.M. acknowledges support by the Studienstiftung des Deutschen Volkes.

References

[1] Y.T. Millev, H.P. Oepen, J. Kirschner, Phys. Rev. B, **57**, 5837 (1998).
[2] Y.T. Millev, H.P. Oepen, J. Kirschner, Phys. Rev. B, **57**, 5848 (1998).
[3] S. Nieber, H. Kronmüller, phys. stat. sol. (b) **165**, 503 (1991).
[4] T. Mewes, H. Nembach, J. Fassbender, B. Hillebrands, J.V. Kim, R.L. Stamps, submitted to Phys. Rev. B.
[5] T. Mewes, H. Nembach, M. Rickart, S.O. Demokritov, J. Fassbender, B. Hillebrands, Phys. Rev. B **65**, 224423 (2002).
[6] H. Xi, M.H. Kryder, R.M. White, Appl. Phys. Lett. **74**, 2687 (1999).

6.13 Influence of thermal activation on the exchange bias effect

T. Mewes, H. Nembach, J. Fassbender, and B. Hillebrands[1]

As discussed in Chapter 6.12, the evolution of the magnetization under the so-called perfect delay convention assumes that the magnetization remains in a metastable state as long as there is an energy barrier present separating the local enthalpy minimum from other enthalpy minima corresponding to other, possibly lower, enthalpy configurations. Thermal fluctuations are one way in which the magnetic system can change from one such minimum to another [1].

The stability of the system in the local minimum of the free enthalpy $g_{local,min}$ can be examined by calculating the barrier height $e_{1,2}(H) = g_{max1,2} - g_{local,min}$ where $g_{max1,2}$ are the adjacent maxima in the free enthalpy relative to the local enthalpy minimum. The distribution of thermal fluctuations below the ordering temperature is assumed to obey Boltzmann statistics, so that it is more likely within a given time interval for the system to hop over a barrier from a high enthalpy state to a low enthalpy state than it is for the reverse process to occur and to increase the system enthalpy. As such, we focus our discussion on thermal processes that lower the system enthalpy and define the energy barrier as the minimum barrier taking the system from one configuration to another: $e(H) = \min(e_1(H), e_2(H))$.

In the following a system with a unidirectional anisotropy $K_1 = 4.6 \cdot 10^4\,\mathrm{erg/cm^3}$ and a fourfold anisotropy $K_4 = 3.8 \cdot 10^4\,\mathrm{erg/cm^3}$ is investigated. This represents an epitaxial exchange coupled $\mathrm{Ni_{81}Fe_{19}/Fe_{50}Mn_{50}(001)}$ bilayer with values determined by fits to experimental data [2], see Fig. 1.

As long as the magnetic field is applied along a high symmetry direction, for example $\alpha_H = 0°, 90°, 180°, \ldots$, due to the symmetry of the problem the barrier height is the same for the increasing and decreasing field branch of the magnetization reversal with respect to the exchange

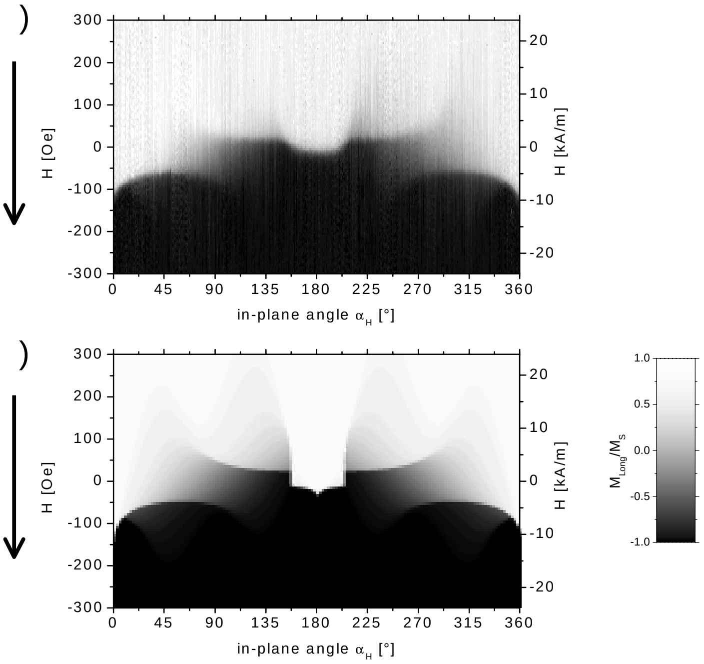

Fig. 1: Reversal diagram for the longitudinal component of the magnetization for the decreasing field branch a) as measured for an epitaxial NiFe/FeMn bilayer system [2] and b) simulation for $K_1 = 4.6 \cdot 10^4\,\mathrm{erg/cm^3}$ and $K_4 = 3.8 \cdot 10^4\,\mathrm{erg/cm^3}$. White corresponds to parallel alignment of the magnetization with respect to the positive field direction and black to antiparallel alignment. As indicated by the black arrow on the left, only the decreasing field branch is shown.

---

[1] In collaboration with J.V. Kim and R.L. Stamps, University of Western Australia, Perth, Australia.

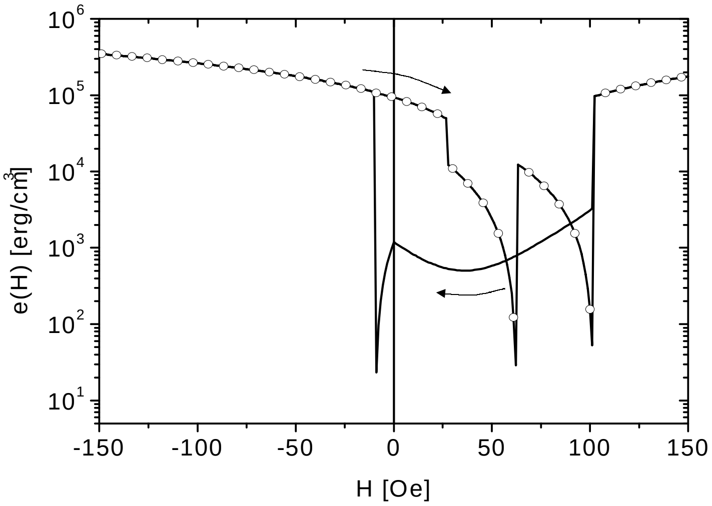

Fig. 2: Barrier height $e(H)$ for $\alpha_H = 160°$. Open symbols correspond to an increasing and the line corresponds to a decreasing field, as also indicated by the arrows.

bias field. This is no longer true if the field is applied in a direction that is not collinear with respect to the easy direction of the unidirectional anisotropy as shown in Fig. 2 for $\alpha_H = 160°$. As the barrier height covers a wide range of energy densities it is shown on a logarithmic scale.

In this case the barrier height becomes asymmetric for both branches of the magnetization reversal in that the barrier height is different when the field is increased from negative saturation compared to the situation when the field is decreased from positive saturation. Therefore any process that is sensitive to the barrier height will become asymmetric in this sense. This has been discussed in the context of time and temperature dependent processes by several authors [3–5], and may be related to the domain orientation asymmetry observed during the magnetization reversal [6–8].

Following Street and Woolley [1], the probability for a thermally activated lowering of the system enthalpy depends on the time interval Δt and the barrier energy E_B according to

$$P(\Delta t) \sim 1 - \exp\left(-\frac{\Delta t}{\tau}\exp(-E_B/k_B T)\right) \quad , \tag{1}$$

where $1/\tau$ denotes the attempt frequency. We approximate this with a heavyside step function $P(\Delta t) = \Theta(k_B T - E_B)$ under the assumption that $\frac{\Delta t}{\tau}$ is small and that $k_B T$ is not too large compared to E_B. This means that all processes associated with energy barriers below a certain cut-off defined by $k_B T$ occur. Such an approximation provides a crude picture of what one might expect for very narrow energy barrier distributions and quasi-static hysteresis loop measurements.

The idea is that if the temperature is low, there are only few possibilities for the system to spontaneously switch from one configuration to a lower enthalpy configuration. This will occur whenever one of the barrier heights $e_1(H)$ or $e_2(H)$ separating the local minimum from the adjacent ones is less than a given thermal energy density e_{therm}. In Fig. 3(a-c) the angular dependence of the magnetization reversal for temperatures corresponding to $e_{therm} = 1000,\ 1300$ and $1700\,\mathrm{erg/cm^3}$ are shown. In comparison with the case without thermal activation the sharp edges are rounded out with increasing temperature resulting in a better agreement between simulation and experiment. Especially the structure at $\alpha_H = 180°$ that is present in the calculation without thermal activation shown in Fig. 1 (lower panel) but not in the experiment of Fig. 1 (upper panel) vanishes when thermal activation is included, as can be seen in Fig. 3. The peak at $\alpha_H = 0°$ is still present and is only reduced in size – as observed in the experiment. As all experiments were taken at 293 K, from the measurements a rough estimation of the activation volume V can be made for

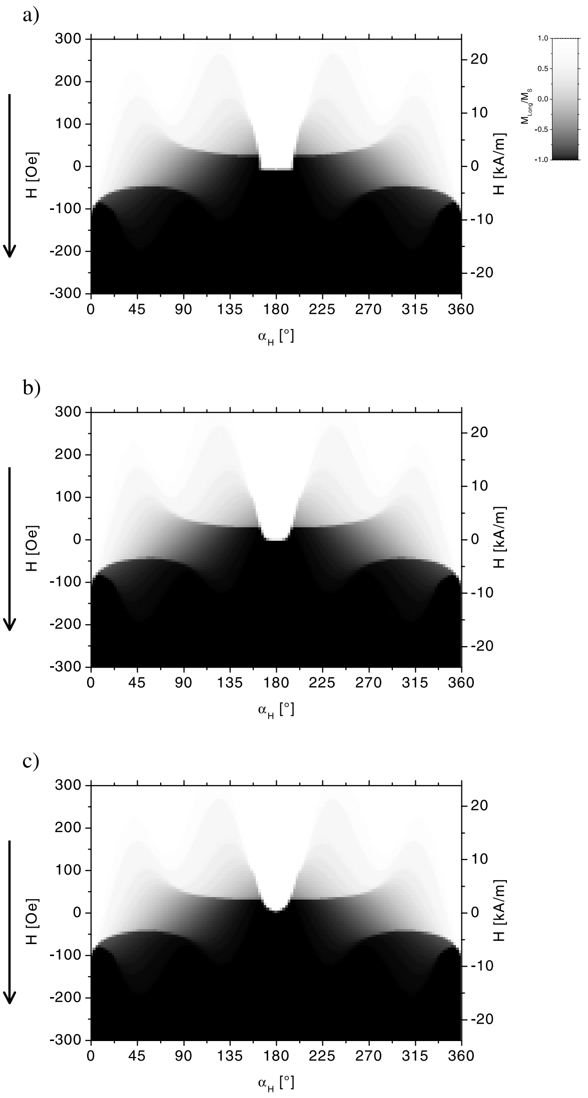

Fig. 3: Simulation of the longitudinal component of the magnetization for the decreasing field branch (indicated by the black arrow on the left) of the magnetization reversal for a system with $K_1 = 4.6 \cdot 10^4\,\mathrm{erg/cm^3}$ and $K_4 = 3.8 \cdot 10^4\,\mathrm{erg/cm^3}$ including thermal activation and a) $e_{therm} = 1000\,\mathrm{erg/cm^3}$, b) $e_{therm} = 1300\ \mathrm{erg/cm^3}$ and c) $e_{therm} = 1700\,\mathrm{erg/cm^3}$.

$e_{therm} = kT/V \approx 1300\,\mathrm{erg/cm^3}$. This results in an activation volume of $2.3 \cdot 10^{-23}\,\mathrm{m^3}$, which corresponds to a cylinder with a radius $r \approx 40\,\mathrm{nm}$. This is of the same order as the exchange length and is therefore consistent with the Stoner like thermal switching process assumed for these estimates of thermal activation.

T.M. acknowledges support by the Studienstiftung des Deutschen Volkes.

References

[1] R. Street, J.C. Woolley, Proc. Phys. Soc. London **62**, 562 (1949).
[2] T. Mewes, H. Nembach, M. Rickart, S.O. Demokritov, J. Fassbender, B. Hillebrands, Phys. Rev. B **65**, 224423 (2002).
[3] E. Fulcomer, S.H. Charap, J. Appl. Phys **43**, 4190 (1972).
[4] R.L. Stamps, Phys. Rev. B **61**, 12174 (2000).
[5] A.M. Goodman, K. O'Grady, M.R. Parker, S. Burkett, J. Magn. Magn. Mater. **193**, 504 (1999).
[6] M.R. Fitzsimmons, P. Yashar, C. Leighton, I.K. Schuller, J. Nogues, C.F. Majkrzak, J.A. Dura, Phys. Rev. Lett. **84**, 3986 (2000).
[7] C. Leighton, M. Song, J. Nogues, M.C. Cyrille, I.K. Schuller, J. Appl. Phys. **88**, 344 (2000).
[8] I.N. Krivorotov, C. Leighton, J. Nogues, I.K. Schuller, E. Dan Dahlberg, Phys. Rev. B **65**, 100402(R) (2002).

D. Elastic Properties

6.14 Brillouin light scattering study on nanoporous low dielectric constant films

T. Wittkowski, K. Jung, and B. Hillebrands[1]

Thin porous films with nanometer pore sizes are subject of intense interest, primarily because of their reduced dielectric constant. The lack of useful characterization tools and the reduction in film mechanical properties with increasing porosity have severely hindered their development and application. Brillouin light scattering provides valuable and new information about the mechanical and other film properties.

The films consist of nanoporous methylsilsesquioxane (MSSQ). Initially composed of a mixture of a thermally stable oligomer and a thermally unstable organic porogen polymer, the porogen diffuses out during heating, leaving voids, and the remaining inorganic matrix vitrifies and leaves a nanoporous structure with reduced dielectric constant [1]. Films with porosities ranging from 16 to 39 % have been investigated where the porosity p is defined in units of % as

$$p = \frac{\rho_{matrix} - \rho_{film}}{\rho_{matrix}} \times 100 \quad . \tag{1}$$

Brillouin spectra were recorded in ($p \rightarrow ps$) 180°-backscattering geometry with a low light power (approx. 10 mW) on the sample. Acoustic surface and bulk excitations were observed at room temperature with an average acquisition time of 1 hour per spectrum. The longitudinal acoustic bulk mode (LA) did not show a significant angular dispersion so that the films behave elastically isotropic. From the phase velocities v_R and v_L of the two independent acoustic excitations, namely the Rayleigh mode and the LA mode, the two independent stiffness constants c_{11} and c_{12} of the film material were deduced, leading to the precise determination of the Poisson's ratio $\nu = 0.26 \pm 0.01$. Assuming that ν changes little with the density, the Young's modulus E for each film is obtained from $E = \rho v_L^2 (1+\nu)(1-2\nu)/(1-\nu)$. Figure 1 shows Brillouin spectra of the 16 % porosity sample.

The variation of the Young's modulus as a function of porosity was determined with two independent experimental methods, Brillouin light scattering (BLS) and surface acoustic waves spectroscopy (SAWS). The latter technique detects the frequency dependent runtime of wide band surface acoustic wave packets generated by a laser pulse. The velocity dispersion of the Rayleigh wave is fitted in order to obtain E and ρ. Figure 2 shows a comparison of the results.

The values from both techniques are, at most, ≈ 20 % different. Considering that the values for the Young's modulus are derived using BLS at approximately 8 GHz from the longitudinal mode, and using SAWS at approximately 100 MHz from a primarily transverse mode, this can be considered as an excellent verification of the E values extracted from both techniques [2]. The unusually low

---

[1] In collaboration with C.M. Flannery, Paul-Drude-Institut für Festkörperelektronik, FG Nanoakustik, Hausvogteiplatz 5-7, D-10117 Berlin, Germany, M.R. Baklanov, XPEQT at IMEC, B-3001 Leuven, Belgium, L. Giovannini, Istituto Nazionale per la Fisica della Materia (INFM) and Dipartimento di Fisica, Universitá di Ferrara, Via Paradiso 12, I-44100 Ferrara, Italy.

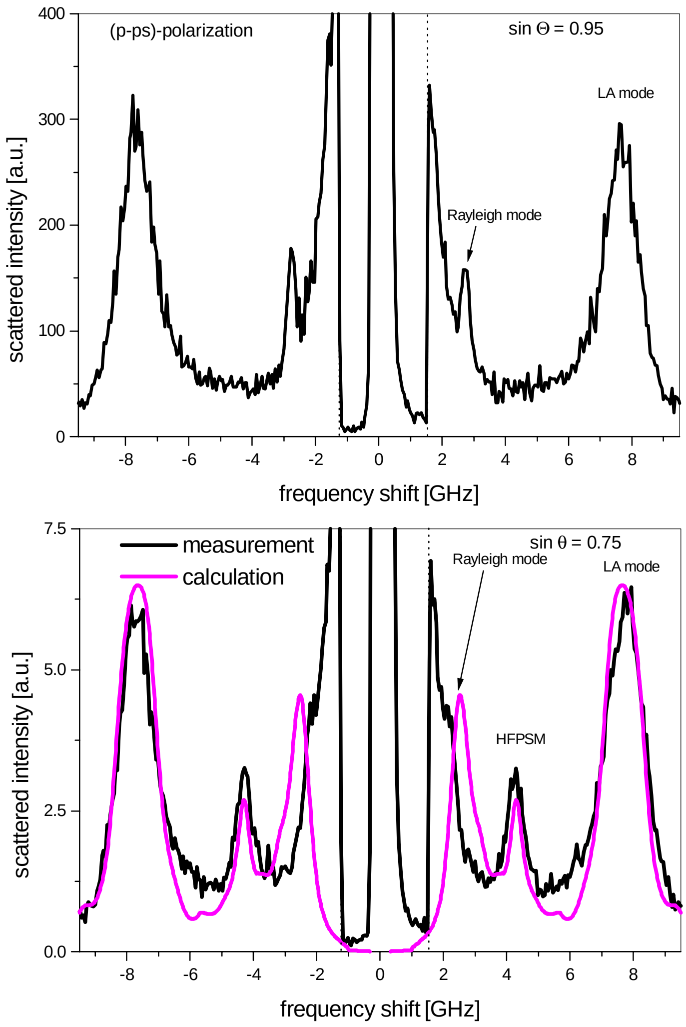

Fig. 1: Brillouin spectra of the 16 % porosity sample for two polar angles of light incidence θ. In addition to the Rayleigh mode a surface resonance, the high-frequency pseudo-surface mode (HFPSM) is detected. Since the refractive index n is known with high accuracy the frequency information of the HFPSM and the LA mode is redundant. However, the scattered intensities of all acoustic excitations may be used to determine the elasto-optic constants of the film material. The lower diagram shows the measured spectrum in combination with the best fitting computed spectrum (grey lines). The deduced isotropic elasto-optic constants are $k_{11} = 0.12$, $k_{12} = -0.93$ and $k_{44} = 0.525$. The underlying parameters are $\rho = 1.178\,\mathrm{g/cm^3}$, $c_{11} = 2.51\,\mathrm{GPa}$ and $c_{12} = 0.86\,\mathrm{GPa}$. From ellipsometric investigation on MSSQ the complex dielectric constant was found to be $\varepsilon_{\mathrm{MSSQ}} = 1.88 + \imath \cdot 0$. For silicon the value $\varepsilon_{\mathrm{Si}} = 18.5 + \imath \cdot 0.52$ was used.

rate of modulus decline (close to linear dependence on porosity) is in contrast to that observed for nanoporous silica where the stiffness decreases with a fourth power.

The Brillouin cross section has been calculated according to the theory of Ref. [3], properly taking into account the optical properties of the sample. It depends on two scattering mechanisms: the ripple contribution, due to the undulation of the free surface and the interface, and the elasto-optic contribution, due to the modulation of the dielectric tensor through the elasto-optic coupling constants. Exploiting the different scattering properties of modes of different nature, we have been able to determine the full set of elasto-optic constants of MSSQ. It is assumed that its elasto-optic tensor k is real and possesses isotropic symmetry; therefore it contains two independent components only. The ripple contribution to the peaks of the LA and the high-frequency pseudo-surface mode (HFPSM) is negligible and the cross section ratio between these two modes depends on the ratio k_{11}/k_{12} with k_{44}/k_{12} given by the isotropy condition. The value of k_{12} is then determined by measuring the cross section ratio of the Rayleigh and the LA mode, since the cross section for the Rayleigh wave depends almost only on the ripple effect. By fitting the experimental spectra with the calculated cross section we found the values $k_{11} = 0.12$, $k_{12} = -0.93$ and $k_{44} = 0.525$. A calculated spectrum has been plotted in Fig. 1 and a comparison with the experimental data shows good agreement.

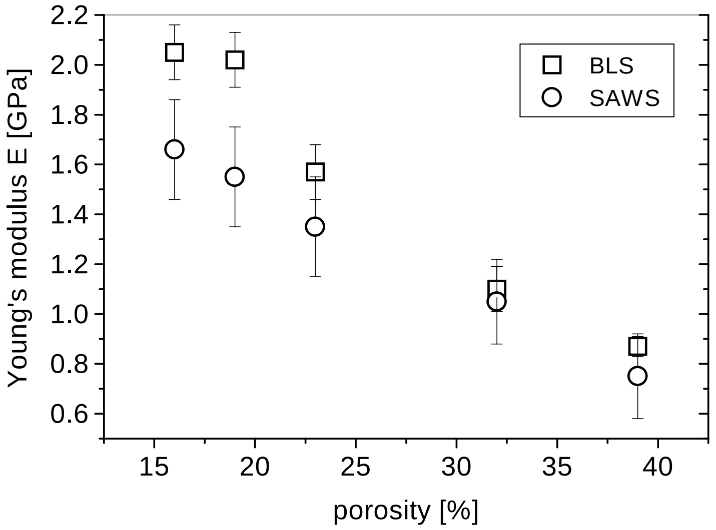

Fig. 2: Young's modulus derived from Brillouin light scattering and SAWS as a function of the film porosity. They are in good agreement with each other and show a linear porosity dependence in this range of porosity.

The investigations demonstrate that Brillouin light scattering in combination with complementary analytical methods provides access to several relevant film properties. Today it is clear that introducing porosity in thin films alters many aspects of their physical behavior. Brillouin light scattering has been shown to be an extremely useful tool for controlling and optimising properties of this type of films.

Support by the Deutsche Forschungsgemeinschaft is gratefully acknowledged.

References

[1] C.J. Hawker, J.L. Hedrick, R.D. Miller, W. Volksen, MRS Bull. **25**, 54 (2000).
[2] C.M. Flannery, T. Wittkowski, K. Jung, B. Hillebrands, M.R. Baklanov, Appl. Phys. Lett. **80**, 4594 (2002).
[3] V. Bortolani, A. Marvin, F. Nizzoli, G. Santoro, J. Phys. C: Solid St. Phys. **16**, 1607 (1980).

6.15 Surface phonons in stepped hard films

T. Wittkowski, G. Distler, K. Jung, and B. Hillebrands

The Brillouin light scattering analysis of stepped films opens up new possibilities for the determination of the stiffness tensor, and it allows the reliable proof of the variation of microstructure as a function of the distance from the interface as well as its quantitative description. An alteration of microstructure with growing film thickness is a frequently observed phenomenon, especially for hard coatings. Prominent examples are boron nitride coatings [1]. Investigations of amorphous carbon films also clearly document such a behavior [2].

Our earlier work indicated that it would be useful to study films of several thicknesses on a common substrate. For this purpose we have modified our sputtering apparatus so that the substrate can be moved behind a shielding window. This technique allows the preparation of stepped films with steps typically 1 mm wide.

Stepped tungsten carbide films were deposited on silicon by magnetron sputtering of a WC target and simultaneous ion plating. Special care was given to precisely fix the electrical potentials in the vicinity of the silicon substrate in order to achieve constant particle flux and energy which are homogeneous over the sample area for the complete deposition run. This preparation technique consequently avoids typical sources of error which may occur when depositing several single films of different thickness. In our experiment the energy of the plating Ar ions was varied between 30 eV and 145 eV. For the flux ratio of plating particles and film building particles we used $\Phi_{\mathrm{Ar}^+}/(\Phi_{\mathrm{W}}+\Phi_{\mathrm{C}}) = 1.8$. From earlier investigations it is well known that the microstructure of WC films depends critically on the fluences and energies in this parameter range [3].

Figure 1 shows a Brillouin spectrum of a stepped WC film deposited with an ion energy of 30 eV. Due to the high mass density of the film material up to seven discrete surface acoustic modes were detected.

Figure 2 shows the dispersion in a stepped WC film which was deposited with an ion energy of 30 eV. The rich data base permits the determination of four independent components of the stiffness tensor as well as the mass density. The film possesses a high stiffness and hardness but cannot be considered superhard ($\mathrm{H_V} > 40$ GPa). As is deduced from the elastic constants the WC films material behaves almost elastically isotropic.

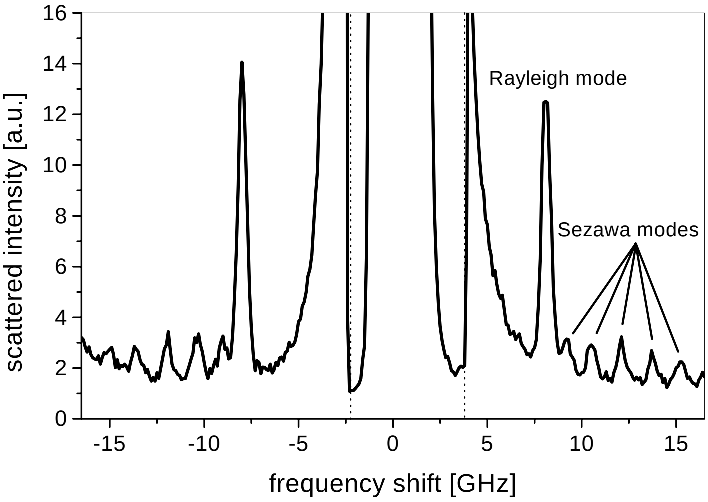

Fig. 1: Brillouin spectrum of the 600 nm thick step of a stepped WC film, deposited with an ion energy of 30 eV. Clearly visible on the Stokes and on the anti-Stokes side of the spectrum are the Rayleigh mode and five Sezawa modes in the discrete part of the spectrum. Spectra were taken in $(p \to ps)$-polarisation; for the spectrum shown, the angle of incidence was 45°. A slit aperture was used in order to reduce the sagittal wave vector interval.

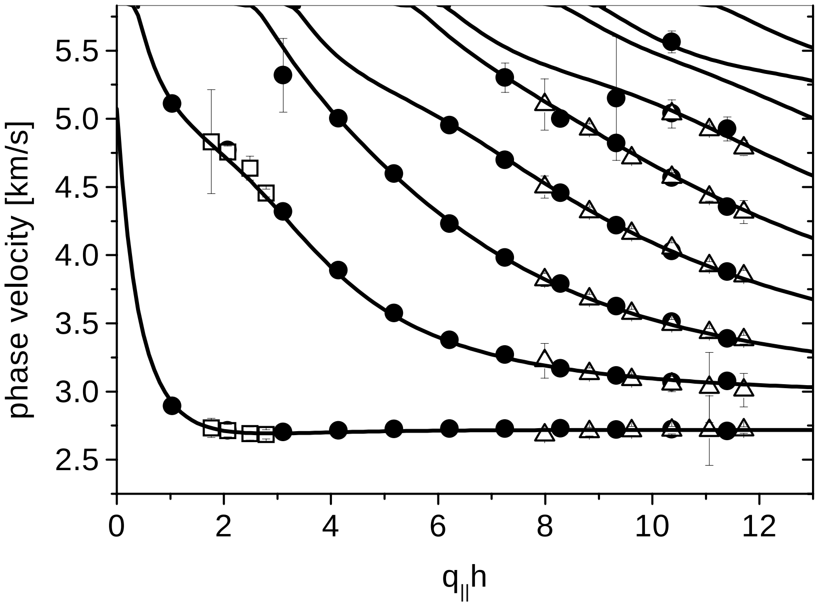

Fig. 2: Phase velocities of the discrete sagittal surface phonons in a stepped tungsten carbide film. Measurements have been taken as a function of film thickness for constant phonon wave vector of 17.27 µm^{-1} (full symbols). On two steps of different thickness the phonon wave vector was varied additionally (open symbols). Both measurement techniques yield identical phase velocities. Lines were calculated with the stiffness constants of the film material, $c_{11} = 350.2$ GPa, $c_{13} = 128.9$ GPa, $c_{33} = 354.2$ GPa, $c_{55} = 113.7$ GPa, and the mass density $\rho = 13.0\,\mathrm{g/cm^3}$. These constants were obtained in a least squares fit of the experimental data.

A Brillouin light scattering analysis of stepped films provides the benefit of an easy way to independently vary the thickness h and the parallel phonon wave vector $q_{\parallel}$. In case that the film material does not alter its microstructure with increasing thickness the dispersion of surface modes depends solely on the product of both quantities. Variations in microstructure can thus be detected by varying both quantities independently. If the sound velocities for identical values of $q_{\parallel}h$ coincide, the microstructure will be homogeneous over the thickness. This is exactly the finding of the wave vector variation at the 120 nm and 600 nm thick steps of the low energy WC film, as shown in Fig. 2.

The influence of changes in the crystallographic phase, involved stoichiometry and density alterations, and the effects of growth structure and film texture on the effective elastic behavior can be analysed in detail at a single sample due to the obviously increased data base for stepped film deposition. Brillouin experiments have evidenced that increasing ion energy during film deposition is accompanied by a distinct change of the effective stiffness constants and leads to a pronounced elastic anisotropy. These results are correlated with Auger electron spectroscopy and X-ray diffraction data and lead to a deepened understanding of the growth mechanisms and the microstructure of these films which are highly relevant for technical applications.

Support by the Deutsche Forschungsgemeinschaft is gratefully acknowledged.

References

[1] T. Wittkowski, P. Cortina, J. Jorzick, K. Jung, B. Hillebrands, Diam. Rel. Mat. **368**, 216 (2000).
[2] T. Wittkowski, V. Wiehn, J. Jorzick, K. Jung, B. Hillebrands, Thin Solid Films **9**, 1957 (2000).
[3] G. Keller, I. Barzen, W. Dötter, R. Erz, S. Ulrich, K. Jung, H. Ehrhardt, Mat. Sci. Eng. A **139**, 137 (1991).

E. Transfer of Technology

6.16 Antiadhesive coatings on coextrusion dies for EVOH containing blend resin

L. Kleinen, K. Jung, and B. Hillebrands[1]

The work in the Institute for Thin Film Technology is aimed at the development of hard coatings for special applications in small and medium sized companies.

Thin films of amorphous carbon modifications (DLC, ta-C, a-C and a-C:H) and several ceramic materials like WC, TiN, TiAlN, SiC and CrN have been developed for a variety of industrial applications especially in the biomedical field. Starting from the requirement for many biocompatible thin films to be either hydrophilic or hydrophobic we developed coatings with large variations in their surface potential. Beyond the biomedical applications those surfaces are suitable to solve many adhesion related problems in other fields like polymer processing.

Manufacturers of plastic fuel tanks for the automotive industry have to follow several national statutory requirements regarding regulations for environment, safety and health. State of the art solutions are multilayer tanks containing polyethylene vinyl alcohol copolymers (EVOH) as a gasoline diffusion barrier. These tanks are produced by coextrusion blow moulding, sandwiching EVOH between several other polymer layers, one layer containing so called ‘coex blend resin’

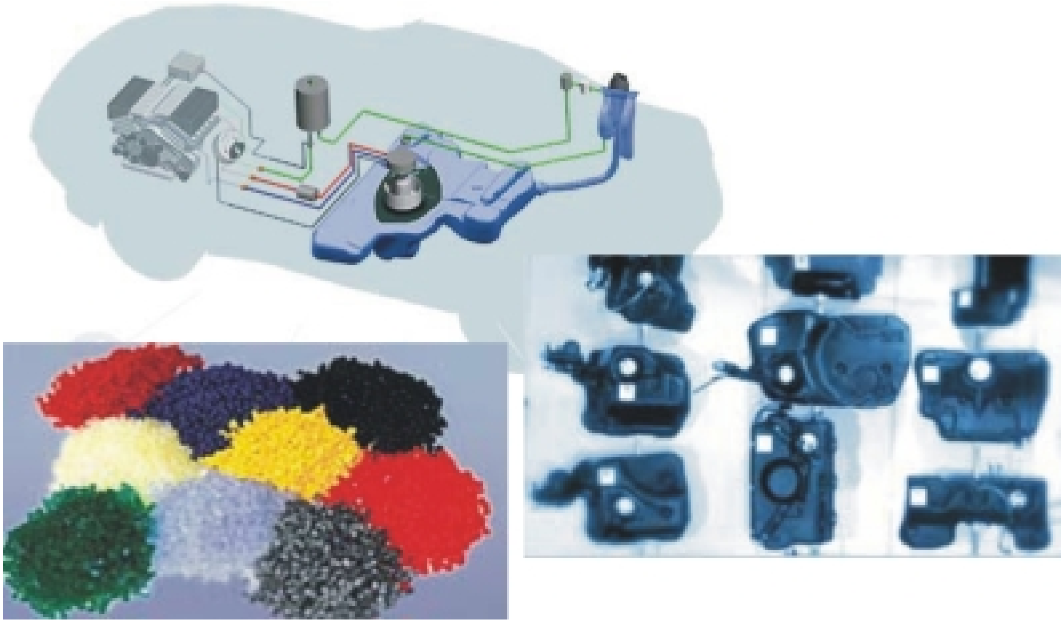

Fig. 1: Plastic fuel tanks for the automotive industry developed and produced by Kautex Textron (Bonn). Shredded plastics are molten and pressed into various forms of tanks by blow extrusion. Part of the multilayered tanks consist of recycled old tanks, a material which is difficult to process.

---

[1] In collaboration with H. Busch, U. Grabowy, NTTF GmbH, Rheinbreitbach and Kautex Textron GmbH & Co. KG, Bonn.

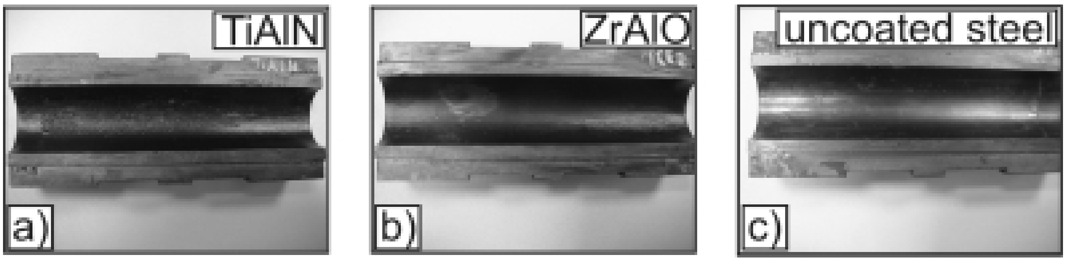

Fig. 2: Colored EVOH debris on coated (a,b) and uncoated (c) test tools after the coextrusion process. The debris was removed and weighted. The coating shall provide a surface that is mostly EVOH repellent and from which the debris can be removed without much effort. The ZrAlO coating (b) showed the best test results. Although there is slightly more EVOH on this surface than on the uncoated steel surfaces ist can be more easily removed.

(shredded plastics from recycled tanks). The EVOH component of this blend resin tends to stick to the walls of the extrusion dies and has to be mechanically removed after several hours of operation time.

Fig. 3: Determination of surface energy by sessile drop contact angle measurement. The measured contact angle θ is the angle between the drop base line and the tangent to the drop profile in the three phase point as shown in the left figure (γ_l is the surface tension of the liquid, γ_s is the surface tension of the solid). The right three pictures show water drops on different solid surfaces varying in their surface energy from hydrophilic to hydrophobic (left to right). Taken from [1, 2].

To ensure less downtime the adhesion of EVOH to the walls of the extrusion dies must be reduced. We approached the problem by coating parts of an extrusion test facility with thin films of different surface energy. Considering that EVOH is the only polar component in the blend resin, the adhesion should be diminished by a surface with a low polar component of surface energy. The test tools were coated with a-C:H/Si, ZrAlO, CrN, WCC, SiC, TiN and TiC. After four hour operation time in the test facility the EVOH debris on the tool walls was made visible with red food coloring (Fig. 2), removed with a copper brush and weighted.

			contact angle [°]		surface energy [mJ/m^2]		
sample		surface	water	diiodomethane	total	disperse	polar
01	HS 03	ZrAlO	72.1	52.2	39.0	27.9	11.1
02	HS 12	a-C:H/Si	80.1	49.6	37.3	31.0	6.2
03	HS 13	CrN	68.8	53.9	40.0	26.4	13.6
04	HS 13	WCC	69.1	44.9	42.3	31.6	11.4
05	HS 15	SiC	44.7	36.4	58.2	32.4	25.9
06	HS 15	TiN	51.5	33.6	55.2	34.6	20.6
07	HS 12	TiC	41.2	47.6	58.0	26.4	31.6
08	HS 22	steel	34.8	56.5	60.5	21.0	39.5

Table 1: Method: sessile drop / Owens-Wendt-Rabel and Kaelble.

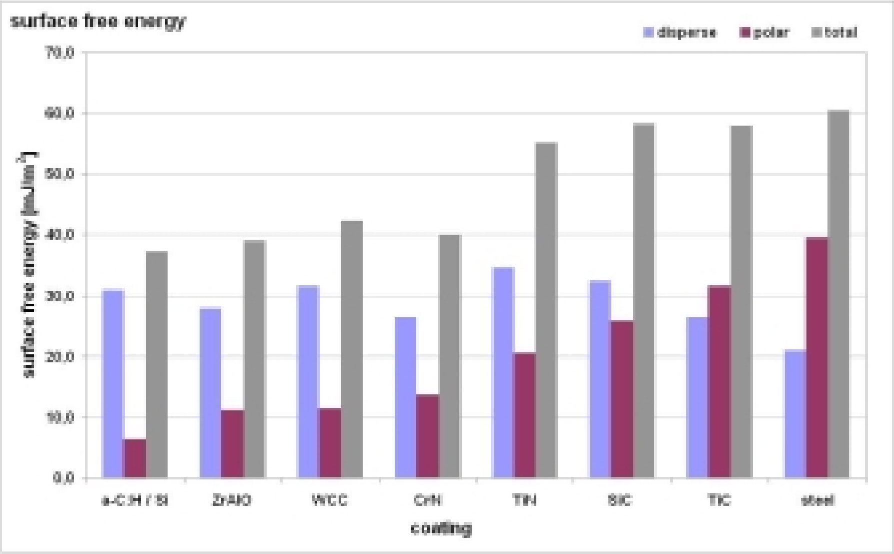

Fig. 4: Polar and disperse parts of the surface energy of seven coatings and uncoated steel. The polar part is assumed to be responsible for the EVOH adhesion and increases from left to right.

The test runs were repeated at least three times with each coated tool using uncoated steel as a reference. Afterwards the disperse and polar parts of the surface free energies of the coatings were determined by optical contact angle (OCA) measurement using an OCA 15 (Dataphysics), the sessile drop method and the Owens-Wendt-Rabel and Kaelble evaluation. A small amount of liquid is dispensed onto the surface. The sessile drop is illuminated from one side with a diffuse light source. From the other side the contour of the drop is observed with a CCD camera [2] and the contact angle is determined by fitting the drop profile. The results of the OCA measurement, which was performed with two liquids of different polar surface tensions (water and diiodomethane) are listed in Tab. 1 and shown in Fig. 4.

The polar part of the surface energy increases from $6\,\mathrm{mJ/cm^2}$ for a-C:H/Si to $40\,\mathrm{mJ/cm^2}$ for uncoated steel. The ZrAlO coating showed the best anti-adhesion results in the test facility although the polar surface energy of $11\,\mathrm{mJ/cm^2}$ is slightly higher than that of the Si doped amorphous carbon coating. But taking into account the different surface roughnesses of the tools this result can be equivocal. Further examinations have to proof the correlation between the EVOH adhesion and the polar surface energy more precisely.

Supported by the Stiftung Rheinland-Pfalz für Innovation is gratefully acknowledged.

References

[1] L. Makkonen, Langmuir **16**, 7669 (2000).
[2] DataPhysics Instruments GmbH, Filderstadt, operation manual.

Chapter 7: Publications

Most publications can be downloaded from http://www.physik.uni-kl.de/hillebrands.

7.1 published

1. *Temperature dependence of interlayer coupling in Fe/Cr superlattices - FMR studies*
   A.B. Drovosekov, D.I. Kholin, N.M. Kreines, O.V. Zhotikova, S.O. Demokritov
   J. Magn. Magn. Mater. **226**,1779 (2001).

2. *Morphology of epitaxial metallic layers on MgO substrates: influence of submonolayer carbon contamination*
   M. Rickart, B.F.P. Roos, T. Mewes, J. Jorzick, S.O. Demokritov, B. Hillebrands
   Surf. Sci. **495**, 68 (2001).

3. *Elastic properties of indium tin oxide films*
   T. Wittkowski, J. Jorzick, H. Seitz, B. Schröder, K. Jung, B. Hillebrands
   Thin Solid Films **398**, 465 (2001).

4. *Switching dynamics and write endurance of magnetic tunnel junctions*
   M. Bauer, R. Lopusnik, J. Fassbender, B. Hillebrands, J. Bangert, J. Wecker
   J. Appl. Phys. **91**, 543 (2002).

5. *Magnetization reversal of exchange bias double layers magnetically patterned by ion irradiation*
   J. Fassbender, S. Poppe, T. Mewes, A. Mougin, B. Hillebrands, D. Engel, M. Jung, A. Ehresmann, H. Schmoranzer, G. Faini, K.J. Kirk, J.N. Chapman
   Phys. Stat. Sol. (a) **189**, 439 (2002).

6. *Auger electron spectroscopy studies of annealing effects on Al/Fe, Al/FeO/Fe and Al/CoO/Co interfaces*
   B.F.P. Roos, P.A. Beck, S.O. Demokritov, B. Hillebrands
   Surf. Sci. Lett. **497**, L55 (2002).

7. *Brillouin light scattering study on the elastic properties of thick sputtered c-BN films*
   T. Wittkowski, J. Jorzick, K. Jung, B. Hillebrands, M. Keunecke and K. Bewilogua
   J. Appl. Phys. **91**, 2729 (2002).

8. *Spin wave wells in nonellipsoidal micrometer size magnetic elements*
   J. Jorzick, S.O. Demokritov, B. Hillebrands, D. Berkov, N.L. Gorn, K. Guslienko, A.N. Slavin
   Phys. Rev. Lett. **88**, 047204 (2002).

9. *Tuning exchange bias and coercive fields in ferromagnet/antiferromagnet bilayers with ion irradiation*
   J. Juraszek, J. Fassbender, S. Poppe, T. Mewes, B. Hillebrands, D. Engel, A. Kronenberger, A. Ehresmann, H. Schmoranzer
   J. Appl. Phys. **91**, 6896 (2002).

10. *Critical properties of nanoporous low dielectric constant films revealed by Brillouin light scattering and surface acoustic wave spectroscopy*
    C.M. Flannery, T. Wittkowski, K. Jung, B. Hillebrands
    Appl. Phys. Lett. **80**, 4594 (2002).

11. *Strength-porosity relationship of nanoporous MSSQ films characterised by Brillouin light scattering and surface acoustic wave spectroscopy*
    C.M. Flannery, T. Wittkowski, K. Jung, B. Hillebrands, M.R. Baklanov
    Proc. MRS Spring meeting, San Francisco **716**, B7.17 1-6 (2002).

12. *Angular dependence and phase diagrams of exchange coupled epitaxial* $Ni_{81}Fe_{19}/Fe_{50}Mn_{50}$ *(001) bilayers*
    T. Mewes, H. Nembach, M. Rickart, S.O. Demokritov, J. Fassbender, B. Hillebrands
    Phys. Rev. B **65**, 224423 (2002).

13. *Ultrafast magnetic switching*
    B. Hillebrands, J. Fassbender
    Nature **418**, 493 (2002).

14. *Non-monotone magnetic anisotropy of bcc Fe-films grown on vicinal fcc Au-substrates*
    M. Rickart, S.O. Demokritov, B. Hillebrands
    J. Phys.: Condens. Matter **14**, 8947 (2002).

15. *Dynamic “pinning” of dipolar origin in nonellipsoidal magnetic stripes*
    K. Yu. Guslienko, S.O. Demokritov, B. Hillebrands, A.N. Slavin
    Phys. Rev. B. **66**, 132402 (2002).

16. *Morphology of epitaxial metallic layers on MgO substrates: influence of submonolayer carbon contamination*
    M. Bailleul, D. Olligs, C. Fermon, S.O. Demokritov, B. Hillebrands
    Europhys. Lett. **56**, 741 (2001).

17. *Domain observation on Fe-Cr-Fe layered structures & Evidence for a biquadratic coupling effect*
    M. Rührig, R. Schäfer, A. Hubert, R. Mosler, J.A. Wolf, S. Demokritov, P. Grünberg
    Phys. Stat. Sol., Special Issue: 40 Years of physica status solidi (1961-2001), 297 (2001).

7.2 in press

1. *Spindynamics in confined magnetic structures II*,
   B. Hillebrands, K. Ounadjela (Eds)
   Springer, Berlin (2003).

2. *Magnetization dynamics investigated by time-resolved Kerr effect magnetometry*
   J. Fassbender
   in: *Spin dynamics in confined magnetic structures II*, Eds. B. Hillebrands, K. Ounadjela
   Springer, Berlin

3. *Confined dynamic excitations in structured magnetic media*
   S.O. Demokritov, B. Hillebrands, A.N. Slavin
   IEEE Trans. Magn.

4. *Temperature dependence of interlayer coupling in a Fe/Cr/Fe wedge sample, MOKE and MBLS studies*
   S. O. Demokritov, A.B. Drovosekov, D.I. Kholin, N.M. Kreines
   IEEE Trans. Magn.

5. *Temperature dependence of interlayer coupling in Fe/Cr/Fe layered systems*
   S.O. Demokritov, A.B. Drovosekov, N.M. Kreines, H. Nembach, M. Rickart, D.J. Kholin
   Sov. Phys. JETP.

6. *Collison properties of quasi-one-dimensional spin wave solitons and two-dimensional spin wave bullets*
   A.N. Slavin, O. Büttner, M. Bauer, S.O. Demokritov, B. Hillebrands, M.P. Kostylev,
   B.A. Kalinikos, V.V. Grimalsky, Yu. Rapoport
   Chaos

7. *Coherent precessional magnetization reversal in microscopic magnetic memory elements*
   H.W. Schumacher, C. Chappert, P. Crozat, R.C. Sousa, P.P. Freitas, J. Miltat, J. Fassbender, B. Hillebrands
   Phys. Rev. Lett.

7.3 submitted

1. *Control of interlayer exchange coupling in Fe/Cr/Fe trilayers by ion beam irradiation*
   S.O. Demokritov, C. Bayer, S. Poppe, M. Rickart, J. Fassbender, B. Hillebrands, D.I. Kholin, N.M. Kreines, O.M. Liedke
   submitted to Phys. Rev. Lett.

2. *Probing the interface magnetism in the FeMn/NiFe exchange bias system using magnetic second harmonic generation*
   L.C. Sampaio, A. Mougin, J. Ferré, P. Georges, A. Brun, H. Bernas, S. Poppe, T. Mewes, J. Fassbender, B. Hillebrands
   submitted to Phys. Rev. Lett.

3. *Ion irradiation for magnetic sensor applications*
   J. Fassbender, S. Poppe, T. Mewes, J. Juraszek, B. Hillebrands, D. Engel, M. Jung, A. Ehresmann, H. Schmoranzer, K.U., Barholz, R. Mattheis
   submitted to Appl. Phys. A.

4. *Phase diagrams and energy barriers of exchanged biased bilayers with additional anisotropies in the ferromagnet*
   T. Mewes, H. Nembach, J. Fassbender, B. Hillebrands, J.V. Kim, R.L. Stamps
   submitted to Phys. Rev. B.

5. *Formation of envelope solitons from parametrically amplified and conjugated spin wave pulses*
   A.A. Serha, S.O. Demokritov, B. Hillebrands, A.N. Slavin
   submitted to J. Appl. Phys.

6. *Phase control of non-adiabatic parametric amplification of spin wave packets*
   A.A. Serha, S.O. Demokritov, B. Hillebrands, Seong-Gi Min, A.N. Slavin
   submitted to J. Appl. Phys.

7. *Spin wave wells with multiple states created in small magnetic elements*
   C. Bayer, S.O. Demokritov, B. Hillebrands, A.N. Slavin
   submitted to Appl. Phys. Lett.

Chapter 8: Conferences, Workshops, Schools and Seminars

(shown in chronological order with the speaker named)

8.1 Conferences

8.1.1 Invited talks

B. Hillebrands:
Ion beam techniques for the fabrication of nanoscale magnetic tunnel junctions and exchange bias systems
2001 Taiwan International Workshop on Applied Nanotechnology, Taipei, Taiwan, November 2001

J. Fassbender:
Einfluss ionenstrahl-induzierter Defekte auf den Exchange-Bias Effekt in magnetischen Dünnschichten
Hauptvortrag, DPG Frühjahrstagung, Regensburg, Germany, March 2002

T. Wittkowski:
Elastic properties of thin hard films analysed with Brillouin light scattering spectroscopy
DAGA 2002, Bochum, Germany, March 2002

S.O. Demokritov:
Confined magnetic excitations in structured magnetic media
Intermag 2002, Amsterdam, The Netherlands, May 2002

J. Fassbender:
Role of ion implantation in exchange bias systems
Intermag 2002, Amsterdam, The Netherlands, May 2002

M. Bauer:
Precession control and switching in thin magnetic films
8th Magneto-Optical Recording International Symposium (MORIS 2002), Brittany, France, May 2002

S.O. Demokritov:
Dynamics of patterned magnetic structures
Moscow International Symposium on Magnetism, Russia, June 2002

S.O. Demokritov:
Current induced magnetic excitations in confined systems
LATIS symposium on current induced magnetic switching, Lausanne, Switzerland, July 2002

8.1.2 Contributed talks and posters

2 contributions: American Vacuum Society Symposium, San Francisco, USA, October/November 2001

2 contributions:	46th Annual Conference on Magnetism and Magnetic Materials, Seattle, USA, November 2001
1 contribution:	Heraeus-Seminar, Bad Honnef, Germany, January 2002
9 contributions:	DPG-Frühjahrstagung Regensburg, Germany, March 2002
2 contributions:	ICMFS 2002, Kyoto, Japan, March 2002
2 contributions:	Gordon Research Conference on Magnetic Nanostructures, Il Ciocco, Italy, May 2002
2 contributions:	AOFA 12, Universität Kaiserslautern, Germany, September 2002

8.2 Workshops

8.2.1 Invited lectures

B. Hillebrands:
Dynamics in patterned magnetic structures
NEDO workshop on patterned magnetic systems: magnetic structures and dynamical behaviors, Cernay, France, October 2002

8.3 Invited Colloquia and Seminars

J. Fassbender:
Modifikation des Exchange-Bias-Effektes mittels Ionenbestrahlung bei Verwendung verschiedener antiferromagnetischer Materialien
Bosch Stuttgart, Germany, November 2001

J. Fassbender:
Ionenbestrahlung zur gezielten Modifikation von magnetischen Parametern
Universität Ulm, Germany, November 2001

S.O. Demokritov:
Spinwellendynamik in lateral strukturierten magnetischen Systemen
DFG-Schwerpunktseminar, Universität Karlsruhe, Germany, November 2001

J. Fassbender:
Switching dynamics and write endurance of magnetic tunnel junctions
NIST, Boulder, Colorado, USA, November 2001

J. Fassbender:
Zeitaufgelöste Untersuchungen zur Magnetisierungsdynamik und zum Schaltverhalten magnetischer Filme
Universität Mainz, Germany, December 2001

J. Fassbender:
Forschung für magneto-elektronische Anwendungen
LMU München, Germany, December 2001

B. Hillebrands:
An excellent testing ground for nonlinear wave propagation phenomena
Université Paris-Nord, Paris, France, January 2002

B. Hillebrands:
Magnetismus in nanoskaligen Systemen
SFB-Kolloquium, Universität Saarbrücken, Germany, January 2002

S.O. Demokritov:
Spinwellendynamik lateral strukturierter magnetischer Systeme
Universität Hamburg, Germany, May 2002

B. Hillebrands:
Spin-Dynamik in der Magnetoelektronik
Physikalisches Kolloquium, Universität Giessen, June 2002

S.O. Demokritov:
Surface morphology and induced magnetic anisotropy of vicinal Fe(001) films
Universität Saarbrücken, Germany, June 2002

J. Fassbender:
Magnetisierungsdynamik in Eisengranatfilmen und magnetischen Tunnelstrukturen
Universität Hamburg, Germany, June 2002

J. Fassbender:
Der Exchange-Bias-Effekt im NiFe/FeMn-System
GKSS Geesthacht, Germany, June 2002

S.O. Demokritov:
Spin waves in laterally confined magnetic systems
ETH Zürich, Switzerland, July 2002

8.4 Contributions to other Meetings

B. Hillebrands:
Non-monotonic magnetic anisotropy of vicinal Fe(001) films with different miscut orientations
Final meeting of the network “Nanomag”, European Science Foundation, Anglet, France, October 2001

T. Wittkowski:
Effective elastic constants of boron nitride films
8th c-BN Expert Meeting, Stuttgart, Germany, October 2001

J. Fassbender:
Magnetisierungsdynamik von magnetischen Tunnelstrukturen
BMBF-Kick-Off-Meeting, Kahl, Germany, February 2002

T. Wittkowski:
Oberflächenphononen in h-B/c-BN-Schichten mit kontrollierter h-BN-Lagendicke
9th c-BN Expert Meeting, Bonn, Germany, October 2002

Appendix: Impressions from our Ph.D. Ceremonies

Dr. Radek Lopusnik

Dr. Thomas Wittkowski

Dr. Marc Rickart